

**A Thesis Submitted for the Degree of PhD at the University of Warwick**

**Permanent WRAP URL:**

<http://wrap.warwick.ac.uk/102257>

**Copyright and reuse:**

This thesis is made available online and is protected by original copyright.

Please scroll down to view the document itself.

Please refer to the repository record for this item for information to help you to cite it.

Our policy information is available from the repository home page.

For more information, please contact the WRAP Team at: [wrap@warwick.ac.uk](mailto:wrap@warwick.ac.uk)

THE BRITISH LIBRARY DOCUMENT SUPPLY CENTRE

TITLE

Magnetic Properties of Gd-Y and Gd-Sc Alloys

AUTHOR

Richard John Melville

INSTITUTION  
and DATE

UNIVERSITY OF WARWICK

1989

Attention is drawn to the fact that the copyright of this thesis rests with its author.

This copy of the thesis has been supplied on condition that anyone who consults it is understood to recognise that its copyright rests with its author and that no information derived from it may be published without the author's prior written consent.



THE BRITISH LIBRARY  
DOCUMENT SUPPLY CENTRE

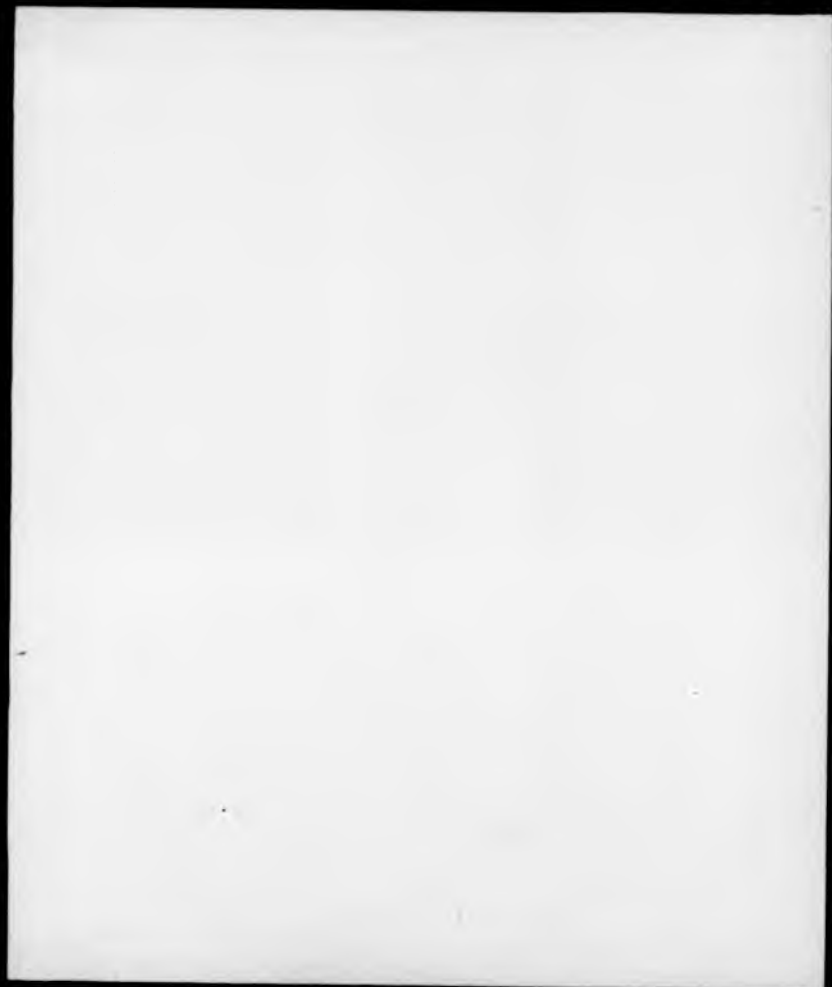
Boston Spa, Wetherby  
West Yorkshire  
United Kingdom

20

REDUCTION X

CAMEA

3



Magnetic Properties of Gd-Y and Gd-Sc Alloys

being a thesis submitted for the degree of Doctor  
of Philosophy at the University of Warwick

by

Richard John Melville, B.Sc. (Hull)

Department of Physics,  
University of Warwick, June 1969.

## Abstract

The magnetic structures and behaviour of Gd-Y and Gd-Sc random alloys have been investigated by single crystal neutron diffraction, ultrasonic measurements of the crystal elastic constants and resistivity measurements. The composition of the alloys studied was chosen in order to observe the competition between the ferromagnetism favoured by Gd-rich alloys and helimagnetism favoured by dilution with Y or Sc.

Neutron diffraction studies of  $\text{Gd}_{60}\text{Y}_{40}$  and  $\text{Gd}_{66}\text{Y}_{34}$  have been concerned principally with the helimagnetic/ferromagnetic transition. Of particular interest has been the behaviour of the modulation wavevector when the ferromagnetic phase is approached as the temperature is lowered. A novel approach to peak-fitting of the diffraction profiles for  $\text{Gd}_{66}\text{Y}_{34}$  has enabled helical inter-layer turn angles of less than  $1^\circ$  to be measured, and no evidence has been observed for any discontinuity of the turn-angle as the transition occurs. This is unique behaviour among the rare-earths.

$\text{Gd}_{60}\text{Y}_{40}$  exhibits differing behaviour as the helimagnetic/ferromagnetic transition is approached. This transition occurs at low temperature, but is unusual in that an apparently 'frozen-in' state of coexisting ferromagnetism and helimagnetism sets in below  $\sim 50$  K. The nature of the phase boundary is discussed concerning this behaviour together with the possible role of random field effects.

Gd-Sc alloys of composition between 64% and 76.7% Gd were initially characterized over their full magnetically ordered temperature range by elastic constant measurements. Neutron diffraction was then used to make accurate structure determinations for the magnetic phases exhibited in this alloy system. Resistivity measurements have provided useful additional information regarding the phases, particularly with regard to the ferro-I phase observed in the alloy richest in Gd.

The magnetic phase diagram for the Gd-Sc system has been observed to be quite dissimilar to that of Gd-Y in the region of 70% Gd. First, there is a conical helix phase separating the helical and ferromagnetic phases, which is absent in Gd-Y. Secondly, the ferro-I phase of Gd-Y is considerably less extensive in Gd-Sc than in Gd-Y. This is unusual in view of earlier belief that this phase should be enhanced by the substitution of Sc for Y. Also, preliminary elastic constant and resistivity measurements for  $\text{Gd}_{64}\text{Sc}_{36}$  have revealed rich and interesting behaviour in an applied magnetic field.

### Declaration

The work contained in this thesis is my own except where specifically stated as otherwise, and was based in the Department of Applied Physics at the University of Hull during the period October 1985 to November 1987 and based in the Department of Physics at the University of Warwick from November 1987 to June 1989. No part of this work has previously been submitted to this or any other academic institution for admission to a higher degree. Some of the work has already appeared in the form of publications which are listed at the end of the reference section.

B. H. H. H.

## Contents

<b>Chapter 1: Introduction .....</b>	<b>1</b>
Introduction .....	1
1.1 Gd, and Alloying Properties of Y and Sc .....	3
1.2 Magnetic Interactions in the Rare-Earths .....	5
1.3 Review on Past Work in Gd Alloys .....	11
1.4 Samples used in this Study .....	15
 <b>Chapter 2: Neutron Diffraction in the Study of Gd-Y and Gd-Sc Alloys .....</b>	 <b>17</b>
Introduction .....	17
2.1 Elastic Nuclear and Magnetic Neutron Diffraction .....	18
2.1.1 Scattering from a Single Ion .....	18
2.1.2 Scattering from a 3D Bravais Lattice .....	23
2.1.3 Ferromagnetic Scattering from a 3D non-Bravais Crystal Lattice .....	26
2.1.4 Helimagnetic Scattering from a 3D non-Bravais Crystal Lattice .....	27
2.2 Diffraction from Gd-Y and Gd-Sc Alloys .....	29
2.2.1 The Reciprocal Lattice .....	29
2.2.2 The Geometric Structure Factor .....	30
2.2.3 Ferromagnetic Structures in Gd-Y and Gd-Sc Alloys .....	30
2.2.4 Modulated Structures in Gd-Y and Gd-Sc Alloys .....	32
2.2.5 Nuclear Scattering Length .....	34
2.2.6 Gd Magnetic Form Factor .....	35

## Contents

<b>Chapter 3: Neutron Diffraction Experimental Techniques .....</b>	<b>38</b>
Introduction .....	38
3.1 Neutron Diffractometer D9 .....	38
3.2 Resolution Effects .....	40
3.3 Experimental Procedure .....	41
3.4 Nuclear Structure Refinement .....	42
3.5 Evaluation of the Average Spontaneous Magnetization .....	43
3.6 Correction Factors .....	44
3.7 Errors in the Evaluation of $(S_q)^2$ .....	47
<b>Chapter 4: Experimental Results: Gd-Y .....</b>	<b>49</b>
4.1 $Gd_{65}Y_{34}$ .....	50
4.1.1 General Properties .....	50
4.1.2 The Helix/Ferromagnetic Transition in $Gd_{65}Y_{34}$ .....	52
4.2 $Gd_{60}Y_{40}$ .....	55
4.2.1 General Properties .....	55
4.2.2 The Low Temperature Transition in $Gd_{60}Y_{40}$ .....	58
<b>Chapter 5: Experimental Results: Gd-Sc .....</b>	<b>60</b>
Introduction .....	60
5.1 $Gd_{64}Sc_{36}$ .....	60
5.2 $Gd_{66}Sc_{34}$ .....	62
5.3 $Gd_{70.8}Sc_{29.2}$ .....	64
5.4 $Gd_{72}Sc_{28}$ .....	65
5.4 $Gd_{77.8}Sc_{22.2}$ .....	68
5.4 $Gd_{78.7}Sc_{21.3}$ .....	70



**Chapter 6: Ultrasonic Studies of Crystal Elastic Constants of Gd-Sc Alloys ..... 73**

Introduction .....	73
6.1 Magnetoelastic Effects in Gd-Y and Gd-Sc Alloys .....	74
6.2 Elastic Constants in the Hexagonal Crystal System .....	77
6.3 Experimental Technique for Measurement of Ultrasonic Wave Velocities .....	78
6.4 Temperature Dependence of Elastic Constants of Gd-Sc Alloys .....	81
6.4.1 Gd <sub>72</sub> Sc <sub>28</sub> .....	82
6.4.2 Gd <sub>64</sub> Sc <sub>36</sub> , Gd <sub>60</sub> Sc <sub>40</sub> , Gd <sub>60</sub> Sc <sub>40</sub> , and Gd <sub>70.5</sub> Sc <sub>29.5</sub> .....	88
6.4.3 Gd <sub>75</sub> Sc <sub>25</sub> .....	89
6.4.4 Gd <sub>78.7</sub> Sc <sub>21.3</sub> .....	90
6.5 Summary .....	92

**Chapter 7: Resistivity, Magnetization and Applied Field Studies ..... 93**

Introduction .....	93
7.1 Resistivity in Gd <sub>64</sub> Sc <sub>36</sub> , Gd <sub>72</sub> Sc <sub>28</sub> and Gd <sub>75</sub> Sc <sub>25</sub> .....	94
7.1.1 Gd <sub>64</sub> Sc <sub>36</sub> .....	96
7.1.2 Gd <sub>72</sub> Sc <sub>28</sub> .....	96
7.1.3 Gd <sub>75</sub> Sc <sub>25</sub> .....	97
7.2 Magnetization Measurements on Gd <sub>64</sub> Sc <sub>36</sub> and Gd <sub>64</sub> Sc <sub>28</sub> .....	98
7.2.2 Gd <sub>72</sub> Sc <sub>28</sub> .....	98
7.2.1 Gd <sub>78.7</sub> Sc <sub>21.3</sub> .....	100
7.3 Ultrasonic Study of H-T Phase Diagram of Gd <sub>64</sub> Sc <sub>36</sub> .....	101
7.3.1 Gd <sub>64</sub> Sc <sub>36</sub> : Isothermal Measurements of C <sub>33</sub> in an Applied Magnetic Field .....	101
7.3.2 Gd <sub>64</sub> Sc <sub>36</sub> : Isofield Measurement of C <sub>33</sub> .....	103
7.3.3 Magneto-resistance Measurements .....	104

## Contents

7.4 Summary .....	105
<b>Chapter 8: Discussion and Conclusions .....</b>	<b>107</b>
8.1 Gd-Y .....	107
8.2 Gd-Sc .....	111
8.2.1 Magnetic Properties of the System .....	111
8.2.2 Ferro-I in Gd-Sc .....	113
8.2.3 $Gd_{78.7}Sc_{21.3}$ .....	115
8.2.4 Magnetic Critical Points .....	117
8.2.5 Gd-Sc Magnetic Phase Diagram- General Overview .....	117
8.3 Future Work .....	119
<b>Appendix A .....</b>	<b>122</b>
<b>Appendix B .....</b>	<b>125</b>
<b>References .....</b>	<b>128</b>

## Acknowledgements

The research carried out for this thesis was originally based at Hull University, and in the past 18 months at Warwick University. The neutron scattering experiments were carried out at the Institut Laue-Langevin, Grenoble in France, and some of the work was done in collaboration with the University of Porto, Portugal. It is therefore a pleasure for me to have the opportunity to acknowledge the help and support of many colleagues at these institutions.

Sincere thanks are due to my supervisor Prof. S.B. Palmer for introducing me to an interesting field of research, and for his friendship and high spirited character which has always been a great encouragement.

At the I.L.L., particular thanks are extended to Dr. G.J. McIntyre for taking a personal interest in my work, and for his patience and dedication with the neutron experiments. I also thank Dr. M. Vrtis for being a most helpful co-worker and lively companion.

At the University of Porto, I would like to thank Prof. J.B. Sousa for his unrivalled enthusiasm and warm friendship. Thanks also to Dr. J.M. Moreira for his hospitality during my stay in Portugal.

I am very grateful to Dr. B. Barbara at the Laboratoire Louis Néel, Grenoble, for the magnetization measurements, and also to Dr. B.J. Beaudry of the Ames Laboratory, Iowa, and Dr. D. Fort of the Centre for Materials Science, University of Birmingham, for provision of the samples.

Also, I am indebted to staff both at Hull and at Warwick for their help throughout the past three years, and also to the technical staff, without whose support research would be very difficult.

I should like to give special thanks to Simon Bates, a colleague and close friend on the rare occasions we have had to meet, whose presence has injected much vitality into my stays in Grenoble.

Finally, I owe much gratitude to Diana, and to Mum, Dad and Dominic for 'being there', and to them I dedicate this thesis.

*Still there are moments when one feels free from one's own identification with human limitations and inadequacies. At such moments, one imagines that one stands on some spot of a small planet, gazing in amazement at the cold yet profoundly moving beauty of the eternal, the unfathomable: life and death flow into one, and there is neither evolution nor destiny; only being.*

Albert Einstein

## 1

## Introduction

**Introduction**

Gd readily forms alloys in solid solution with other rare-earth metals and also the nonmagnetic rare-earth-like metals Y and Sc. This work, concerned principally with Gd-Sc alloys, has been inspired by the recent flurry of interest in Gd-Y alloys, which have proved to be particularly suited to investigating the competition between ferromagnetic order developed in Gd-rich alloys, and helical antiferromagnetic order developed in Y-rich alloys. Such competition, together with the very low anisotropy, leads to a very unusual and complex magnetic phase diagram which has been extensively explored using neutron diffraction techniques (see for example Child and Cable, 1969, Legvold et al., 1980, Bates et al., 1985, 1987). Of particular interest has been the proposed Lifshitz point near 30 at.% Y, where paramagnetic, ferromagnetic and helical antiferromagnetic phases coexist. A Lifshitz point was not found, but instead two multicritical points in the same region of composition, one of which bears resemblance to a Lifshitz point in two dimensions (Bates et al., 1985). Another most interesting, and possibly unique feature of Gd-Y is the apparently smooth approach to zero of the modulation wavevector as the ferromagnetic phase boundary is approached from the helical phase. A turn angle of  $1.4^\circ$  has been reported in a 32 at.% Y alloy (Bates et al. 1985) and this is by far the smallest turn angle observed for a rare-earth material. This behaviour is almost certainly attributable to the low basal plane

anisotropy of the system, yet the possibility of a continuous phase transition between these two ordered phases remains somewhat intriguing.

The feature of perhaps greatest interest in the Gd-Y alloys is the 'double ferromagnetism' proposed by L gvold (1980) on the basis of the two-tier magnetization curves, and confirmed by neutron diffraction. Alloys exhibiting this property (>30 at.% Y) order initially into a phase (ferro-I) where the spin structure is such that there is a component of the magnetic moment pointing along the hexagonal c-axis and another distributed randomly in the basal plane. At lower temperature, the basal plane component of magnetization orders, and the structure becomes ferromagnetic; there are therefore two apparently decoupled ordering regimes. The ferro-I phase is believed to have its origin in a short-range exchange interaction (Bates, 1985).

Although both Y and Sc crystallize in the hexagonal close-packed structure and both form a continuous solid solution with Gd for all compositions, they differ as diluents. Y has an atomic volume very similar to that of Gd (Y:19.95 cm<sup>3</sup>/mol, Gd:19.91 cm<sup>3</sup>/mol), whereas Sc has a considerably smaller atomic volume (Sc:15.04 cm<sup>3</sup>/mol). This is particularly important when considering the relative magnetic properties of the alloys, since the band structure and the density of states at the Fermi level are likely to be more strongly perturbed in the Gd-Sc alloys than in the Gd-Y alloys (L gvold, 1979). It is by these arguments that the departures from the mean-field behaviour in both alloy systems may be understood (see section 1.3).

One interesting consequence of a large band structure distortion in the Gd-Sc alloys is a weakening of the RKKY exchange interaction due to a reduction in the conduction electron mean free path. It might therefore be expected that the reduced exchange interaction would favour the formation of a magnetic phase similar to the ferro-I phase, hitherto only observed in Gd-Y alloys. Furthermore, the competing interactions between ferromagnetic and helical order introduced by the dilution of Gd with Sc have rendered Gd-Sc

alloys an ideal candidate for a Lifshitz point (Hornreich, 1980) although the phase diagram in the region of ferromagnetic/helical coexistence has not been well determined.

This study has thus been motivated by the richness of the Gd-Y alloy system and the likely interesting consequences of substituting Sc for Y. It was hoped that by comparing the similarities and differences of the magnetic behaviour of the two alloy series, one would be able to attribute particular properties to either Gd or its diluent and therefore identify the fundamental consequences of replacing Y by Sc.

The technique of neutron diffraction, being the most definitive means of determining the magnetic structures, was used extensively. The short wavelength neutrons available at the Institut Laue-Langevin (ILL), Grenoble, enabled the inherent absorption problems associated with Gd to be partially overcome (as in previous Gd-Y studies), and the improved resolution of the newly rebuilt D9 instrument was expected to benefit studies of long period incommensurate antiferromagnetic phases. Ultrasonic velocity measurements at Hull and at Warwick together with collaborative work involving transport property measurements at Porto, Portugal, were used to characterize the samples and provide a broader picture of the magnetic behaviour to support the neutron measurements.

### 1.1 Gd, and Alloying Properties of Y and Sc

Gd is a group IIIA element, and is the mid-member of the 14 elements which start at La (Z=57) and finish with Lu (Z=71) and which have become known (somewhat misleadingly) as the 'rare-earths'. The rare-earths are classed in the third group of the periodic table since the 4f electron shell is being filled, while the number of outer valence electrons remains unchanged. Gd has a half-filled 4f shell from which it derives its magnetic properties, and



the two outermost shells, the 6s and 5d shells are occupied by two electrons and one electron respectively. This is in keeping with the normal electronic configuration of the rare-earths:  $Xs4f^n5d^16s^2$  ( $n=1$  to 14). The relative positions in energy of these atomic states (Herman and Skillman, 1963) are shown in figure 1.1.

The 5d and 6s atomic states are close in energy, but are well separated from the 4f level. In their usual metallic state, the rare-earths lose the 5d and 6s electrons to the conduction band with a resulting high chemical similarity among them. Indeed it was not until the late 1950's that Spedding and his colleagues at Iowa State University and the Ames Laboratory succeeded in producing the first reasonably pure samples.

If we examine the radial extent of the electrons in Gd (figure 1.2), it is clear that the 4f shell is highly localized; there is very little overlap between 4f wavefunctions on neighbouring sites. Also, the 4f wavefunction maximum lies well within the closed 5s and 5p shells and thus form a very narrow energy band. This is in contrast to the 5d and 6s atomic wavefunctions which do overlap one another to a considerable extent and which form a relatively wide s-d conduction band. As a consequence of the extreme localization of the 4f electrons, the ground state of Gd is well described by Hund's Rules: for the half-filled shell,  $S=7/2$  and  $L=0$  with  $J=L+S$  being a good quantum number. The localized saturation moment of Gd is then given by  $\mu_{Gd} = Jg\mu_B$ , where the Landé factor  $g$  is 2 for spin-only ions, and hence  $\mu_{Gd} = 7\mu_B$ . In fact a host of magnetisation measurements on Gd have indicated that the saturation moment per Gd atom is about  $7.63\mu_B$  (Rosland et al., 1975), where the additional moment is normally attributed to the polarization of the conduction electrons.

Gd, being an S-state ion, is in many ways unique among the rare-earths: the spherical charge cloud means there is relatively little magnetic anisotropy. Also, Gd is the only rare-earth to order initially into a ferromagnet

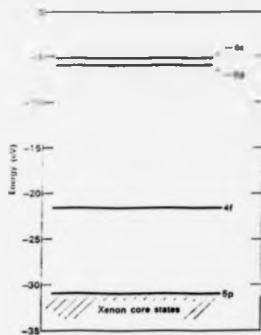


Figure 1.1 The relative positions in energy of the outer atomic electrons in atomic Gd.

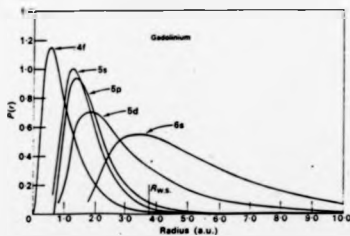


Figure 1.2 The relative outer radial extent of the atomic electrons in atomic Gd. The Wigner-Seitz radius appropriate to Gd in its metallic state is indicated.

and has the highest ordering temperature (294 K) of all the rare-earths. It remains a ferromagnet at all temperatures below  $T_c$  (c-axis ferromagnet at high temperature) but exhibits a spin-reorientation transition at 235 K, where the magnetic moments rotate away from the c-axis toward the basal plane (Cable and Koehler, 1982).

Y and Sc may be regarded as good diluents for Gd and indeed other heavy rare-earth metals because they crystallize in the same hcp structure and have a similar outer electron configuration (for Sc,  $3d^1 4s^2$ ; for Y,  $4d^1 5s^2$ ). In spite of the 25% atomic size disparity for Sc, both Y and Sc form continuous solid solutions with Gd, and for the same reasons are usually accommodated under the name of 'rare-earths'. The smaller atomic volume of Sc is the most obvious difference between the two as nonmagnetic diluents; in the RKKY theory, no dependence of exchange energy on volume is predicted although there is a slight variation of exchange energy with the c/a ratio. Interestingly enough, Sc is more compatible in this respect than Y, which has a c/a ratio of 1.573. Sc and Gd have ratios of 1.592 and 1.591 respectively. A more detailed discussion of the diluent properties of Y and Sc will be given in section 1.3.

## 1.2 Magnetic Interactions in the Rare-Earths.

The variations in magnetic structure that occur throughout the heavy rare-earths can be considered as the natural consequence of a single Hamiltonian for the 4f localized moment system. Following Cooper (1972), two types of energy must be included in the Hamiltonian:

$$H = H_{\text{iso ex}} + H_{\text{an}} \quad (1.1)$$

The first contribution is the effective Heisenberg spin Hamiltonian for the isotropic exchange interaction between localized spin sites  $i$  and  $j$ ,

$$H_{\text{iso ex}} = \sum_{i \neq j} J_{ij} \mathbf{S}_i \cdot \mathbf{S}_j, \quad (1.2)$$

where  $J_{ij}$  is the exchange constant and  $\mathbf{S}$  is the total ionic spin. We return to this interaction later in the section.

The second contribution arises due to anisotropic factors, predominantly caused by the orbital contribution to the ionic moment:

$$H_{\text{an}} = H_{\text{an ex}} + H_{\text{cf}} + H_{\text{ma}}. \quad (1.3)$$

$H_{\text{an ex}}$  is attributed to the non-sphericity of the 4f wavefunctions and is, for most purposes, a negligible effect. The second term is the anisotropy energy of the unstrained lattice resulting from interaction with the crystalline electric field caused by each rare-earth ion 'seeing' the other charged ions in the lattice, and it follows that this crystal field will exhibit the symmetry of the ionic lattice. Gd of course, being an S-state ion will suffer from relatively little crystal field anisotropy, two to three orders of magnitude smaller than other heavy rare-earths.

The final contribution to  $H_{\text{an}}$  comes from magnetostriction effects. There are both single-ion and two-ion contributions to these effects arising from the modulation by strain of the crystal field and anisotropic exchange interactions respectively:

$$H_{\text{ma}} = H_{\text{a}} + H_{\text{m}}. \quad (1.4)$$

Here  $H_{\text{a}}$  is the elastic energy associated with a homogeneous strain, while  $H_{\text{m}}$  is the magnetoelastic interaction coupling the spin system to the strains. We shall discuss magnetostrictive effects in further detail in chapter 6.

We now show how the Hamiltonian of (1.1) gives rise to the various types of magnetic structure by treating the localized moments in the molecular field approximation, following the approach used by Elliot (1961) to discuss the phenomenological theory of magnetic ordering in the rare-earths. The periodicity of the equilibrium spin arrangement is determined by the exchange

interactions. We assume a model for the spin arrangements described by two parameters; the wave vector  $q$  of the modulation parallel to the  $c$ -axis and the angle between the moments and the  $c$ -axis,  $\theta$  (figure 1.3). The moments may be described with reference to an orthogonal set of axes with the  $z$  axis parallel to the hexagonal  $c$ -axis:

$$S_{iz} = S \sin \theta \cos(q \cdot R_i), \quad S_{iy} = S \sin \theta \sin(q \cdot R_i), \quad S_{ix} = S \cos \theta, \quad (1.5)$$

where  $R_i$  is the position vector of the  $i$ th moment and  $S_{ix}$ ,  $S_{iy}$  and  $S_{iz}$  are the components of the moment with respect to the chosen axes. By considering the allowed values for  $q$  and  $\theta$ , equation (1.5) describes a number of spin arrangements:

(1)  $q$  and  $\theta$  general values; the moments lie on the surface of a cone of angle  $\theta$ . This is the case with Er and Ho at low temperatures.

(2)  $q = 0$  and  $\theta \neq 0$ ; this is a description of a canted ferromagnetic structure with canting angle  $\theta$  to the  $c$ -axis, as in Gd below its spin-reorientation transition.

(3)  $q \neq 0$  and  $\theta = 0$ ; the moment vectors are parallel to the  $c$ -axis and their magnitude is modulated along the  $c$ -axis e.g. Er above 53 K and Tm.

(4)  $q = 0$  and  $\theta = 0$ ; this condition describes a  $c$ -axis ferromagnet, as in Gd above its spin-reorientation transition.

(5)  $q \neq 0$  and  $\theta = \pi/2$ ; the spin-arrangement here is a planar spiral as in Dy, Tb and Ho at high temperature.

(6)  $q = 0$  and  $\theta = \pi/2$ ; this description corresponds to a ferromagnet with moments in the basal plane as in Dy and Tb at low temperature.

The exchange energy is solely responsible, in the absence of magnetic anisotropy, for the value of  $q$ . It is useful to consider the Fourier transform of the exchange interaction:

$$J(Q) = \sum_j J_{ij} \exp[iQ \cdot R_{ij}]. \quad (1.6)$$

where  $Q$  is a general wavevector. The exchange energy then becomes

$$E_{\text{ex}} = -J(Q). \quad (1.7)$$

We now see that the exchange interaction determines the periodicity of the magnetic structure, for the spiral pitch is determined by that wavevector  $q$  which maximizes  $J(Q)$ , thereby lowering the energy. Furthermore, if the maximum of  $J(Q)$  occurs at  $Q = 0$ , then exchange favours a ferromagnetic arrangement, and if the maximum is at the edge of the Brillouin zone, then exchange favours a conventional antiferromagnet. If, however, the maximum appears at some wavevector between the origin and the zone boundary, then a spiral arrangement will be supported, as observed in many heavy rare-earths.

It has been known for some time (e.g. Yoshimori, 1959) that the existence of spiral spin structures is due to the presence of competing exchange interactions. For example, a positive interaction between nearest neighbours and a negative interaction between next-nearest neighbours may give rise to such structures. The mechanism responsible for the oscillatory interactions necessary for spirals in the rare-earths is the RKKY interaction, which is now discussed.

Although the open 4f shell contributes almost all the entire observed bulk magnetization, strong magnetic ordering clearly cannot be explained by a direct exchange interaction between 4f shells since the overlap of their wavefunctions is negligible. Instead, it is now accepted that the magnetic ordering is promoted through an indirect interaction between 4f shells, mediated by a polarization of the conduction electrons. Such a polarization has an oscillatory component due to the Fermi distribution which restricts the wavevector of the conduction electrons carrying the polarization. This interaction is known as the RKKY interaction after Ruderman and Kittel (1954), Kasuya (1957) and Yosida (1957). The indirect exchange produces an

effective 4f-4f coupling which is responsible for the various observed magnetic properties. It may be written (Freeman, 1972):

$$J(\mathbf{Q}) = \frac{2}{N} |j_{sf}(\mathbf{Q})|^2 \chi(\mathbf{Q}) \quad (1.8)$$

where  $j_{sf}(\mathbf{Q})$  is the s-f exchange element governing the strength of the interaction between the conduction and f electrons, and N is the number of magnetic lattice sites per unit volume.  $\chi(\mathbf{Q})$  is the wavevector dependent susceptibility and is a measure of the response of the electron gas to the exchange field of the localized spin. In the free electron band approximation, the RKKY interaction may be written in a more familiar form

$$J(\mathbf{R}) = (9/2) \pi / 2E_F \Phi(2k_F R), \quad (1.9)$$

with

$$\Phi(x) = \frac{x \cos x - \sin x}{x^4}. \quad (1.10)$$

$E_F$  is the Fermi energy and  $k_F$  is the Fermi wavevector. The interaction is thus long-range, decreasing as  $R^{-3}$  for large R, and oscillates with the period  $(2k_F)^{-1}$ .

The free electron approximation of the RKKY interaction is not correct since it gives a maximum of  $J(\mathbf{Q})$  at  $\mathbf{Q} = 0$ . However, Yosida and Watabe (1962) used a nearly free electron approximation to the conduction electron band and arrived at a spiral turn angle of  $48^\circ$ . This was very close to the value of  $51^\circ$  observed in Tm, Er and Ho, but in fact turned out to be mere coincidence, since band calculations have shown that the conduction bands and Fermi surface are remote from an almost free electron model.

A more instructive approach may be taken by considering details in the Fermi surface of the rare-earths in conjunction with equation (1.2). The most stable spin structure is determined by a maximum in  $J(\mathbf{Q})$ , and has been shown, under certain approximations, to be determined by the maximum in

the susceptibility. Lomer (1962) first realized that the feature of the Fermi surface required to produce a maximum in the susceptibility was 'nesting'; large, nearly flat parallel areas separated by  $q$ . The Fermi surface of holes for Gd is shown in figure 1.4. The surface consists of a single volume with a 'trunk' contributed by bands of largely s-p character and 'arms' in the vicinity of the ALH plane which arise mainly from bands of d character. Keeton and Loucks (1968) carried out relativistic augmented plane wave band calculations for the rare-earth metals and showed that 'webbing' between two arms near L of these Fermi surfaces exists for heavy rare-earth metals such as Lu, Er and Dy, as well as Y, but is nearly absent in Gd which is consistent with the helical wavevector  $q$ . The webbing was responsible for the separation in the hexagonal  $c$  direction of those flat Fermi surfaces required for nesting. In fact remarkable agreement was shown between the observed periodicities and those determined by the nesting characteristics calculated by a band theoretical approach.

We now return to the anisotropic contribution to the magnetic Hamiltonian,  $H_{\text{An}}$ . We know the anisotropic effects are very small for Gd due to the absence of an orbital magnetic moment. However, it has recently been shown (Kaino and Kasuya, 1981), that there is a further addition to the anisotropy. Using a simple band model, the non-linear effect of the s-f interaction was investigated, and it was found that the non-linear effect stabilized the cone structure thus contributing to the anisotropy energy. The non-linear effect was also found to be responsible for the ferromagnetic transition. Although the model was too simple to make detailed numerical comparison with experimental results in rare-earth metals, it was broadly seen to account for the magnetic phase diagrams of Gd-Y and Gd-La. We leave further discussion for the time being and note that the anisotropic effects may be treated together in a phenomenological framework:



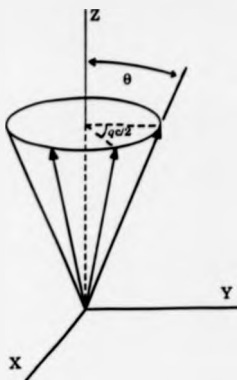


Figure 1.3 Cone spin arrangement. Arrows indicate moments of successive planes perpendicular to the c-axis.

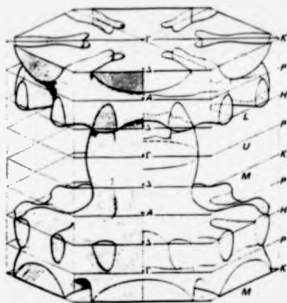


Figure 1.4 Complete non-relativistic Fermi surface of non-magnetic Gd (after Dimmock and Freeman, 1964).

$$E_A = K_1 \sin^2 \theta + K_2 \sin^4 \theta + K_3 \sin^6 \theta + K_4 \sin^8 \theta \cos 6\phi, \quad (1.11)$$

where  $K_i$  are the anisotropy constants,  $\theta$  is the angle between the moment and the c-axis, and  $\phi$  is the angle between the projection of the moment on the basal plane and the a-axis. The first three terms represent anisotropy regarding the direction of the moment with respect to the c-axis, the fourth reflects the anisotropy within the basal plane.

We have thus shown how the equilibrium magnetic structures of the heavy rare-earths (and their alloys with themselves and the nonmagnetic rare-earth-like elements Y, La and Sc) may be understood as the combination of the RKKY exchange interaction and the details of the Fermi surface, which determine the  $q$  of the magnetic structure, and the anisotropic effects which determine the easy planes or axes of the structure. We concentrate now on the alloying effects of the nonmagnetic elements on Gd.

### 1.3 Review on Past Work in Gd Alloys.

Since the late 1950's, much effort has been directed to studying the magnetic properties of alloy systems of the heavy rare-earth metals with a nonmagnetic constituent as well as with each other. Originally, the physics of rare-earth metals was thought to be simple: the magnetic interaction is the long-ranged RKKY interaction, which was expected to scale with the de Gennes factor,  $G = (g-1)^2 J(J+1)$ , from one element to the next. The anisotropies of the rare-earths should scale with the Stevens factors that determine the  $4f$  electron distribution. Both  $G$  and the Stevens factors are independent of solid-state effects, being determined purely from atomic considerations. However, through studies of alloys, it soon became apparent that significant and systematic deviations occurred. In particular it was found that the Néel temperatures (proportional to the exchange interaction) varied as  $G^{2/3}$  rather than  $G$  (e.g. Koehler, 1965, Bozorth and Gambino, 1966). Only relatively

recently has the solution to this problem been known to reside in one or a combination of three explanations. These are 1) a variation of the exchange interaction with concentration due to a concentration-dependent band structure (Lindgård, 1977), 2) a linear scaling with the de Gennes factor but with  $J$  replaced by  $S$  (Løvold, 1978), and 3) the inclusion of a mean free path dependence in the RKKY interaction (Young, 1983). We shall return to these arguments after briefly reviewing past work on Gd-X alloys, where X is Y, Sc, La or Lu. Particular features of the Gd-Y alloys, the essence of which has been given in the introduction, do not receive attention in this section, since they are well documented elsewhere (Blackie, 1982; Bates, 1985).

The first measurements on these alloy types were made by Thoburn et al. (1958) on Gd-La and Gd-Y alloys. These, like most early measurements on the rare-earths before the potential of neutron diffraction was realized, were magnetization measurements on a range of polycrystalline samples. It was found that alloys of high (>66%) Gd content underwent paramagnetic to ferromagnetic transitions on decreasing the temperature, but that alloys with a lower Gd content underwent antiferromagnetic transitions. Also, it was noted that experimentally determined values of the saturation ionic moment per Gd site,  $\mu_{Gd}$ , were significantly higher than the theoretical values for Gd obtained on the assumption of contributions by 4f spin alone ( $\mu_{Gd} = gJ = 7\mu_B$ ). Nigh et al. (1964) made similar measurements on Gd-Sc alloys and noticed that the saturation magnetic moment per Gd atom increased with decreasing Gd concentration in the case of the ferromagnets. Antiferromagnetic and ferromagnetic states at different temperatures were exhibited in a 69% Gd alloy. Perhaps of greater significance was that there appeared to be a lowering of the ordering temperatures on substituting Sc for Y, and it was suggested that a decreased magnetic interaction might result from the smaller lattice parameter of Sc. This was also found to be true of Gd-Lu alloys (Smidt and Daane, 1963).

In a molecular field analysis of the Tb-Y alloy system (Wollan, 1967), Wollan discussed his results relative to the initial magnetic ordering properties in terms of their implication for the heavy rare-earth metals and their alloys with Y, Sc and La. He concluded that the magnetic properties were closely tied to the effect of the crystal parameters on the magnetic coupling, which would not be anticipated on the basis of a simple free-electron RKKY type interaction. In particular, the axial ratio ( $c/a$ ) and atomic volume of the diluent were believed to be the key to understanding the deviations of the ordering temperatures from those predicted by mean field theory and the variation of the excess saturation ionic moment observed for Gd. Wollan (1967) went further by comparing the Gd-Y system and the Gd-Sc system. It was concluded that with regard to the initial ordering properties of the alloys, the two systems had the same magnetic coupling properties when account was taken of the effect of the change in volume in the Gd-Sc alloys. Furthermore, a quantitative comparison between these volume changes, and the volume changes brought about in the pure metals by the application of high pressures were found to be in agreement.

Child and Koehler (1968) investigated alloys of Tb, Ho and Er with Sc by powder neutron diffraction, where it was remarked that the absence of magnetic order in what are still relatively concentrated alloys shows that the magnetic interaction is greatly modified when Sc is put into the system. The overall effect was apparently to abruptly weaken the interaction at a critical concentration of 70-80% Sc. Similar observations were made in the magnetization studies of Nigh et al. (1964).

A powder neutron diffraction study of Gd-Y and Gd-Sc alloys by Child and Cable (1969) extended the neutron diffraction studies. For the first time a low-absorbing isotope of Gd,  $^{160}\text{Gd}$ , was used. Much information was given on the magnetic phases including turn angles and canting angles (the angle

between the moment and the c-axis), and the ordered moment was observed to vary considerably between 6.6 and 8.1 $\mu_B$ .

Consequently, at that time, not only was there the problem of the non-linear scaling of the ordering temperatures with the de Gennes factor, but there were exceptions to the 'universal' behaviour, namely the alloys with Y, Sc and to a smaller extent Lu. Further complications were added to the picture when the dependence of the excess moment per Gd atom under dilution with Y, Sc, La and Lu was found to be inversely proportional to the c/a ratio (White et al., 1975).

It was not until 1977 that some light was shed on the matter. Lindgård (1977) combined a mean-field random alloy theory with a simple calculation of the exchange interaction  $J(Q)$  and showed that this quantitatively accounted for the phase diagram for alloys of rare-earth metals with Y, Lu, Sc and other rare-earth metals. The small atomic volume and corresponding low density of states at the Fermi level of Sc was found to be an important correction for Gd-Sc alloys. However, this theory could not account for the excess moment per Gd ion on dilution.

Legvold (1979) proposed a different solution. The rare-earths and their alloys were found to scale with  $S(S+1)$  extremely well. The notable exceptions, the Y and Sc alloys once more, could be accounted for by two factors. Firstly, the reduction in the ordering temperature for Sc was caused by an increase in conduction electron scattering from the solute atoms. Secondly, the Y results could be understood by invoking the 5d band polarization-enhancement effect: the surplus magnetic moment of an alloy (the moment in excess of 7 $\mu_B$ ) is proportional to the c/a ratio of the alloy (Legvold et al., 1977).

To summarize, the change in the saturated magnetic moment and the depression of  $T_c$  caused by different nonmagnetic solutes in Gd suggested that the RKKY interaction was not directly applicable to alloys. The saturated moment varied with the c/a ratio. Remarkably, no correlation with c/a was

found for  $T_c$ , which was found to vary with the residual resistivity. The  $T_c$  dependence can therefore be understood by taking into account the conduction electron mean free path in the alloys. The apparent independence of the excess moment and  $T_c$  may be understood by considering these two effects to be local and global effects respectively (Lagvoid, 1977). Recently, a third explanation of rare-earth alloys has been given by simply considering the modification to the RKKY theory by the introduction of a mean free path dependence only (Young, 1983). The conduction electron mean free path clearly has a major rôle in understanding the magnetism of these materials.

Of special interest to this study is a recent publication by Ito et al. (1987) on the magnetic structure of a  $\text{Gd}_{76.78}\text{Sc}_{23.3}$ <sup>†</sup> single crystal random alloy. This is because one of the samples used for this work had the same nominal composition, having been cut from the same boule. Ito and co-workers performed measurements of magnetization, low field ac susceptibility, electrical resistivity, ultrasonic attenuation and specific heat. Their results are discussed in detail together with those from this work in chapter 8.

#### 1.4 Samples used in this Study

The Gd-Sc samples used in this study were chosen to span the multicritical régime in the magnetic phase diagram and a summary of these, together with the Gd-Y samples studied is given in table 1.1. The  $\text{Gd}_{66}\text{Y}_{34}$  and the  $\text{Gd}_{76.78}\text{Sc}_{23.3}$  sample were grown by B.J. Beaudry at the Ames Laboratories, Iowa. The  $\text{Gd}_{60}\text{Y}_{40}$  sample was grown by D. Hukin at the Clarendon Laboratory, Oxford. The remaining Gd-Sc samples were grown at the Department of Metallurgy and Materials at the University of Birmingham, U.K., by D. Fort. There has been much doubt as to the complete miscibility of Sc

---

<sup>†</sup> believed to be  $\text{Gd}_{75}\text{Sc}_{25}$  at the time of publication.

**Table 1.1 Samples used in this work**

COMPOSITION	SAMPLE DESCRIPTION	SOURCE
Gd <sub>64</sub> Sc <sub>36</sub>	Rectangular block: b and c faces planed a = 5.06mm, b = 4.44mm, c = 4.16mm	Birmingham, 1987
Gd <sub>68</sub> Sc <sub>32</sub>	A-axis disc: Average diameter = 3.32mm Thickness = 3.03mm	Birmingham, 1987
Gd <sub>68</sub> Sc <sub>32</sub>	C-axis disc: Average diameter = 4.11mm Thickness = 3.54mm	Birmingham, 1987
Gd <sub>69</sub> Sc <sub>31</sub>	Rectangular block: b and c faces planed a = 4.79mm, b = 4.45mm, c = 4.64mm	Birmingham, 1988
Gd <sub>70.5</sub> Sc <sub>29.5</sub>	Rectangular block: b and c faces planed a = 4.15mm, b = 4.61mm, c = 4.52mm	Birmingham, 1988
Gd <sub>72</sub> Sc <sub>28</sub>	Rectangular block: a and c faces planed a = 4.51mm, b = 5.05mm, c = 5.76mm	Birmingham, 1988
Gd <sub>75</sub> Sc <sub>25</sub>	Rectangular block: b and c faces planed a = 5.17mm, b = 5.13mm, c = 5.44mm	Birmingham, 1988
Gd <sub>76.7</sub> Sc <sub>23.3</sub>	Rectangular block: all faces planed a = 3.92mm, b = 4.55mm, c = 5.14mm	Ames, 1986
Gd <sub>60</sub> Y <sub>40</sub>	C-axis disc: Diameter = 9.5mm Thickness = 4.0mm	Oxford, 1985?
Gd <sub>66</sub> Y <sub>34</sub>	Rectangular block: all faces planed a = 5.10mm, b = 4.95mm, c = 8.20mm	Ames, 1985?

N.B. Values given are correct in the given digit.

and Gd across the full range of solid solutions because of the much smaller Sc atom (Fort, 1986). However, Gd and Sc have been observed to be completely miscible (Beaudry and Daane, 1963) as have Sc and Y (Beaudry and Daane, 1963). It appears, therefore, that the great similarity between Sc and the other rare-earths in everything but size overcomes the size disparity.

The crystal growth process used in Birmingham for the Gd-Sc alloys involved firstly melting the appropriately weighed out start materials together in a water-cooled copper cold boat by radio-frequency (rf) heating. The resulting ingot was remelted several times to ensure homogeneity. The finger-shaped ingot was then hung vertically by a tungsten wire in an rf tube and heated at 1000-1030°C for 50-70 hours. The rf was finally switched off and the boules allowed to cool naturally. This solid-state crystal growth method is essentially the one which was used at Ames, except that the arc melted buttons were annealed at 1130°C for up to 100 hours. The Oxford Gd-Y sample was also grown using a similar technique.

A spectrographic and vacuum fusion analysis of the start materials for the Gd-Sc alloys is given in table 1.2. No such analysis is available for the Y start material, but it may be expected not to differ too much in impurities from the Gd or Sc. The principal axes of the hcp crystals was determined using the X-ray back-reflection Laue technique, and finally the crystals were spark machined to give parallel planed faces necessary for the ultrasonic work.



Table 1.2 Spectrometric and vacuum fusion analysis  
of Gd and Sc start materials

IMPURITY ELEMENT	IMPURITY IN Gd (Atomic ppm)	IMPURITY IN Sc (Atomic ppm)
Oxygen	216	45
Nitrogen	11	6
Hydrogen	311	401
Carbon	79	232
Fluorine	<25	87
Iron	26	13
Other Rare-Earths	<9	--
Other Elements	<35	<32

## 2

## Neutron Diffraction in the Study of Gd-Y and Gd-Sc Alloys

**Introduction**

Neutron diffraction remains today the most powerful direct method for investigating magnetic structures. The Bragg equation for diffraction,  $n\lambda = 2d\sin\theta$ , is a very useful starting point from which the form of a diffraction pattern may be understood, and its simplicity is indeed appealing. However, this apparent simplicity can be somewhat misleading: why, for instance, should the neutrons be reflected specularly and why can the atoms be treated as grouped into planes? Questions such as these may be answered by using a wave-theoretical approach to diffraction. Moreover, a wave treatment may be readily extended to treat more complex problems such as magnetic neutron diffraction.

It is not the purpose of this chapter to recite the formal theory of thermal neutron scattering which may be found in many good text books (Izyumov and Ozerov (1970), Bacon (1975), Squires (1978), Lovesey (1984)). However an attempt to give a flavour of the theory and its power in relatively simple situations is instructive, always remembering that in the pursuit of brevity any such attempt must be a compromise between the complexity and power of a rigorous formalism and the less rewarding simplicity of a treatment done in a relaxed manner.

The theory will be restricted to the case of elastic scattering with particular emphasis on magnetic diffraction. It is treated using the concept of

the scattering cross-section, which is first applied to a single ionic scatterer to obtain the nuclear and magnetic contributions. The theory is then extended, employing the concept of reciprocal space, to three-dimensional lattices, whereby scattering cross-sections are derived for a variety of magnetic structures. Cross-sections are derived for the hcp crystal lattices and special attention is given to the modifications to the cross-section necessary due to the presence of magnetic domains. Finally, consideration is given to the evaluation of magnetic form factors and nuclear scattering lengths in the Gd-Y and Gd-Sc alloys.

## **2.1 Elastic Nuclear and Magnetic Neutron Diffraction**

When describing neutron diffraction it is helpful to treat the complex interaction between the lattice and neutrons in two parts: firstly the scattering from a single atom which will in general have a nuclear part and a magnetic part, and secondly the diffraction resulting from the superposition of scattered waves from the regular arrangement of these atoms within the crystal.

### **2.1.1 Scattering from a Single Ion**

The basic quantity that is measured in a neutron scattering experiment is the partial differential (p.d.) cross-section. This quantity gives the fraction of neutrons of incident energy  $E$  scattered into an element of solid angle  $d\Omega$  with an energy between  $E'$  and  $E'+dE'$ . The p.d. cross-section is denoted by

$$\frac{d^2\sigma}{d\Omega dE'}$$

where  $\sigma$  is the total cross-section and has the dimension of area. In the work described here, elastic neutron scattering was used to probe the magnetic

structure of the sample in question. i.e. there was no associated energy transfer to or from the target sample. The energy dependence of the p.d. cross-section may therefore be integrated out of the expression to leave the simpler differential cross-section (henceforth referred to as cross-section):-

$$\frac{d\sigma}{d\Omega} = \int_0^{\infty} \left( \frac{d^2\sigma}{d\Omega dE'} \right) dE' \quad \text{elastic scattering} \quad (2.1)$$

We may now find an expression for the cross-section in terms of the incident and scattered neutron wavefunctions associated with the incident and scattered neutron wavevectors,  $\mathbf{k}$  and  $\mathbf{k}'$  respectively. The neutron energy is assumed constant, given by  $E = \hbar^2 k^2 / 2m$  where  $m$  is the neutron mass. The probability of a transition from the plane wave state defined by  $\mathbf{k}$  to the plane wave state  $\mathbf{k}'$  is given by Fermi's Golden Rule:-

$$W_{\mathbf{k} \rightarrow \mathbf{k}'} = \frac{2\pi}{\hbar} \left| \int d\mathbf{r} \psi_{\mathbf{k}'}^* V \psi_{\mathbf{k}} \right|^2 \rho_{\mathbf{k}'}(E') \quad (2.2)$$

where  $V$  is the interaction potential causing the transition and  $\rho_{\mathbf{k}'}(E')$  is the density of final scattered states. It can be shown (Squires, 1978) by the normalized wavefunctions,

$$\begin{aligned} \psi_{\mathbf{k}} &= L^{-3/2} \exp(i\mathbf{k} \cdot \mathbf{r}) \\ \psi_{\mathbf{k}'} &= L^{-3/2} \exp(i\mathbf{k}' \cdot \mathbf{r}), \end{aligned} \quad (2.3)$$

for a large box of volume  $L$ , that the density of final states is

$$\rho_{\mathbf{k}'}(E) = \left( \frac{L}{2\pi} \right)^3 \frac{mk}{\hbar^2} d\Omega. \quad (2.4)$$

The incident neutron flux is given by  $\hbar k / mL^3$ . Together with (2.2) and (2.4) the total cross-section may thus be expressed:-

$$d\sigma = W_{\mathbf{k} \rightarrow \mathbf{k}'} / \text{incident flux}$$

$$\therefore d\sigma = L^6 \left( \frac{m}{2\pi\hbar^2} \right)^2 \left| \int d\mathbf{r} \psi_{\mathbf{k}}^* V \psi_{\mathbf{k}} \right|^2 d\Omega.$$

So with the notation

$$\int d\mathbf{r} \psi_{\mathbf{k}}^* V \psi_{\mathbf{k}} = \frac{1}{L^3} \langle \mathbf{k}' | V | \mathbf{k} \rangle,$$

we get the result

$$\frac{d\sigma}{d\Omega} = \left( \frac{m}{2\pi\hbar^2} \right)^2 |\langle \mathbf{k}' | V | \mathbf{k} \rangle|^2. \quad (2.5)$$

We now turn to the form of the interaction potential,  $V$ , with the further assumption that the scattering takes place from the bound nucleii. Because the wavelength of a thermal neutron ( $\sim 1\text{\AA}$ ) is much larger than a characteristic nuclear dimension, scattering from the nucleus will be isotropic and the interaction may therefore be characterized by a single parameter  $b$ , called the nuclear scattering length. Within the Born approximation, the only form of  $V(\mathbf{r})$  which gives isotropic scattering is a delta function. For a nucleus at a position defined by  $\mathbf{R}$ , the Fermi pseudo-potential is defined as

$$V(\mathbf{r}) = \frac{2\pi\hbar^2}{m} b \delta(\mathbf{r} - \mathbf{R}). \quad (2.6)$$

It now follows from (2.5) and (2.6),

$$\begin{aligned} \frac{d\sigma}{d\Omega} &= b^2 \left| \int d\mathbf{r} \exp(-i\mathbf{k}' \cdot \mathbf{r}) \delta(\mathbf{r}) \exp(i\mathbf{k} \cdot \mathbf{r}) \right|^2 \\ \therefore \frac{d\sigma}{d\Omega} &= b^2. \end{aligned} \quad (2.7)$$

Having found the form of the cross-section for nuclear scattering, we now turn to the scattering from a magnetic atom with a localized moment. We assume the moment to arise from electron spin only. The interaction between the moment of the neutron,  $\mu$ , and that of a spinning electron is a dipole-dipole

interaction which may no longer be assumed to be short ranged. Consequently, the scattering will no longer be isotropic.

The potential of a neutron with dipole moment  $\mu$  in a magnetic field  $H$  is

$$V(r) = -\mu \cdot H \quad (2.8)$$

We may write this in terms of the neutron spin,  $\sigma = \mu / \mu_N$  where  $\gamma$  is the gyromagnetic ratio of the neutron ( $= -1.91$ ) and  $\mu_N$  is the nuclear magneton:

$$V(r) = -\gamma \mu_N \sigma \cdot H \quad (2.9)$$

The field produced by a spinning electron is

$$H_e = -2\mu_B \text{curl} \left( \frac{s \wedge R}{R^2} \right), \quad (2.10)$$

where  $\mu_B$  is the Bohr magneton and  $s$  the electron spin. Therefore, the potential of a neutron in the field of the  $i$ th spinning electron can be written

$$V(r) = 2\gamma \mu_N \mu_B \sigma \cdot W_{s_i}, \quad (2.11)$$

where  $W_{s_i}$  is defined as  $\text{curl} [(s_i \wedge R) / R^2]$ . We determine  $\langle k' | W_{s_i} | k \rangle$  by integrating over the space coordinates  $r$  of the neutron:-

$$\langle k' | W_{s_i} | k \rangle = \int dr \exp(-ik' \cdot r) \text{curl} \left( \frac{s_i \wedge R}{R^2} \right) \exp(ik \cdot r). \quad (2.12)$$

It may be shown (Squires 1978) that the right hand side may be simplified:-

$$\langle k' | W_{s_i} | k \rangle = 4\pi \exp(ik \cdot r_i) (\hat{k} \wedge (s_i \wedge \hat{k})) \quad (2.13)$$

where the scattering vector  $\kappa = k - k'$ . We now consider the potential  $W_s$  of a neutron in the field of an ion with a localised spin-only moment. Now we have

$$\langle k' | W_s | k \rangle = 4\pi \sum_i \exp(ik \cdot r_i) (\hat{k} \wedge (\hat{A}_i \wedge \hat{k})) S_i \quad (2.14)$$

where  $S$  is the ionic spin. In order to account for the spatial distribution of the electrons producing the moment, we introduce the magnetic form factor:-

$$f_m(\kappa) = \int \rho(r) \exp(i\kappa \cdot r) dr, \quad (2.15)$$

where  $\rho(r)$  is the normalized electron spin density.  $f_m(\kappa)$  is clearly just the Fourier transform of the electron spin density. We denote the vector quantity in curly brackets (eqn. 2.14) in the usual way by  $q$ , the magnetic interaction vector. From (2.14) and (2.15) we then have

$$\langle k | W_B | k \rangle = 4\pi f_m(\kappa) S q. \quad (2.16)$$

Therefore,

$$\frac{d\sigma}{d\Omega} = \left(\frac{m}{2\pi\hbar^2}\right)^2 (2\mu_B)^2 g^2 (4\pi)^2 f_m(\kappa)^2 S^2 |q|^2. \quad (2.17)$$

It should be noted that this cross-section is independent of the neutron spin; this is to be expected for unpolarized neutron scattering. (For a more rigorous treatment showing how the independence on  $g$  arises, see Squires (1978).) Further simplification of the expression may be made by writing it in terms of  $r_0$ , the classical electron radius ( $= e^2/mc^2$  where the symbols have their conventional meaning):-

$$\frac{d\sigma}{d\Omega} = (\gamma r_0)^2 f_m(\kappa)^2 S^2 |q|^2. \quad (2.18)$$

Finally, one may express the scalar terms as a single factor  $p^2$ ,  $p$  being the magnetic scattering length,

$$\frac{d\sigma}{d\Omega} = p^2 |q|^2. \quad (2.19)$$

It is now clear that the angular dependence of the coherent elastic magnetic scattering is more complicated than the nuclear scattering, since it is determined by the additional angular dependence of the magnetic form factor as well as  $q$  (which itself depends on the orientation of the scattering vector

with respect to the moment vector,  $\mathbf{S}$ ). We shall now proceed to describe neutron diffraction from a regular crystal lattice having derived scattering from a single ion:-

$$\frac{d\sigma}{d\Omega} = b^2, \quad \text{nuclear scattering}$$

$$\frac{d\sigma}{d\Omega} = p^2 |\mathbf{q}|^2, \quad \text{magnetic scattering}$$

### 2.1.2 Scattering from a 3D Bravais Lattice

A Bravais lattice may be generated by three basis vectors,  $\mathbf{a}_i$  ( $i=1,2,3$ ) and the position of any atom within the lattice may be written

$$\mathbf{l}_i = \sum_j n_j \mathbf{a}_j, \quad n_j, \text{ integer}$$

Consider a plane wave with wavevector  $\mathbf{k}$  incident on the lattice. We know that each atom is the source of a spherical elastically scattered wave and we wish to find the resultant amplitude scattered with wavevector  $\mathbf{k}'$  by the lattice. We can write the phases of the waves scattered by atoms at positions  $\mathbf{l}_i$  from the origin as

$$\frac{2\pi}{\lambda} \mathbf{l}_i \cdot (\mathbf{k}' - \mathbf{k}) = m2\pi \quad m, \text{ integer} \quad (2.20)$$

for constructive interference. We define the scattering vector  $\boldsymbol{\kappa}$  by

$$\frac{2\pi}{\lambda} (\mathbf{k}' - \mathbf{k}) = \boldsymbol{\kappa} \quad (2.21)$$

The condition that all scattered waves from all atoms add in phase is now expressed

$$\sum_i n_i \mathbf{a}_i \cdot \boldsymbol{\kappa} = m2\pi. \quad (2.22)$$



These are the Laue equations. It is clear that these equations can be satisfied for all values of  $n_i$  only if  $\mathbf{a}_i \cdot \mathbf{x}$  is a multiple of  $2\pi$ .

$$\mathbf{a}_i \cdot \mathbf{x} = 2\pi H_i. \quad (2.23)$$

A vector,  $\boldsymbol{\epsilon} = \mathbf{x}$ , may now be defined such that all three equations of (2.23) are simultaneously satisfied:-

$$\boldsymbol{\epsilon} = 2\pi H_i \mathbf{a}_i^*, \quad (2.24)$$

with  $\mathbf{a}_i \cdot \boldsymbol{\epsilon} = 2\pi H_i$  and  $\mathbf{a}_i \cdot \mathbf{a}_k^* = \delta_{ik}$ .

If  $H_i$  takes on all possible values, the vectors  $\boldsymbol{\epsilon}$  associated with  $H_i$  define a lattice called the reciprocal lattice where the basis vectors of the reciprocal lattice are given by

$$\begin{aligned} \mathbf{a}_1^* &= \frac{2\pi}{v_0} (\mathbf{a}_2 \wedge \mathbf{a}_3) \\ \mathbf{a}_2^* &= \frac{2\pi}{v_0} (\mathbf{a}_3 \wedge \mathbf{a}_1) \\ \mathbf{a}_3^* &= \frac{2\pi}{v_0} (\mathbf{a}_1 \wedge \mathbf{a}_2) \end{aligned} \quad (2.25)$$

where  $v_0$  is the volume of the real space unit cell and is equal to the triple scalar product  $\mathbf{a}_1 \cdot (\mathbf{a}_2 \wedge \mathbf{a}_3)$ . The reciprocal lattice, therefore, is built up (as in a crystal lattice) from three basis vectors which define all the points in the lattice. Also, from its definition, the vectors,  $\boldsymbol{\epsilon}$ , describing the points in the reciprocal lattice are vectors which satisfy the Laue equations, and therefore represent conditions of constructive interference. The beauty of the concept of the reciprocal lattice now emerges, since it is clear that if the scattering vector coincides with a reciprocal lattice vector, the conditions for constructive interference will be necessarily satisfied. We may thus express the condition for coherent scattering very simply as

$$\mathbf{k}' - \mathbf{k} = \mathbf{x} = \boldsymbol{\epsilon}. \quad (2.26)$$

Having defined a useful notation, we return to the problem of evaluating the cross-section for a Bravais lattice defined by the vectors  $\mathbf{l}_i$ . This is simply the sum of the scattered waves from each scattering centre in the lattice:-

$$\frac{d\sigma}{d\Omega} = b^2 \left| \sum_i \exp(i\kappa \cdot \mathbf{l}_i) \right|^2. \quad (2.27)$$

When  $\kappa$  is equal to a reciprocal lattice vector  $\tau$ , this expression is very large due to all the terms in the sum adding in phase. If  $\kappa$  moves away from a reciprocal lattice vector, the terms become rapidly out of phase and the sum falls to a negligible value. For a large crystal, it may be shown that

$$\left| \sum_i \exp(i\kappa \cdot \mathbf{l}_i) \right|^2 = N \frac{(2\pi)^3}{v_0} \sum_{\tau} \delta(\kappa - \tau). \quad (2.28)$$

Hence,

$$\frac{d\sigma}{d\Omega} = N \frac{(2\pi)^3}{v_0} b^2 \sum_{\tau} \delta(\kappa - \tau). \quad (2.29)$$

$N$  is the total number of scattering centres. We see that the scattered intensity occurs in the form of delta functions centred at each reciprocal lattice point. In reality, the elastically diffracted peak assumes a width in reciprocal space which is inversely proportional to the number of scattering centres involved in the scattering.

For a single domain Bravais ferromagnet with identical magnetic ions, the magnetic cross-section may be derived in a similar way. However, it is clear that the expression will be the same as (2.29), but with  $b^2$  replaced by the magnetic equivalent,  $p^2 |q|^2$ . In its full form,

$$\frac{d\sigma}{d\Omega} = (\gamma r_0)^2 f_m(\kappa)^2 S^2 |q|^2 N \frac{(2\pi)^3}{v_0} \sum_{\tau} \delta(\kappa - \tau). \quad (2.30)$$

Immediately, we see that the magnetic Bragg scattering occurs at exactly the same reciprocal lattice points as the nuclear scattering. This is also true of non-Bravais ferromagnets.

### 2.1.3 Ferromagnetic Scattering from a 3D non-Bravais Crystal Lattice

We may readily generalize to the case of a lattice with more than one atom per unit cell by introducing vectors  $\mathbf{d}_j$  which describe the positions of the atoms  $j$  within the unit cell. The vectors  $\mathbf{l}_j$  used previously now define the corners of the unit cells, and in a similar manner to (2.27),

$$\frac{d\sigma}{d\Omega} = \left| \sum_{ij} b_j \exp(i\mathbf{x} \cdot \mathbf{l}_i) \exp(i\mathbf{x} \cdot \mathbf{d}_j) \right|^2, \quad (2.31)$$

From (2.28),

$$\frac{d\sigma}{d\Omega} = N \frac{(2\pi)^3}{v_0} \sum_{\mathbf{\kappa}} \delta(\mathbf{\kappa} - \mathbf{\kappa}') |F_N|^2 \quad (2.32)$$

where  $F_N$  is the nuclear unit cell structure factor:

$$F_N = \sum_j b_j \exp(i\mathbf{x} \cdot \mathbf{d}_j). \quad (2.33)$$

Notice how the scattering length has been absorbed in the structure factor to account for different atoms within the unit cell. In general,  $b$  will depend on the particular isotope and spin of the scattering ion. In the case of unit cells with identical ions, or in cases where they may be treated as such (as in a random alloy), we can rewrite the structure factor in terms of an average scattering length and a geometrical structure factor,  $G_{\mathbf{hkl}}$ :

$$F_N = \bar{b} G_{\mathbf{hkl}}. \quad (2.34)$$

$G_{hkl}$  is simply a function of the positions of the scattering centres within the unit cell. It is readily calculable for a given crystal structure (see next section). It follows,

$$\frac{d\sigma}{d\Omega} = N \frac{(2\pi)^3}{v_0} b^2 G_{hkl}^2 \sum_{\tau} \delta(\kappa - \tau) . \quad (2.35)$$

For a ferromagnet, the cross-section becomes

$$\frac{d\sigma}{d\Omega} = N \frac{(2\pi)^3}{v_0} \sum_{\tau} \delta(\kappa - \tau) |F_M|^2 , \quad (2.36)$$

with

$$F_M = \sum_j p_j q_j \exp(i\kappa \cdot d_j) . \quad (2.37)$$

(c.f. (2.32) and (2.33).) Since magnetic and nuclear unit cells coincide, we get

$$\frac{d\sigma}{d\Omega} = (v_0)^{-2} f_m(\kappa)^2 S^2 |q|^2 G_{hkl}^2 N \frac{(2\pi)^3}{v_0} \sum_{\tau} \delta(\kappa - \tau) . \quad (2.38)$$

The magnetic symmetry of a magnetically ordered material will always be lower than the symmetry of the atomic lattice. Therefore, in the absence of an applied field, the symmetry-breaking effect of magnetic ordering will generally lead to the existence of magnetic domains. To obtain the cross-section we must average over all possible orientations of these domains i.e. over the 'easy' axes for S. Thus the cross-section will be modified by the substitution of  $\langle q \rangle$  for  $q$ , where the triangular brackets denote the average value. We leave the calculation of  $\langle q \rangle$  to the next section.

#### 2.1.4 Helimagnetic Scattering from a 3D non-Bravais Crystal Lattice

The treatment of scattering from helimagnets is more complex than for simple ferromagnets or antiferromagnets since these structures do not,

strictly speaking, have a magnetic unit cell. Following Squires, we start from a more general form of the elastic magnetic cross-section.

$$\frac{d\sigma}{d\Omega} = (\gamma r_0)^2 f_m(\kappa)^2 \sum_{\alpha\beta} (\delta_{\alpha\beta} - \hat{\kappa}_\alpha \hat{\kappa}_\beta) \sum_{\mathbf{l}\mathbf{l}'} \langle S_l^\alpha \rangle \langle S_{l'}^\beta \rangle \exp[i\mathbf{x} \cdot (\mathbf{l} - \mathbf{l}')] \quad (2.39)$$

This expression is essentially the same as (2.30) except that  $|\mathbf{q}|^2$  and  $S$  have been written as time-independent correlators. We now let  $\mathbf{q}$  be a vector in the direction of the helical axis of magnitude  $2\pi$  divided by the pitch of helix. The helical axis we take as the hexagonal  $c$ -axis. The spin components have the form

$$\langle S_l^x \rangle = \langle S \rangle \cos(\mathbf{q} \cdot \mathbf{l}), \quad \langle S_l^y \rangle = \langle S \rangle \sin(\mathbf{q} \cdot \mathbf{l}), \quad \langle S_l^z \rangle = 0. \quad (2.40)$$

Inserting these values into (2.39) we get

$$\begin{aligned} \frac{d\sigma}{d\Omega} &= (\gamma r_0)^2 f_m(\kappa)^2 \langle S \rangle^2 \sum_{\mathbf{l}\mathbf{l}'} \exp[i\mathbf{x} \cdot (\mathbf{l} - \mathbf{l}')] \left[ \left(1 - \frac{1}{2} \hat{\kappa}_x^2 + \hat{\kappa}_y^2\right) \cos(\mathbf{q} \cdot (\mathbf{l} - \mathbf{l}')) \right. \\ &\quad \left. + \frac{1}{2} (\hat{\kappa}_y^2 - \hat{\kappa}_x^2) \cos(\mathbf{q} \cdot (\mathbf{l} + \mathbf{l}')) - \hat{\kappa}_x \hat{\kappa}_y \sin(\mathbf{q} \cdot (\mathbf{l} + \mathbf{l}')) \right]. \end{aligned} \quad (2.41)$$

Then,

$$\begin{aligned} \frac{d\sigma}{d\Omega} &= (\gamma r_0)^2 f_m(\kappa)^2 \langle S \rangle^2 \sum_{\mathbf{l}\mathbf{l}'} \exp[i\mathbf{x} \cdot (\mathbf{l} - \mathbf{l}')] \left[ \left(1 - \frac{1}{2} \hat{\kappa}_x^2 + \hat{\kappa}_y^2\right) \cos(\mathbf{q} \cdot (\mathbf{l} - \mathbf{l}')) \right. \\ &\quad \left. + \operatorname{Re} \left( \frac{1}{2} \hat{\kappa}_y + i \hat{\kappa}_x \right)^2 \exp[i\mathbf{q} \cdot (\mathbf{l} + \mathbf{l}')] \right]. \end{aligned} \quad (2.42)$$

The second term will vanish on summing over  $\mathbf{l}$  and  $\mathbf{l}'$  since we know that  $\mathbf{q}$  is not equal to a reciprocal lattice vector. (If it was, there would be ferromagnetism.) Hence,

$$\begin{aligned} \frac{d\sigma}{d\Omega} &= (\gamma r_0)^2 f_m(\kappa)^2 \langle S \rangle^2 \left(1 - \frac{1}{2} (\hat{\kappa}_x^2 + \hat{\kappa}_y^2)\right) \sum_{\mathbf{l}\mathbf{l}'} \exp[i\mathbf{x} \cdot (\mathbf{l} - \mathbf{l}')] \cos(\mathbf{q} \cdot (\mathbf{l} - \mathbf{l}')) \quad (2.43) \\ &= (\gamma r_0)^2 f_m(\kappa)^2 \langle S \rangle^2 \frac{1}{4} (1 + \hat{\kappa}_z^2) \sum_{\mathbf{l}\mathbf{l}'} \left[ \exp[i(\mathbf{x} + \mathbf{q}) \cdot (\mathbf{l} - \mathbf{l}')] \right. \\ &\quad \left. + \exp[i(\mathbf{x} - \mathbf{q}) \cdot (\mathbf{l} - \mathbf{l}')] \right]. \end{aligned} \quad (2.44)$$

$$\frac{d\sigma}{d\Omega} = (\gamma_0)^2 f_m(\kappa)^2 < S > \frac{2N(2\pi)^3}{4v_0} (1 + \frac{1}{2}) \sum_{\epsilon} \{ \delta(\kappa + q - \epsilon) + \delta(\kappa - q - \epsilon) \} \quad (2.45)$$

Equation (2.45) shows that magnetic Bragg scattering occurs when  $\kappa = \epsilon \pm q$  i.e. each nuclear peak is flanked by a pair of magnetic satellites separated from the nuclear peak in the direction of  $q$  (transposed in reciprocal space). These are normally indexed as  $hkl^{\pm}$ .

## 2.2 Diffraction from Gd-Y and Gd-Sc Alloys

### 2.2.1 The Reciprocal Lattice

We now look at particular aspects of neutron diffraction from Gd-Y and Gd-Sc. First, we turn to the form of the reciprocal lattice for the hcp structure. The vectors defining the real space lattice and its associated reciprocal lattice are related by the equation

$$a_i \cdot a_j^* = \delta_{ij}$$

derived in section 2.1.2. This tells us that  $a_i^*$  is perpendicular to the  $a_i$  planes of the crystal lattice. Also, from (2.24),  $|a_i^*|$  is equal to  $2\pi$  divided by the plane spacing of  $a_i$ . The reciprocal lattice constructed for the hcp structure is shown in figures 2.1 and 2.2. Figure 2.1 is the reciprocal lattice of the basal plane and, like the real space basal plane, it has 6-fold symmetry. This is the  $a^*b^*$  plane. The  $a^*c^*$  plane is shown separately in figure 2.2.

A particularly informative way of picturing coherent elastic scattering from a lattice, used in conjunction with the reciprocal lattice, is the Ewald sphere construction. This is a geometric construction representing a sphere of possible elastic scattering. Examples of such a construction are given in figures 2.1 and 2.2. The geometry of the scattering triangle may be used to recover the Bragg equation very simply:-

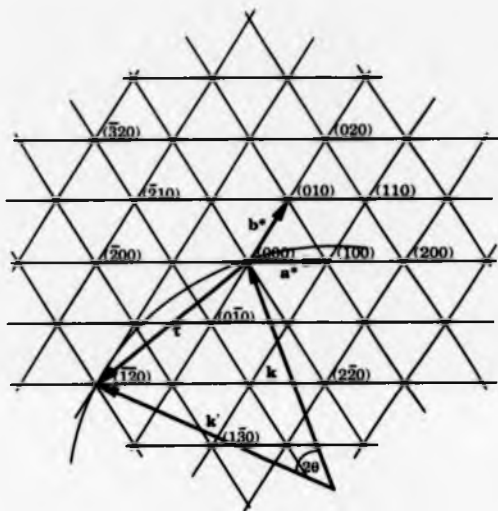


Figure 2.1 Hexagonal basal plane reciprocal space and Ewald sphere construction.

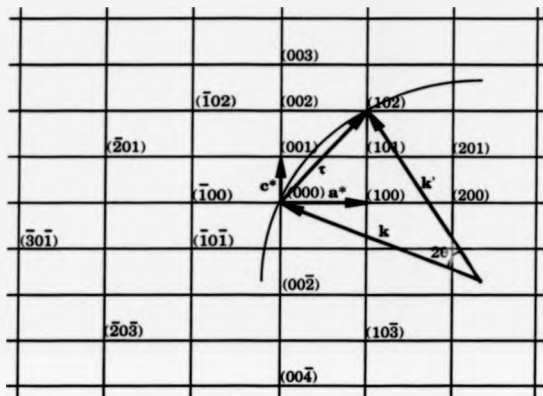


Figure 2.2 Hexagonal  $a^*c^*$  plane reciprocal space and Ewald sphere construction.



$$\sin\theta = \frac{\tau}{2\lambda}$$

but  $\tau=2\pi/d$ ,

$$\lambda=2d\sin\theta.$$

The Ewald sphere construction will be used in the discussion of resolution effects in chapter 3.

### 2.2.2 The Geometric Structure Factor

The hcp crystal structure of Gd-Y and Gd-Sc is not a Bravais lattice, therefore a geometric structure factor,  $G_{hkl}$ , is used in the scattering cross-section to account for the second atom in the unit cell. Defining the position vectors of the nuclei as

$$\begin{aligned} \mathbf{d}_1 &= (0, 0, 0), \\ \mathbf{d}_2 &= \left(\frac{2}{3}, \frac{1}{3}, \frac{1}{2}\right), \end{aligned} \quad (2.46)$$

evaluation of  $G_{hkl}^2$  is simply a matter of summing the scattered waves from these two points:-

$$G_{hkl} = 1 + \exp\left(i\left(\frac{2h}{3} + \frac{k}{3} + \frac{l}{2}\right)\right). \quad (2.47)$$

It follows that

$$G_{hkl}^2 = 2 + 2\cos\left(2\pi\left(\frac{2h}{3} + \frac{k}{3} + \frac{l}{2}\right)\right). \quad (2.48)$$

Values of  $G_{hkl}^2$  are given in table (2.1) for several of the more important low angle reflections.

### 2.2.3 Ferromagnetic Structures in Gd-Y and Gd-Sc Alloys

For a single domain ferromagnet, it can be seen from (2.38) that for a particular reflection, the magnetic cross-section is proportional to  $S^2|q|^2$ . For a multi-domain ferromagnet, the situation is more complex. Let us assume the magnetization direction for a particular domain in a ferromagnet makes

Table 2.1 Relative intensities of some low-angle reflections

REFLECTION (hkl)	$G_{hkl}^2$
001	0
002	4
003	0
004	4
100	1
101	3
102	1
103	3
104	1
200	1
201	3
202	1
203	3

an angle  $\theta$  to the  $c$ -axis. Because of the other domains within the sample, this does not uniquely define the moment orientation within the sample. Each domain will have a different value of  $q$  and that particular value of  $q$  will also depend on the orientation of the scattering vector for the reflection under consideration. Let us now evaluate  $q$  for two important reflections, the  $h00$  and  $00l$  type reflections. We choose to represent these reflections by the  $100$  and  $002$  respectively. Immediately we know  $\kappa_{100}$  lies along  $a^*$  and  $\kappa_{002}$  lies along  $c^*$ . Denoting the angular displacement of the basal plane component of magnetisation from the  $a^*$  axis by  $\phi$  (figure 2.3), and using a variation on the expansion of  $|q|^2$ ,

$$|q|^2 = [1 - (\hat{k} \cdot \hat{S})^2], \quad (2.48)$$

for the  $100$  we have

$$\begin{aligned} |q_{100}|^2 &= [1 - (\hat{k}_{100} \cdot \hat{S})^2], \\ &= 1 - \cos^2 \alpha, \end{aligned} \quad (2.50)$$

where  $\alpha = \cos^{-1}(\sin \theta \cos \phi)$ .

$$\therefore |q_{100}|^2 = 1 - \sin^2 \theta \cos^2 \phi. \quad (2.51)$$

Also, for the  $002$ ,

$$\begin{aligned} |q_{002}|^2 &= 1 - \cos^2 \theta, \\ \therefore |q_{002}|^2 &= \sin^2 \theta. \end{aligned} \quad (2.52)$$

$|q|^2$  is simply the square of the projection of the magnetization onto the scattering plane defined by  $\kappa$ , and consequently there will be no scattering from a domain whose magnetization vector is parallel to the scattering vector.

For a particular Bragg reflection it is important to average  $q$  over the possible domain orientations. For the canted ferromagnetic structure it may be assumed that the domain easy directions lie in two cones centred on  $\pm c^*$  and with a semi-cone angle of  $\theta$ . Clearly  $|q_{002}|^2$  will remain unchanged after domain averaging, since all moments will have the same basal plane component.  $|q_{100}|^2$  is, however, highly sensitive to domain orientation. For a uniform distribution of domains about  $c^*$ :-

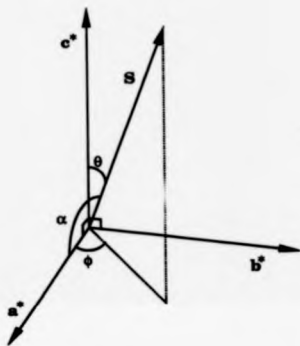


Figure 2.3 Arbitrary moment vector and relationship to reciprocal lattice.

$$\langle |q_{100}|^2 \rangle = \frac{\sin^2 \theta}{2} + \cos^2 \theta, \quad (2.53)$$

where the triangular brackets denotes the average value. The first term represents averaging over different basal plane directions and the second over the two c-axis directions. In summary, for a multi-domained canted ferromagnetic sample with no applied field:

$$\left( \frac{d\sigma}{d\Omega} \right)_{100} \propto \langle (Sq)_{100}^2 \rangle = S^2 \left( \frac{\sin^2 \theta}{2} + \cos^2 \theta \right), \quad (2.54)$$

$$\left( \frac{d\sigma}{d\Omega} \right)_{002} \propto \langle (Sq)_{002}^2 \rangle = S^2 \sin^2 \theta. \quad (2.55)$$

#### 2.2.4 Modulated Structures in Gd-Y and Gd-Sc Alloys

We shall now examine in more detail the diffraction conditions for modulated structures with: propagation directions along the  $c^*$  axis. Such structures give rise to magnetic Bragg reflections or 'satellites' associated with each reciprocal lattice point ( $q$  permitting). The satellites are found on lattice rows parallel to the  $c^*$  axis. The existence of a single pair of satellites implies a structure in which the scattering amplitudes of the atoms are modulated sinusoidally. From the location of the satellites on lines parallel to  $c^*$  it may be concluded that the wavevector of the modulation is parallel to that direction. The absence of satellites of  $00l^{\pm}$  type implies a uniaxial configuration in which the moments are parallel or anti-parallel to the c-axis. This follows because the neutron senses only the component of the moment which is perpendicular to the scattering vector.

With these points in mind, we derive the intensities of magnetic reflections for a conical helical structure described by the spin components:-

$$S_{nx} = S_{\perp} \cos(n\alpha), \quad S_{ny} = S_{\perp} \sin(n\alpha), \quad S_{nz} = S_{\parallel},$$

where  $n$  denotes the index of the layer in which the moment lies. In this configuration, there is a ferromagnetic component along the  $c$ -axis so that there is magnetic intensity residing on nuclear reciprocal lattice points which are not of the 001 type. Satellites due to the helical part of the structure are, however, still observed at 001 lattice points. For a given reflection, the conical configuration gives rise to intensities:-

$$\left(\frac{d\sigma}{d\Omega}\right)_{hkl} = (\gamma r_0)^2 f_m(\kappa)^2 G_{hkl}^2 S_{\parallel}^2 \sin^2 \zeta, \quad (2.56)$$

$$\left(\frac{d\sigma}{d\Omega}\right)_{hkl\pm} = (\gamma r_0)^2 (f_m(\kappa)^2)^2 G_{hkl}^2 S_{\perp}^2 \frac{1}{4} (1 + \cos^2 \zeta), \quad (2.57)$$

where  $\zeta$  is the angle between the scattering vector and  $c^*$ , and  $f_m(\kappa)^2$  is the form factor evaluated for each satellite separately. Note that the magnetic cross-section is proportional to  $(Sq)^2$  in (2.56) and (2.57); it has value  $S_{\parallel}^2 \sin^2 \zeta$  and  $S_{\perp}^2 \frac{1}{4} (1 + \cos^2 \zeta)$  respectively. If the periodicity of the helix is not too short,  $f_m(\kappa)^2$  may be averaged between the two satellites, or the value at the nuclear peak may be taken. For the 100 and 002 reflections, we have:-

$$\left(\frac{d\sigma}{d\Omega}\right)_{100} = \langle (Sq)_{100}^2 \rangle = S_{\parallel}^2, \quad (2.58)$$

$$\left(\frac{d\sigma}{d\Omega}\right)_{100\pm} = \langle (Sq)_{100\pm}^2 \rangle = \frac{1}{4} S_{\perp}^2, \quad (2.59)$$

$$\left(\frac{d\sigma}{d\Omega}\right)_{002} = \langle (Sq)_{002}^2 \rangle = 0, \quad (2.60)$$

$$\left(\frac{d\sigma}{d\Omega}\right)_{002\pm} \approx \langle S_{002}^2 \rangle = \frac{1}{2} S_{\perp}^2. \quad (2.61)$$

Diffraction data from a simple basal plane helix may also be calculated from (2.56) and (2.57). In this case there is no magnetic contribution to the normal lattice sites ( $S_{\parallel}=0$ ).

### 2.2.5 Nuclear Scattering Length

The nuclear scattering length,  $b$ , is the single parameter which describes neutron-nuclear scattering, and it has a value typically of the order of the nuclear radius. It is generally expressed as a complex quantity. For most elements, the imaginary component is negligible, however on approaching the scattering resonance of a nucleus it becomes increasingly important. This is true of the Gd isotopes scattering thermal neutrons. In such cases, one would ideally like to know the boundary conditions at the nuclear surface in order to determine the scattering length of a particular nucleus. At present, such a calculation is not possible, however it is possible to express these conditions in terms of quantities relating to the compound nucleus formed by the addition of a neutron. The method is to assume a single resonance energy level in the compound nucleus (Breit and Wigner, 1936) which then allows the scattering length to be expressed:-

$$b = b' - ib'' = R + \frac{\frac{1}{2}\Gamma_a(r)k^{-1}}{(E-E_r) + \frac{1}{2}i\Gamma} \quad (2.62)$$

The two terms are referred to as 'potential' and 'resonance' terms. The potential term is always positive and is equal to the nuclear radius.  $E_r$  is the resonance energy of the compound nucleus and  $E$  is the incident neutron energy.  $\Gamma = \Gamma_a^{(r)} + \Gamma_n^{(r)}$  which are the resonance widths for absorption and re-emission of the incident neutron respectively.

Bates (1985) has modelled the behaviour of  $\bar{b}$  and  $\bar{b}'$  for natural Gd near resonance. This necessarily involves averaging over all the isotopes, since  $b$  will be different for each. The resonance level was taken at 1.8 Å and the resonance widths were taken to be

$$\Gamma_n^{(r)} = 1.65 \times 10^{-15} \text{ eV},$$

$$\Gamma = \Gamma_n^{(r)} = 0.108 \text{ (eV)}.$$

Although only approximate, these values were found to model measured values of  $\bar{b}$  and  $\bar{b}'$  very well. Plots of  $\bar{b} = \sqrt{|\bar{b}^2|}$ ,  $\bar{b}'$  and  $\bar{b}''$  as a function of incident neutron wavelength are shown in figure 2.4.

For a random Gd-Y or Gd-Sc alloy, the scattering potential will vary randomly from point to point throughout the sample due to different elements and different isotopes of each element. It is only the mean potential of the scattering system (i.e. the same scattering system with  $b$  replaced by  $\bar{b}_{\text{alloy}}$  everywhere) which may give rise to interference effects (coherent scattering). For a particular alloy, therefore,  $\bar{b}_{\text{alloy}}$  will be an average over  $\bar{b}$  for each constituent element,

$$\bar{b}_{\text{alloy}} = \sum_i c_i \bar{b}_i, \quad (2.63)$$

where  $\bar{b}_i$  is the mean scattering length and  $c_i$  is the concentration of the  $i$  element.

Y and Sc may be considered to exhibit no resonances for thermal neutrons. Their scattering lengths have been taken as (Lovesey 1984)

$$\bar{b}_Y = 0.775 \times 10^{-14} \text{ m},$$

$$\bar{b}_{\text{Sc}} = 1.23 \times 10^{-14} \text{ m}.$$

Together with a value for  $\bar{b}_{\text{Gd}}$  derived for the appropriate neutron wavelength (as already discussed),  $\bar{b}_{\text{alloy}}$  may be readily determined (table 2.2).



Figure 2.4 Gd Scattering Lengths vs.  
Neutron Wavelength

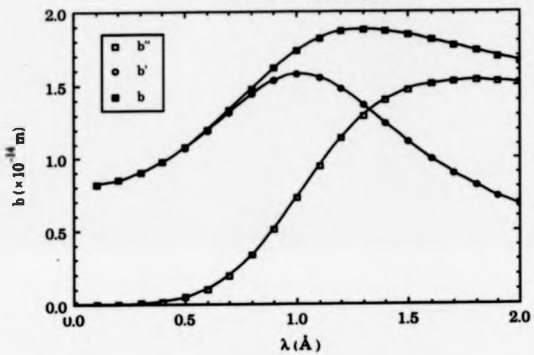


**Table 2.2 Nuclear scattering lengths of alloys used in this work**

ALLOY	$b_{\text{alloy}}^2$
Gd <sub>84</sub> Sc <sub>16</sub>	$1.24 \times 10^{-28} \text{ m}^2$
Gd <sub>88</sub> Sc <sub>12</sub>	1.22
Gd <sub>70.6</sub> Sc <sub>29.4</sub>	1.21
Gd <sub>72</sub> Sc <sub>28</sub>	1.20
Gd <sub>75</sub> Sc <sub>25</sub>	1.19
Gd <sub>76.7</sub> Sc <sub>23.3</sub>	1.19
Gd <sub>80</sub> Y <sub>20</sub>	0.879
Gd <sub>88</sub> Y <sub>12</sub>	0.910

N.B. Values given are uncertain in the last digit.

### 2.2.6 Gd Magnetic Form Factor

In the absence of a fully reliable calculation of the 4f form factor for Gd (which requires an accurate knowledge of the band structure), the measurements of the magnetic form factor by Moon and Koehler (1971) on the low absorbing isotope  $^{160}\text{Gd}$  at 96 K have been used in this study. In that publication, the theoretical calculations of the form factor by Blume et al. (1962) were used to fit the data. Blume's calculations used non-relativistic Hartree-Fock wavefunctions for free trivalent rare-earth ions. By taking a value for the 4f moment of  $5.63\mu_B$  at 96 K, excellent agreement was obtained with the measured values for  $\sin\theta/\lambda > 0.55\text{\AA}^{-1}$ . However the value taken for the moment was too small to be realistic, and the fit was poor at low angles.

Figure 2.5 shows a comparison of the measured points (to which a curve has been fitted) and points taken from Blume's theoretical curve which has been normalised to a 4f moment of  $6.42\mu_B$  (that expected for the 4f contribution at 96 K). From the fit it is clear that the wavefunctions used in the theory are not fully representative of the situation. The experimental line falls below the calculated points and thus the free ion wavefunctions are more contracted than the 4f metallic wavefunctions. At large angles, the data is well fitted by the theory, indicating the spin distribution is spherically symmetric, as it should be.

Stassis et al. (1977) used relativistic wavefunctions to evaluate the magnetic scattering resulting from the coupling of the magnetic moment of the neutron to the relativistic ionic current. Therefore these calculations differed in two principal ways from earlier work. 1) Use of relativistic wavefunctions and 2) relativistic treatment of the interaction between the neutron moment and the ionic current. The Dirac-Fock calculations yielded an electronic density more expanded in space than the non-relativistic H-F

treatment. This is due to the velocity dependence of the electronic mass which causes the inner orbits to contract more than the outer ones (Freeman and Desclaux, 1972). As a result of this relativistic core contraction, the 4f electrons see a less attractive nuclear potential and the 4f-electron radial density is more expanded than are nonrelativistic radial densities. The D-F calculations are seen to fit the data of Moon very closely (fig. 2.5).

In considering the magnetic properties of the rare-earths, it is evident that the 4f electrons are responsible for almost all the observed bulk magnetization. However the RKKY interaction which couples the localized 4f electrons also promotes the magnetic ordering of the electrons lost to the conduction band since they become effectively polarized. Furthermore it is easy to see that the form factor of the conduction electrons will fall off more steeply with increasing Bragg angle than for the 4f shell since they are highly non-localized.

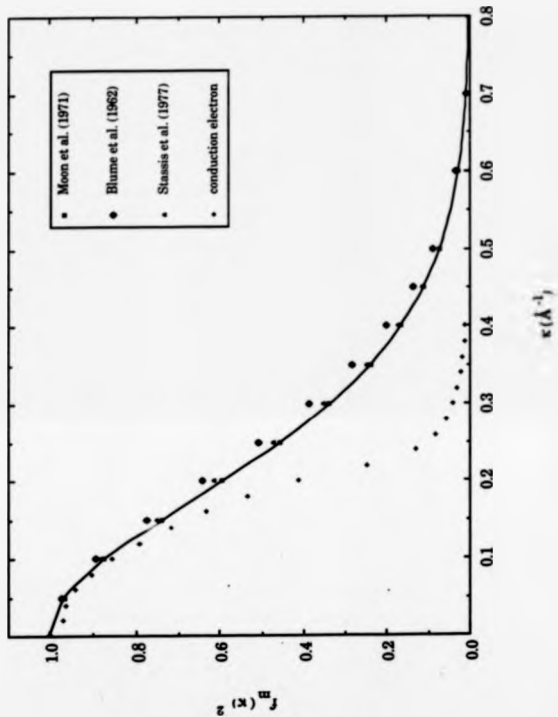
Evaluation of the RKKY interaction is possible only with extreme approximations. Consequently, only an estimate of the conduction electron form factor may be made. For a free electron gas in three dimensions we may write (Freeman 1972):-

$$f_{\text{cond}} = \frac{1}{2} \left( 1 + \frac{4k_F^2 - \kappa^2}{4k_F\kappa} \ln \frac{2k_F + \kappa}{2k_F - \kappa} \right) \quad (2.64)$$

where  $k_F$  is the radius of the conduction electron spherical Fermi surface. For Gd,  $k_F$  was calculated to be  $1.4 \times 10^{10} \text{ m}^{-1}$ , and the resulting form factor is also shown in figure 2.5.

For values of  $\sin\theta/\lambda < 0.22\text{\AA}^{-1}$  the conduction band magnetization is important and should be included in any structure factor analysis. In practice, however, this is very difficult as other factors e.g. temperature, type of magnetic order and diluent concentration will also influence the contribution.

Figure 2.5 Form Factor of Gadolinium



## 3

## Neutron Diffraction Experimental Techniques

## Introduction

The neutron diffraction studies of Gd-Y and Gd-Sc alloys were carried out at the High Flux Reactor at the Institut Laue-Langevin, Grenoble. The instrument used was the D9 diffractometer, which is situated on the hot source beam tube H3. The hot source (10 dm<sup>3</sup> graphite at 2400 K) modifies the Maxwellian distribution of the thermal neutron flux (in equilibrium with the D<sub>2</sub>O moderator at 300 K) such that there is an enhancement of the neutron flux in the wavelength range  $0.4 < \lambda < 0.8 \text{ \AA}$ . The use of 'hot' neutrons is a prerequisite for studies of materials containing natural Gd due to its high capture cross-section of thermal neutrons.

## 3.1 Neutron Diffractometer D9

D9 provides neutrons in a continuously variable wavelength range from a Cu crystal monochromator in transmission geometry using the (220) planes. No second order wavelength contamination was expected due to the absence of the 110 reflection for Cu, and at an operating wavelength of  $\sim 0.48 \text{ \AA}$ , very little higher order contamination could be expected due to these wavelengths lying well inside the Gd absorption edge. The  $\lambda/2$  contamination ( $\sim 1\%$ ) was effectively removed by using an In resonance filter ( $0.48 \text{ \AA}$ ). The nominal neutron wavelength selected by the monochromator take-off angle was

measured using a Be standard crystal. D9 is fully automatic in performing many types of scans, controlled earlier by a PDP 11/34 and now a Micro-VAX II. Automatic temperature control is available with the duplex closed-cycle He refrigerator (Allibon et al., 1981) which has an operating range 14–300 K.

D9 has a diffraction geometry of the standard normal-beam equatorial type, i.e. both incident and diffracted beams lie in the same horizontal plane, normal to the axis used for rotation of the crystal through the Bragg condition. Figure 3.1 shows a plan schematic of D9 with the path lengths and take-off angles of the diffracted beam marked. The pre- and post-sample slit sizes were determined by the sample size; they were generally chosen to be equal (typically 10mm in diameter), and such that for any measurement the sample would be completely bathed in the incident radiation, but not so large as to enhance the background radiation unnecessarily. The pre-detector slit was typically 8mm for centering the sample, but replaced by a larger (typically 14mm) slit for integrated intensity measurements, such that it did not impede the diffracted beam from the reflection of interest.

D9 is a four-circle diffractometer, the four 'circles' referring to the three crystal rotation axes,  $\omega$ ,  $\chi$ , and  $\phi$ , and the detector rotation axis,  $2\theta$ .  $\phi$  is the goniometer rotation axis, which may be moved out of the vertical by its location on the  $\chi$  circle (see figure 3.2).  $\omega$  is the angle of rotation of the  $\chi$  circle about a vertical axis. Being a four-circle machine, D9 has an extra degree of freedom (i.e. the crystal may be rotated about the scattering vector). However, this extra freedom is limited by the  $\chi$ -circle, which has restricted movement in order to prevent it from hitting the collimators. Consequently bisecting diffraction geometry (where  $\omega=\theta$ ) is generally adopted. Therefore, for best possible use of the instrumental resolution, the crystal orientation with respect to the  $\phi$ -axis should be chosen beforehand. In order to maximize the instrumental resolution along the  $c^*$  direction about h0l type reflections, the samples should

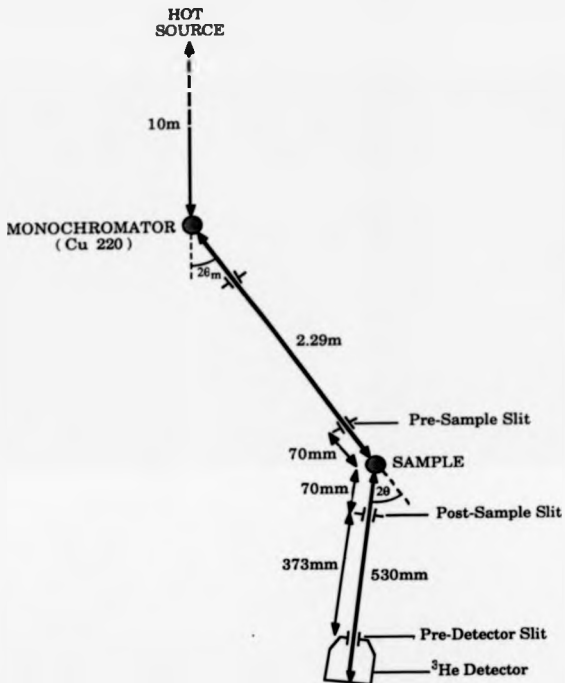


**Figure 3.1 Plan Schematic of D9 Diffractometer**



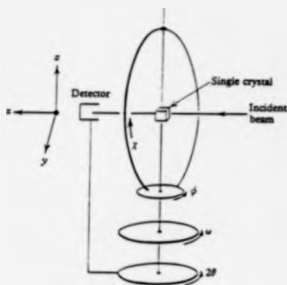


Figure 3.2 Diffraction angles in the standard normal-beam equatorial geometry. Note that for D $\theta$  the zero  $\chi$  angle is when the positive direction of the goniometer-head axis is along  $-z$ .

be mounted with their  $a^*c^*$  planes in the horizontal diffractometer plane when the  $\phi$  axis is perpendicular to the plane.

The samples were mounted on Al pins using Kwikfill and the Al pins mounted on the copper cold tip of the displax. The sample was aligned in the beam centre by using the novel XYZ translations at the base of the displax head (Archer and Lehmann, 1986) to bring the sample into central alignment with cross-hairs in an optical telescope. The sample was then sealed inside an inner V can containing an air atmosphere. Outside the V can is placed a thin Al heat shield and finally an outer Al vacuum shield. A schematic diagram of the cryostat assembly is presented in figure 3.3. The displax refrigerator was stable to  $\pm 0.1$  K, with an absolute accuracy of approximately  $\pm 1$  K.

### 3.2 Resolution Effects

For D9, the resolution in the vertical direction was expected to be poor due to lack of vertical collimation. In the horizontal plane of the instrument, the resolution is very much better, governed by essentially five factors; beam divergence, sample crystal mosaic, sample crystal size, detector resolution and neutron wavelength bandwidth,  $\Delta\lambda$ . The effect of these parameters on the 2-D reflection profile in the equatorial plane has been discussed in some detail by Schoenborn (1982). For a given sample, this may be readily determined by a 2-D scan around a selected nuclear reflection (figure 3.4). The most important feature concerning the type of investigation used for studying Gd-Y and Gd-Sc is that the reflection profile in the  $\omega/2\theta$  plane of D9 is, by and large, ellipsoidal with a high major/minor axial ratio and with the major axis inclined at a few degrees to the  $2\theta$  axis. For most purposes, it is therefore sufficient to note that the resolution is best in  $\omega$ , being determined essentially by the incident beam divergence and the sample crystal mosaic, and notably worse in  $2\theta$ , due to the combined effects of the detector resolution and wavelength spread  $\Delta\lambda$ .

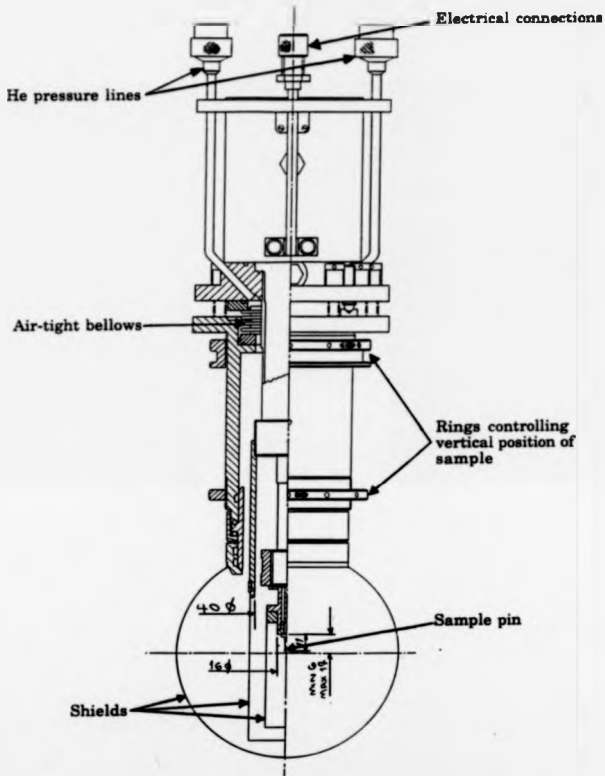


Figure 3.3 Section through and exterior aspects of the cryostat assembly.

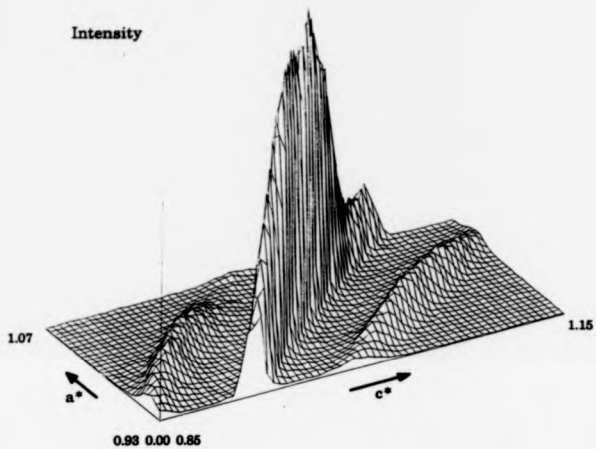


Figure 3.4 2D scan around 101 reflection for Gd<sub>60</sub>Y<sub>40</sub> at 40 K.

The resolution ellipsoid thus restricts the choice in how the crystal is mounted on the pin: first the scattering vector and the modulation wavevector,  $q$ , should lie in the equatorial plane since the vertical resolution is poor. Secondly, because the resolution is always worse in  $2\theta$  than  $\omega$ , the satellites are best resolved when the scattering vector and  $q$  are as near to perpendicular as possible, and worst when collinear. Therefore, for the best possible resolution along the helical  $q$ -vector, the sample must be positioned such that the scan involves scanning only  $\omega$  (figure 3.5.). In this figure, it is also shown how a scan along  $\omega^*$  through the 002 reflection will include the contribution to the integrated intensity of the satellites at  $hk\zeta$  (where  $\zeta = l \pm q$ ) due to the poor resolution in  $2\theta$ , provided the  $q$ -vector is not too large ( $\omega$  less than  $\sim 30^\circ$ ).

### 3.3 Experimental Procedure

Before the diffractometer can 'find' a given reflection, the orientation of the crystallographic axes with respect to the laboratory frame must be known. Setting up a UB matrix (which transforms the crystal axes into the laboratory axes) is therefore an important first procedure in the study of a newly mounted sample. It is calculated by finding two or three strong non-collinear reflections, and subsequently refined when the positions of additional reflections (in the region of reciprocal space of most interest) have been measured. The refinement is carried out by a least squares fitting routine on the instrument computer.

The diffracted magnetic and nuclear intensities were collected by either:

- 1)  $\omega/2\theta$  scans, where  $\omega$  and  $2\theta$  are moved in the ratio 1:2. These scans are effectively radial in reciprocal space.
- 2) Q-scans. These scans are along specific directions in reciprocal space and may employ all four circles.

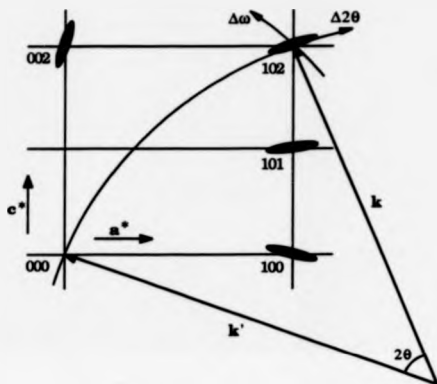


Figure 3.5 The resolution function and its importance in the  $(h0l)$  plane.

Note though that the combination of instrumental resolution and detector slit width means that in both types of scans the region swept out has finite width. In the paramagnetic phase (well above the initial ordering temperature),  $\omega/2\theta$  scans were performed through an extensive set of reflections to obtain integrated intensities for a nuclear structure refinement. Then, at each temperature, scans were made along the  $c^*$  and  $a^*$  directions through several low-angle nuclear reflections to check for ferromagnetic contributions. At selected temperatures, extended scans were also performed along various directions in reciprocal space to detect the appearance of antiferromagnetic satellite reflections.

After determining the temperature ranges of the magnetic phases for a particular alloy composition,  $\omega/2\theta$  scans were made through more extensive sets of reflections at a fixed temperature within each phase. Particular emphasis was placed on those reflections at low Bragg angles. In the antiferromagnetic phases the scans included the satellite reflections associated with each nuclear reflection. Lorentz corrections (McIntyre and Stansfield, 1988) and absorption corrections were applied to the observed integrated intensities of the nuclear and the satellite reflections to obtain partially complete sets of structure factors. The magnetic structure of each phase was refined against these sets of structure factors to check the proposed magnetic structures.

### 3.4 Nuclear Structure Refinement

The set of integrated intensities collected in the paramagnetic phase of each alloy (Gd-Sc only) and corrected for the Lorentz factor and absorption were used for a nuclear structure refinement. Structure refinements involve the adjustment of several chosen parameters in order to minimize the discrepancies between the observed and computed intensities. In order to

measure the correctness of the refinement, it has become common practice to use a residual of the following form

$$R = \frac{\sum | |F_o| - |F_c| |}{\sum |F_o|}$$

where  $F_o$  is the square root of the observed intensity and  $F_c$  is the square root of the calculated intensity. The value of  $R$  is a small fraction (typically less than 0.1) when the structure is correct, and a large fraction when incorrect. In the nuclear structure refinement of the Gd-Sc alloys, the adjusted parameters were a scale factor, an extinction parameter and the two thermal displacement parameters of the hcp structure. In particular, no free positional parameters were allowed. Some of the results from the structure refinements are presented in table 3.1.

### 3.5 Evaluation of the Average Spontaneous Magnetization

For a ferromagnetic reflection, the ratio of the magnetic to the nuclear integrated intensity (directly proportional to their respective cross-sections) may be derived directly from (2.35) and (2.38):-

$$\frac{I_M}{I_N} = \frac{(\gamma_0)^2 f_m(\kappa)^2 S^2 |q|^2}{b_{\text{alloy}}} \quad (3.1)$$

For antiferromagnetic reflections, the expression is similar except that  $f_m(\kappa)$  should be replaced by  $f_m(\kappa)t$  as appropriate for each satellite. (For long period structures,  $f_m(\kappa)t$  may be approximated by  $f_m(\kappa)$ .) The important information regarding the magnetic structures is contained in the spontaneous magnetization  $S$  (a function of the temperature), and  $q$  (dependent directly on the magnetic structure of the alloy). It is therefore useful to rearrange (3.1):-



Table 3.1 Results of nuclear structure refinements on Gd-Sr alloys

Alloy	Temp.	No. of refin.	R factor	hkl	$Y_s$	$e^{-2W}$
Gd <sub>46</sub> Sr <sub>54</sub>	170 K	57	0.0131	100 002 101	0.883 0.671 0.820	0.987 0.982 0.982
Gd <sub>49</sub> Sr <sub>51</sub>	220 K	39	0.0118	100 002 101	0.980 0.943 0.943	0.980 0.974 0.974
Gd <sub>70.6</sub> Sr <sub>29.4</sub>	200 K	58	0.0241	100 002 101	0.752 0.459 0.610	0.986 0.981 0.981
Gd <sub>72</sub> Sr <sub>28</sub>	200 K	49	0.0282	100 002 101	0.813 0.518 0.680	0.984 0.982 0.980
Gd <sub>75</sub> Sr <sub>25</sub>	220 K	59	0.0272	100 002 101	0.883 0.671 0.800	0.984 0.977 0.978
Gd <sub>78.1</sub> Sr <sub>21.9</sub>	220 K	55	0.0165	100 002 101	0.883 0.671 0.820	0.982 0.977 0.976

$$(Sq)^2 = \frac{I_M/I_N b_{\text{alloy}}^2}{(\gamma_{\text{Fe}})^2 \epsilon_m(\kappa)^2} \quad (3.2)$$

This quantity is readily calculable for a particular reflection, and the information on the magnetic structure is tied up in  $q$  which may only be evaluated after a magnetic structure has been proposed. Consequently, it is only when a magnetic structure has been suggested that  $S$  may be found – a different value of  $S$  will be obtained for a different magnetic structure owing to a different value of  $q$ . Determination of the magnetic structure is, however, more straightforward than a trial and error process, because the absence of magnetic reflections along reciprocal lattice axes usually gives some indication of the orientation of the moment vectors. The correct magnetic structure may be assumed to have been found when the spontaneous magnetization over a range of temperatures within a magnetic phase is in accord with a theoretical curve (or an experimental curve measured by other means).

In chapters 4 and 5, the results of magnetic diffracted intensities of the 100 and 002 reflections are presented in the form of (3.2). Magnetization curves are then derived on the basis of the proposed magnetic structure exhibited by the sample at each temperature.

### 3.6 Correction Factors

In general, the measured integrated intensity will not reflect the true scattering cross-section due to a number of factors. The important ones are

- 1) Lorentz factor
- 2) Absorption factor,  $A$
- 3) Debye-Waller factor,  $e^{-2W}$
- 4) Thermal Diffuse Scattering (TDS),  $\alpha$
- 5) Extinction,  $Y_e$

These factors modify the integrated intensity from a given Bragg reflection in the following way

$$I' = IAe^{-2W}(Y_s + \alpha), \quad (3.3)$$

where  $I'$  is the observed intensity corrected for the Lorentz factor, and  $I$  is the 'true' intensity used in (3.2). (There is in fact a choice in how to apply TDS and extinction corrections. For example one may use  $Y_s(1+\alpha)$  instead of  $(Y_s+\alpha)$  - Tibbals et al., 1981- however since the difference  $(1-Y_s)\alpha$  is usually small it is not too important, especially since  $Y_s$  very different to 1 occurs mainly at low  $Q$  whereas large  $\alpha$  values occurs at high  $Q$ . These factors will, in general, be different for nuclear and magnetic reflections and are discussed below with reference to their importance for the low-angle reflections used in this study.

1.) The Lorentz factor is simply a geometric term which corrects for the different rates at which the reciprocal lattice points sweep through the diffraction sphere. (The longer the reciprocal lattice points spend near to the Ewald diffraction sphere, the more intense the reflection.) The Lorentz factor was corrected for in the peak-fitting program from which the integrated intensities were derived.

2.) Since the calculation of  $(S_q)^2$  involves normalizing the magnetic intensities to the nuclear intensities (3.2), the absorption factor (dependent on the path length of each part of the diffracted beam in the sample) was not expected to affect the calculated values. For the antiferromagnetic reflections (whose path is in general slightly different to that for the nuclear reflections), a version of the ILL absorption program DATAP (Coppens et al., 1965) modified to accept fractional reciprocal lattice indices indicated the error in this assumption was less than 1% when averaged between the two satellites.

3. & 4.) These two factors are considered together since they both arise from the thermal motion of the scattering centres. The presence of the thermal motion means the elastic cross-section may be modified by inelastic scattering processes, where a neutron may lose or gain energy by interaction with a

phonon. The Debye-Waller factor takes the form  $e^{-2W}$  where  $W$  is proportional to  $(\sin\theta/\lambda)^2$ , and leads to a reduction in the observed peak intensity. The nuclear structure refinements showed that the introduction of an error of ~3% at maximum would arise from this factor for the 100, 101 and 002 reflections.

Thermal diffuse scattering (TDS) is the 'background' distribution around a reciprocal lattice point of the intensity lost from the Bragg reflection as a consequence of thermal vibrations. This diffuse scattering is not uniform through reciprocal space, but possesses a broad maximum centred on the reciprocal lattice points, and in severe cases may result in over-estimation of the integrated intensity by as much as 25%. TDS is evaluated by analysis of the active scattering volume swept out in reciprocal space by the detector aperture during the scan, and requires that the crystal elastic constants be known. An estimation of the TDS factor for  $\text{Gd}_{88}\text{Sc}_{12}$  gave a value for  $\alpha$  of much less than 1%.

5.) Because of the severe absorption associated with materials of high Gd concentration and hence small path lengths in the sample, the effect of extinction in these experiments was expected to be very small. The phenomenon of extinction is based on the fact that a neutron beam subjected to double reflection from the same set of planes coincides in direction with the primary radiation and interferes with the latter. This interaction leads to a considerable interference weakening of the primary beam, or in other words, to screening of the inner layers of the crystal. If this type of phenomenon occurs within the limits of a single mosaic block, it is called primary extinction; if radiation scattered by different mosaic blocks interacts, it is called secondary extinction (see for example Isyumov and Ozerov, 1970).

The Gd-Y alloys studied by Bates (1985) were indeed found to suffer from weak secondary extinction. However, in this study, three of the six samples used for neutron scattering were observed to suffer from severe extinction (see

table 3.1). This is surprising since the same crystal growth method was employed for at least five of the samples.

Extinction factors for the nuclear reflections were obtained from the nuclear structure refinements performed assuming secondary extinction described by a type I crystal (where extinction effects are dominated by the sample mosaic spread). For the antiferromagnetic reflections, the magnetic extinction was ignored since it was expected to be a small correction compared to the nuclear extinction correction. For the ferromagnetic reflections, the superposition of nuclear and magnetic diffracted intensity means that the total extinction may not be derived from the nuclear and magnetic extinction factors evaluated for their separate respective intensities, since the extinction is a complex function of the total intensity. Instead an iterative method was used to calculate  $Y_p/Y_{sm}$  ( $Y_{sm}$  is the magnetic extinction) employing Zachariasen's (1967) correction to the ferromagnetic reflections (see Appendix A). Although Zachariasen's treatment should only be used in the approximation of small extinction, the analysis proved to be satisfactory: systematic errors arising from the determination of extinction are difficult to estimate, particularly when the correction is important, but probably lie in the region of 5–10% of  $\delta$  where  $\delta = 1 - Y_g$ .

### 3.7 Errors in the Evaluation of $(Sq)^2$

For antiferromagnetic reflections, (3.2) may be expressed as

$$(Sq)^2 = \left( \frac{I_M}{I_N} \right) C,$$

with

$$C = \frac{b_{\text{alloy}}^2}{(\gamma r_0)^2 f_m(\kappa)^2} \frac{Y_g}{Y_{sm}}.$$

Errors in the constant  $C$  arise from computation and determination of the physical parameters. Being systematic errors they are difficult to evaluate and have thus been excluded in the presentation of the data, but are not expected to exceed the experimental errors. Errors in the evaluation of the quantity  $I_M/I_N$  arise from the counting statistics: the Gaussian error sigma for a measured integrated intensity  $I$  was typically 2%.

For ferromagnetic reflections,

$$(\text{Sq})^2 = \left( \frac{I_T' - I_N'}{I_N'} \right) C,$$

where  $I_T'$  is the total peak integrated intensity. Hence,

$$(\sigma(\text{Sq})^2)^2 = \left( \frac{\partial(\text{Sq})^2}{\partial I_T'} \right)^2 (\sigma(I_T'))^2 + \left( \frac{\partial(\text{Sq})^2}{\partial I_N'} \right)^2 (\sigma(I_N'))^2$$

$$(\sigma(\text{Sq})^2)^2 = \left( \frac{1}{I_N'} \right)^2 (\sigma(I_T'))^2 + \left( \frac{I_T'}{I_N'^2} \right)^2 (\sigma(I_N'))^2$$

$$\sigma(\text{Sq})^2 = \sqrt{(2)(0.02)} \left( \frac{I_T'}{I_N'} \right) C.$$

In a similar fashion, for the antiferromagnetic reflections one obtains

$$\sigma(\text{Sq})^2 = \sqrt{(2)(0.02)} \left( \frac{I_M}{I_N} \right) C.$$

These are the errors which have been used in the presentation of the data, reflecting the experimental point to point accuracy.

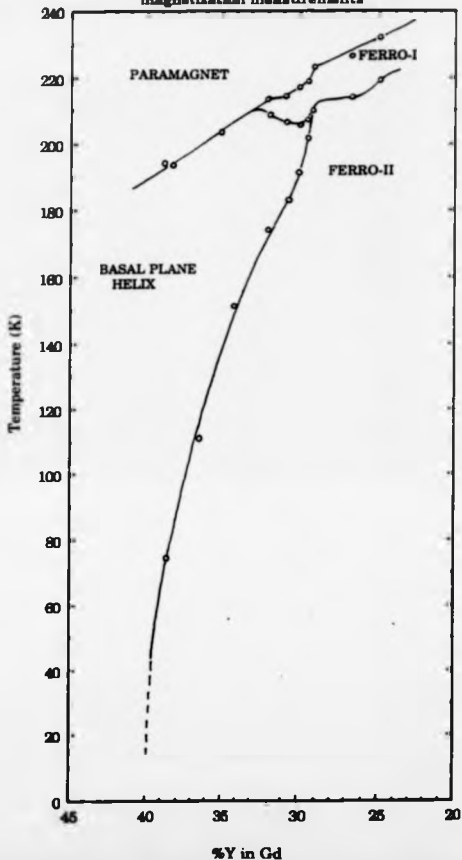
## Experimental Results: Gd-Y

### Introduction

The Gd-Y alloys were the first alloys studied in this work. The magnetic phase diagram and magnetic behaviour of Gd-Y alloys have already been well documented by Bates (1985). A partial magnetic phase diagram is reproduced in figure 4.1 for reference. Previous experiments performed on single crystal Gd-Y alloys revealed a range of unique and interesting magnetic behaviour. One of the most interesting features of this alloy series is the presence of an apparently continuous (2nd order) phase line separating two ordered magnetic phases. This phase line exists between the compositions of about  $\text{Gd}_{60}\text{Y}_{40}$  and  $\text{Gd}_{70}\text{Y}_{30}$ , separating a high temperature basal plane helix from a low temperature canted ferromagnetic phase, ferro-II. On approaching the phase line from the helimagnetic phase either by increasing Gd concentration or by lowering the temperature, the helical inter-layer turn angle appears to decrease smoothly towards zero, values as small as  $1.4^\circ$  having been measured (Bates et al., 1985). This suggests that a continuous change of the order parameter may take place on crossing between the helimagnetic and ferro-II phases. Such behaviour, unique among rare-earths, is attributable to the relatively small planar anisotropy of Gd and can be modelled assuming continuous basal plane symmetry (Michelson, 1977).

One of the consistent features of this phase transition is a large increase in the helimagnetic diffraction peak widths prior to the formation of

Figure 4.1 Partial magnetic phase diagram of Gd-Y alloys from ultrasonic, resistivity and magnetization measurements





ferromagnetic order, the effect being more pronounced in the alloys richer in Y where the transition temperature is lower. It has been proposed that this apparent loss of long-range helimagnetic order arises from the formation of random fields due to the proximity of the ferromagnetic phase. It is then possible that if the ferromagnetic transition occurred at low enough temperatures then the helimagnetic order would be completely destroyed, yielding a metastable spin-glass like phase.

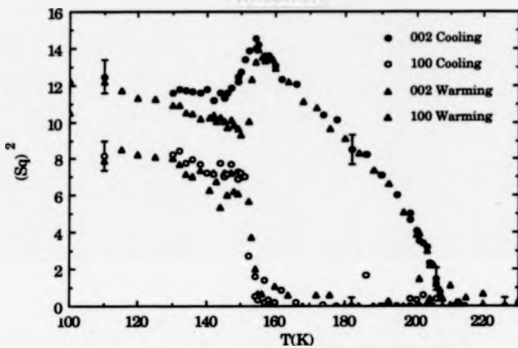
In order to understand better the nature of the helix/ferro-II transition in Gd-Y alloys, we studied two alloys with nominal compositions of  $\text{Gd}_{88}\text{Y}_{12}$  and  $\text{Gd}_{60}\text{Y}_{40}$ . In the former sample the transition takes place at high temperature ( $\sim 151$  K) and in the latter the transition is at very low temperature.

#### 4.1 $\text{Gd}_{88}\text{Y}_{12}$

##### 4.1.1 General Properties

The experiment was performed at a wavelength of  $0.48\text{\AA}$  (a compromise between high absorption at high  $\lambda$  and low flux at low  $\lambda$ ) and the sample was mounted with the usual orientation for maximum resolution along  $c^*$ , as previously described in section 3.1. We unfortunately cooled the sample just into the helical phase before we began Q-scans in the search for magnetic satellite reflections, so the Néel temperature was only accurately determined on warming and observed to be 208 K. Scans of the  $\omega/2\theta$  type were made while cooling from 210 K down to 20 K through various low  $2\theta$  reflections in order to enable averaging over domains in the ferromagnetic phase, and to improve statistics in general. The average values of  $(S_q)_{100}^z$  and  $(S_q)_{001}^z$  are plotted against temperature in figure 4.2. The interpretation of the data has been dealt with in the previous chapter, however it is important enough to re-iterate that

Figure 4.2  $(S_q)^2$  vs. Temperature  
for Gd66Y34



the 002 reflection contains contributions from the satellites owing to the poor inherent resolution along  $c^*$ , whereas the 100 does not contain any such contribution. In the high temperature phase, it is clear from the presence of satellites at  $hk\zeta$  (where  $\zeta = l/q$  and  $q$  is a displacement in reciprocal lattice units along  $c^*$ ) and the absence of any magnetic contribution to the 100 type reflections that the structure is a simple basal plane helix. Figure 4.3 is an isometric plot built up from  $c^*$  scans through the 101 reflection. As the temperature drops through the helical phase, the  $q$ -vector of the helix decreases uniformly and approaches zero at the helix/ferro-II transition at  $\sim 151$  K. Below 151 K, the satellites have become absorbed in the tail of the nuclear peak; the alloy has a canted ferromagnetic structure whose canting angle varies with temperature as shown in figure 4.4. At this transition to ferromagnetism, the moments rapidly acquire a canting angle of about  $65^\circ$  which then remains approximately constant down to the lowest temperatures reached.

The ionic magnetization per Gd ion is presented in figure 4.5 as calculated from the 100 and 002 reflections (eqns. 2.11 and 2.12) and also as calculated from the 101 satellites in the helical phase (eqns. 2.9 and 2.10). The measured saturation magnetization can be expected to have a value between  $7\mu_B$  and  $7.6\mu_B$ , with the excess moment above  $7\mu_B$  arising from conduction electron polarization effects. (The full magnetization of  $7.6\mu_B$  will not be measured due to the rapid decrease of the conduction electron form factor with increasing scattering vector.) A theoretical curve is also given in figure 4.5; this is the mean field theoretical curve taken from the Debye-Weiss quantum theory with  $J=7/2$ . This curve, and all subsequent theoretical magnetization curves presented in this chapter and the next, have simply been scaled in temperature to  $T_0$  (where  $T_0$  is the initial ordering temperature), and in  $S_{Gd}$  to the approximate value of the saturation magnetization (from 100 and 002 reflections) such that a reasonable fit over the whole curve is achieved.

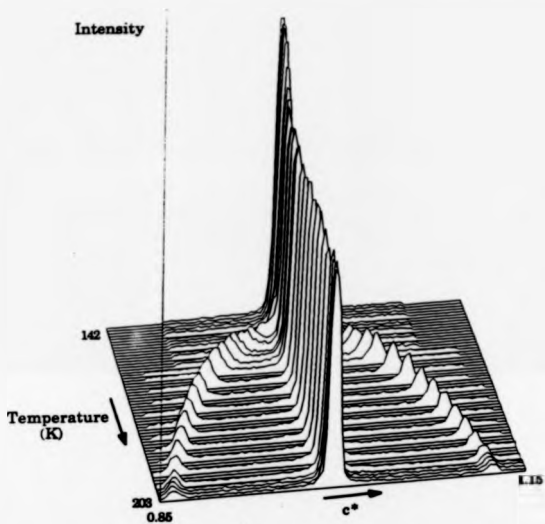


Figure 4.3 Isometric plot for Gd68Y34 constructed from  $c^*$  scans between 203 K and 142 K while cooling.

Figure 4.4 Canting Angle vs. Temperature  
for Gd66Y34

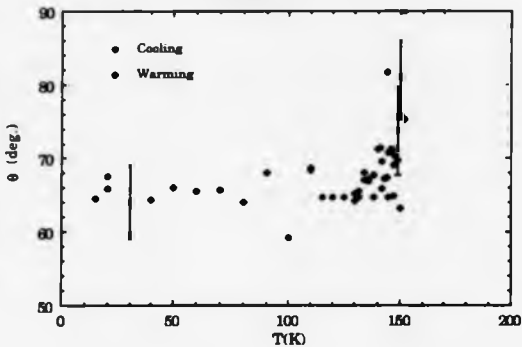
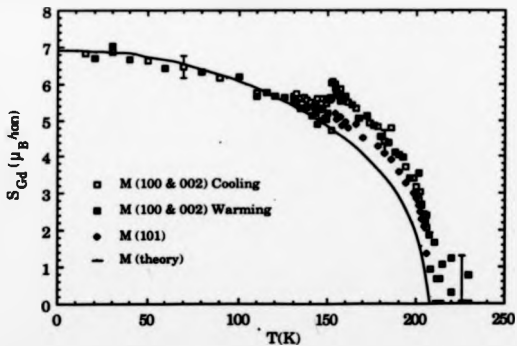


Figure 4.5 Mean Ionic Gd Moment vs. T  
for Gd66Y34

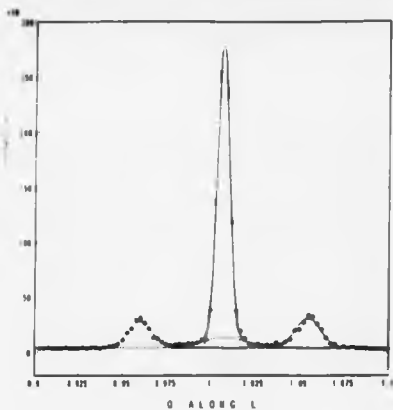


High values of magnetization, particularly from the 100 and 002 reflections, are immediately apparent in the helical phase but most probably arise due to extinction, which has not been corrected for: since the magnetization has been calculated by normalizing the magnetic intensity to the nuclear intensity, which suffers more from extinction than the magnetic intensity, this will lead to an over-estimation of the magnetization, in keeping with the observations. Furthermore, in the basal plane helix structure the magnetization calculated from the 101 reflection can be expected to suffer less from this effect due to the usually lower extinction of the 101 than the 002 reflection, also consistent with the results. In the ferromagnetic phase, magnetization calculated from the 100 and 002 reflections follows the theoretical curve well and saturates at approximately  $6.9\mu_B$ . In this phase, the extinction can be expected to have the opposite effect, leading to an under-estimation of the magnetization (see Appendix A). However, by comparing the observed saturation magnetization with an expected value in the region of  $7.3\mu_B$ , the effect is not severe.

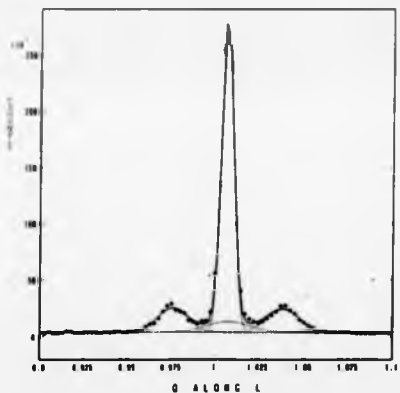
#### 4.1.3 The Helix / Ferro-II Transition in $Gd_{95}Y_{54}$

There has been much debate concerning the Gd-Y alloys as to whether the  $q$ -vector goes continuously to zero at the ferromagnetic transition or whether there is in fact a small jump to zero. Although it appears from figure 4.3 that the transition has a continuous nature, it still remains very difficult to extract small values of  $q$  due to the limitation of the instrumental resolution. The smoothly varying  $q$  may be attributed to the very low basal plane anisotropy of Gd.

Figures 4.6 and 4.7 show a series of  $Q$ -scans along  $c^*$  through the 101 reflection as the helix/ferro-II transition is approached. One can see that 3 K above the transition the satellites begin to disappear under the strong nuclear

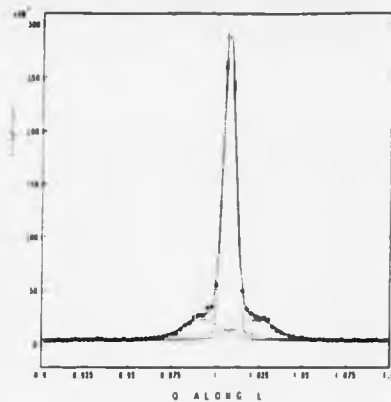


$T = 157 \text{ K}$

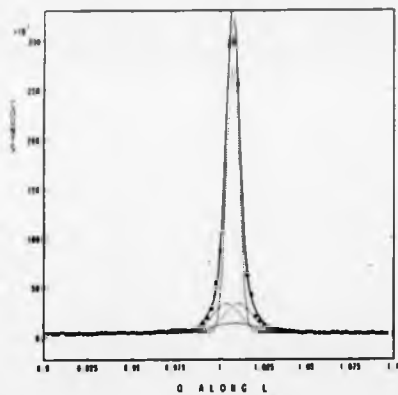


$T = 154 \text{ K}$

Figure 4.6 Q-scans along  $c^*$  through 101 reflection at 157 K and 154 K for  $\text{Gd}_2\text{FeY}_3$ .



$T = 152\text{ K}$



$T = 150\text{ K}$

Figure 4.7 Q-scans along  $c^*$  through 101 reflection at 152 K and 150 K for  $\text{Gd}_{66}\text{Y}_{34}$ .



reflection and this poses serious problems for the peak-fitting software. At this stage, the fitting of the satellites may go wildly awry, the most common problem being that the program tries to fit a single peak centred on the nuclear reflection to account for both satellites; the remaining peak to be fitted then suffers from very incorrect parameters.

In order to overcome this problem, we resorted to constraining many fitting parameters so that the program would be forced to recognise two satellites. The availability of an upgraded peak-fitting program at the ILL which ran considerably faster than the older version facilitated the implementation of the technique. The fitting was carried out as follows. Firstly, the nuclear profile was fitted with two Gaussian peaks just above  $T_N$ . This was simply an empirical device to describe the convolution of the less than perfect crystal mosaic spread with the not exactly Gaussian instrumental resolution function. The heights and widths of these peaks were then fixed and so too the distance between their centres. This was done because the nuclear part of the scan was not expected to vary much between 208 K and 151 K, except possibly the centre of this two-peak profile which was left unconstrained. The satellites, at high temperature in the helical phase, were fitted with Gaussians with the single constraint that their centres be equidistant from the centre of the main nuclear peak. These constraints alone work well until close to the ferromagnetic phase. Here, the satellite widths were constrained to be equal and eventually the heights, which is a valid approximation since the satellites are so close together. The beauty of the method is that the magnetic intensity appearing on top of the nuclear intensity due to the closeness of the satellites, forces the program to fit the 'satellites' under the main nuclear peak;  $q$ -vectors corresponding to a satellite separation less than the nuclear widths (limited by the resolution of the instrument) have been measured by these means. The fitting from several scans near the transition is also shown in figures 4.6 and 4.7; the turn angle,  $\phi = \pi q$ , calculated from these fits is shown in figure 4.8. The

overall fits are very good and this is reflected in the well behaved turn angle, which falls to values much less than  $1^\circ$  per layer.

It may be argued that it is meaningless to talk of a 'turn angle' when the satellites are so close together as to be indistinguishable from a single broad ferromagnetic peak. However, in a continuous transition of this type, there is not so much a transition from helimagnetism to ferromagnetism, but rather a transition via short-range helical order with low  $q$  and short-range ferromagnetic order. Therefore any boundary defined between the two has to be somewhat arbitrary. An indication of such a boundary might, for example, be the point at which maximum short-range order is reached. A plot of the fitted satellite widths against temperature is given in figure 4.9. The maximum in the widths corresponds well to  $T_c$  determined by extrapolation of the turn angle to zero, and below this temperature the ferromagnetic regions are dominant and becoming long-ranged. More importantly, since the fitted 'turn angle' varies smoothly (indicating a good peak fit even at a temperature where short range ferromagnetism is dominant) to values less than  $1^\circ$ , this is a very good indication that the transition is continuous.

There is some small thermal hysteresis, of 2 K at most, associated with the changeover from the modulated structure to the ferromagnetic structure, as observed previously by Legvold et al. (1980) and Blackie (1981). Thermodynamically, this is unusual when contrasted with the smooth decrease of the  $q$ -vector to zero at the transition, which is characteristic of a second order process. However, the thermal hysteresis almost certainly arises from the nucleation of different helical domain structures between warming and cooling. This has been observed in Tb and MnP (Baruchel et al., 1981, 1987, Drillat, 1982). From the discussion of helical and ferromagnetic domain structures by Palmer (1975), there is a strong case for arguing that on cooling, the ferromagnetic domains grow directly from the low  $q$  helical domains; on warming, however, the helical domains grow from the ferromagnetic domain

Figure 4.8 Turn Angle vs. Temperature  
for Gd<sub>66</sub>Y<sub>34</sub>

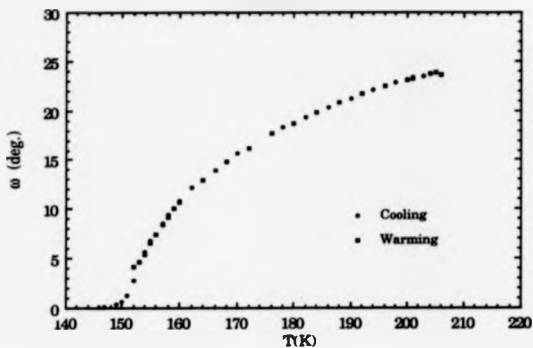
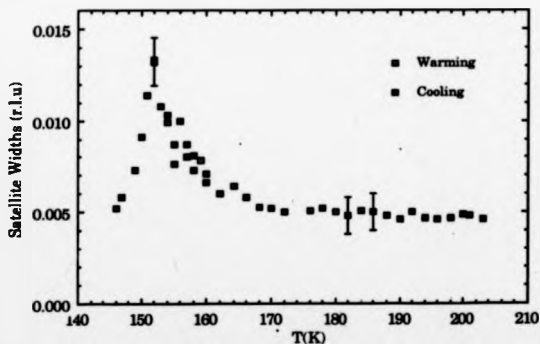


Figure 4.9 Satellite Widths vs. T  
for Gd<sub>66</sub>Y<sub>34</sub>



walls. This would explain the appearance of satellites at small  $q$  in the helical phase on warming (fig. 4.10), rather than emerging from beneath the nuclear peak in the reverse manner to the behaviour on cooling (fig. 4.3). By using the minimum inter-layer turn angle of  $4^\circ$  observed on entering the helical phase from the ferromagnetic phase, and assuming this turn angle is associated with the domain walls (in the ferromagnetic phase) from which the chirality domains evolve, it is possible to estimate that there are 45 spins in a  $180^\circ$  wall.

## 4.2 Gd<sub>80</sub>Y<sub>20</sub>

### 4.2.1 General Properties

The first experiment on Gd<sub>80</sub>Y<sub>20</sub> was also carried out at a wavelength of  $0.48\text{\AA}$ . The alloy was found to order initially into a simple basal plane helix at 188 K. The relative integrated intensities of the satellites for reflections with different angular positions from the hexagonal uniaxial confirmed the simple basal plane helix structure. From the isometric plot of  $c^*$  scans through the 101 reflection (figure 4.11), the most striking feature is seen to be the severe broadening of the magnetic satellites. The broadening is in fact so severe on approaching the ferromagnetic phase that by 12 K (the lowest temperature reached) the helimagnetic satellites are only just visible above background. Peak-fitting these broadened satellites, involving a deconvolution of an estimated resolution function, initially indicated that the best fit was a Lorentzian squared profile, consistent with the idea that the long-range helimagnetic order is being destroyed by interaction with random fields (Cowley et al., 1984). The helical system in Gd-Y can be expected to be particularly sensitive to random fields, with its 'continuous' symmetry easily disturbed by weak fields in the basal plane. Such behaviour, however, has not been observed in recent neutron diffraction experiments on very dilute Gd-Y

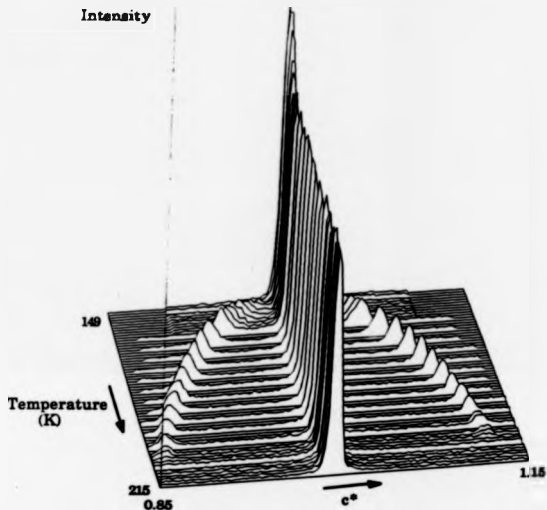


Figure 4.10 Isometric plot for  $\text{Gd}_{66}\text{Y}_{34}$  constructed from  $c^*$  scans between 215 K and 149 K while warming.



Figure 4.11 Isometric plot for Gd<sub>60</sub>Y<sub>40</sub> constructed from  $c^*$  scans through the 101 reflection between 204 K and 12 K.

alloys (Gotaas et al., 1985) nor in single crystal Gd-Y superlattices (Majkrak et al., 1986). It therefore appeared that the presence of random fields in the helimagnetic phase of Gd-Y was an inherent property of the alloys only arising in the proximity of the low temperature ferromagnetic phase. Also, if the ferromagnetic transition was at low enough temperatures, then the long-range helimagnetic order would be completely destroyed leading to a metastable spin-glass like state prior to the ferromagnetic transition.

#### 4.2.2 The Low Temperature Transition in $Gd_{90}Y_{10}$

A second experiment was performed (at  $0.47\text{\AA}$ ) in order to improve the counting statistics for a more thorough peak fitting analysis and to observe the effect of the helimagnetic break up in the basal plane as well as along the  $c$ -axis. In order to ascertain the nature of the loss of helimagnetic order, it is necessary to measure the peak shape of the coherent magnetic scattering. If, for example, the helimagnetic break up is due to random fields then the expected peak shape, after deconvolution of the instrumental resolution function, is Lorentzian squared (Cowley et al. 1984). However, on measuring the instrumental resolution function, it was found that the only scan direction with sufficient resolution to possibly observe such effects was along the omega arc, the sample rotation arc. Furthermore, the presence of significant spectral dispersion in the area of reciprocal space of interest imposed additional restrictions on the type of scans which could be performed in order to observe peak broadening. By mounting the sample with either the  $a^*-c^*$  or  $b^*-c^*$  planes within the instrumental horizontal plane, it was possible to perform scans with sufficient resolution parallel to  $c^*$  axis through selected magnetic diffraction peaks; it was not possible, however, to perform scans with sufficient resolution parallel to  $a^*$  or  $b^*$  through the satellites for any orientation of the crystal. The  $c^*$ -axis behaviour of the helimagnetic structure was then studied

down to the lowest possible temperature attainable using a duplex refrigerator (approximately 12 K). Again, no completed ferromagnetic transition was observed.

A similar approach to that used for  $\text{Gd}_{55}\text{Y}_{34}$  was employed in peak fitting the profiles. However, it soon became evident that the satellites did not have the Lorentzian squared profile that had been expected, but that instead a simple Gaussian peak shape for the satellites together with a broad peak centred on the nuclear reflection gave a remarkably good fit, as can be seen from figure 4.12. This is a typical fit taken from a scan at 20 K through the 101 reflection. The nuclear part is fitted with two peaks, both taken from a higher temperature scan where the broadening is not so apparent. The central diffuse peak is undoubtedly magnetic in origin and can be expected to arise from short-range order ferromagnetism.

The temperature dependence of  $(S_q)^2$  for the 101 and 101<sup>2</sup> reflections are plotted in figure 4.13. Values of  $(S_q)^2$  above 50 K for the 101 integrated intensity are absent in figure 4.13 due to the software fitting a curved background for the ferromagnetic peak at these temperatures. The temperature dependence of the Gd ionic magnetization as calculated from the 101 reflection and its satellites is given in figure 4.14. It has been assumed in the calculation that all the ferromagnetism appearing on the 101 reciprocal lattice point arises from c-axis ferromagnetism. Although it is known that Gd-Y orders into a canted ferromagnet from the helical phase, this assumption is not far wrong since it gives a good value for the saturation magnetization at  $\sim 7\mu_B$ . Furthermore, the jump in the magnetization at  $\sim 50$  K in figure 4.14 is not a physical property of the system, but results from the lack of data for the ferromagnetic peak integrated intensity above 50 K as a result of the reasons given above.

The decrease in intensity of the satellites and the increase in ferromagnetic peak intensity at low temperature (fig. 4.13) is consistent with the approach to the helix/ferro-II transition. Below about 60 K, the helix is



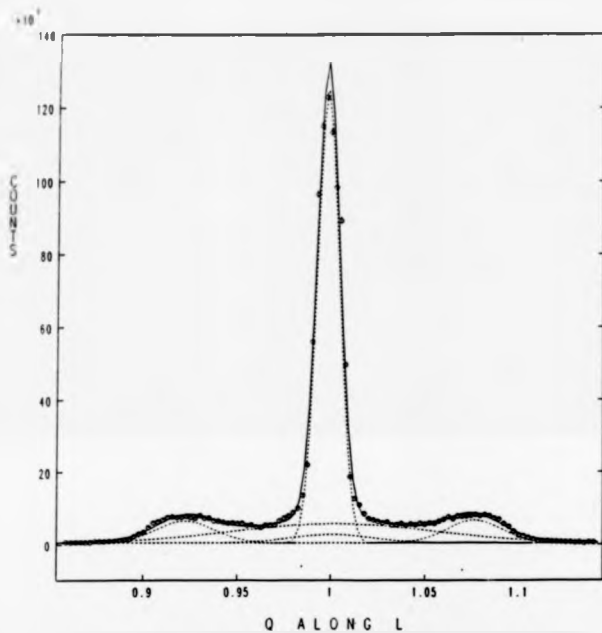


Figure 4.12 Scattering profile along  $c^*$  through 101 reflection at 20 K for Gd60Y40.

Figure 4.13  $(S_q)^2$  vs. Temperature  
for Gd<sub>60</sub>Y<sub>40</sub>

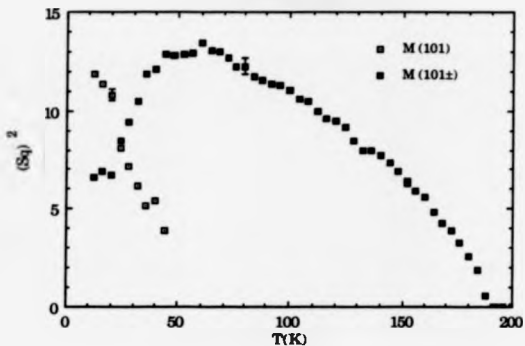
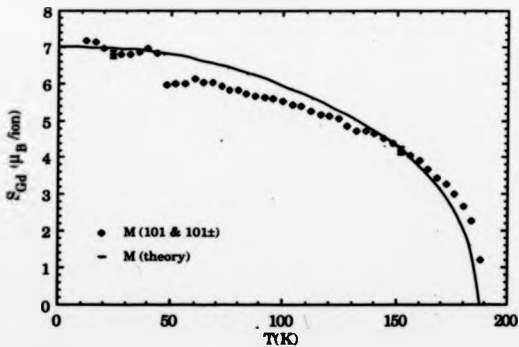


Figure 4.14 Mean Ionic Gd Moment vs. T  
for Gd<sub>60</sub>Y<sub>40</sub>



breaking up and forming small regions of ferromagnetism, the transition being very gradual to the point where it remains incomplete even at 12 K with no long-range ordered structure apparent. This type of behaviour must be influenced by the proximity of the helix/ferro-II phase line which will be very steep in this region of the phase diagram, and meet the 0 K line at a very slightly higher Gd concentration.

Such observations may be explained in terms of the fact that below  $\sim 60$  K, further cooling will take the alloy on a path very close to, and nearly parallel to, the helix/ferro-II phase line (see figure 4.1). In this region, local regions of the sample (on a microscopic scale) slightly richer in Gd will tend to exhibit ferromagnetic properties since they are nearer to the ferromagnetic phase, and regions richer in Y will tend to remain helimagnetic. The closeness of the phase line below 60 K accounts for the critical behaviour over such a wide temperature range, and this may be enhanced by the criticality characteristics of the phase line; in Gd-Y alloys the satellites have nearly always been observed to broaden near to the helix/ferro-II boundary indicating a wide region about the line where critical effects may be important.

The variation of the satellite and nuclear widths with temperature are shown in figure 4.15. The widths of the satellites are always greater than the resolution-limited (i.e. limited in minimum width by the instrumental resolution) nuclear Bragg peak, indicating that long-range order is never created in the modulated phase, possibly restricted by the formation of microdomains by random fields. The width of the nuclear Bragg peak is about 0.006 reciprocal lattice units, thus any structure that is correlated over 200 planes or more will appear as a resolution-limited Bragg peak. However, the width of the 101 satellites is about 0.008 r.l.u. (before increasing as the temperature is lowered), corresponding to an approximate maximum correlation length of about 125 atomic planes ( $\sim 700\text{\AA}$ ). As the phase transition is approached, the modulation becomes less spatially correlated, with a range of about  $300\text{\AA}$ . The

temperature dependence of the width of the ferromagnetic peak is shown in figure 4.18. Once more, values above 50 K are absent due to the program trying to fit the background. The width of this peak reaches a minimum of 0.07 r.l.u corresponding to a maximum correlation length of  $\sim 80\text{\AA}$ , i.e. the ferromagnetism remains very short-range.

A plot of  $\omega$  vs.  $T$  is given in figure 4.17, where once more a smooth variation of the turn angle may be observed. The turn angle is observed to 'lock-in' to  $13.8^\circ \pm 0.1^\circ$ , which encompasses the commensurate turn angle of  $13.85^\circ$  where the helix turns through  $360^\circ$  in 26 planes. Lock-in behaviour has up to now only been observed in very dilute alloys (Gotaas et al., 1985). It is debatable, however, whether the moments here or in the dilute alloys are truly locked-in, since the effect may not be due to crystal field effects, but due to a simple independence of the turn angle with temperature (see Gd-Sc alloys, chapter 5). For Gd<sub>80</sub>Y<sub>20</sub>, the 'lock-in' effect may again be explained by the steepness and closeness of the helix/ferro-II phase boundary. This is because if the helix/ferro-II phase boundary is a line where  $q \rightarrow 0$ , then a path parallel to it will have little influence on the turn angle.

Finally, it should be mentioned that although an interpretation of the results has been given in terms of the nature of the helix/ferro-II phase boundary, it seems likely that random fields still have a rôle in bringing about the observed effects. The supporting evidence is the large magnetic peak broadening, which has been predicted to occur in isotropic systems (being particularly susceptible to random field effects) where random fields will cause a long-range ordered structure to break up into micro-domains which will eventually destroy the long-range order (Cowley et al., 1984). However, the absence of the Lorentzian squared lineshape characteristic of random field effects is evidence that they do not tell the full story.

Figure 4.15 101 Nuclear and Satellite Widths vs. T for Gd60Y40

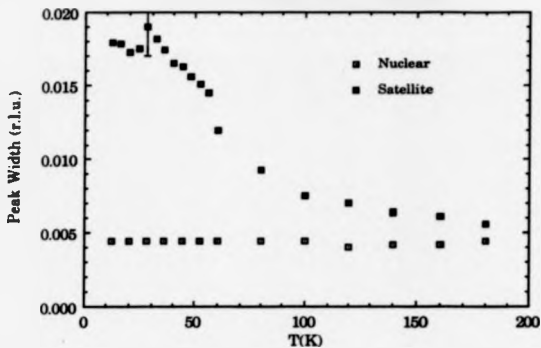


Figure 4.16 101 Ferromagnetic Peak Width vs. T for Gd60Y40

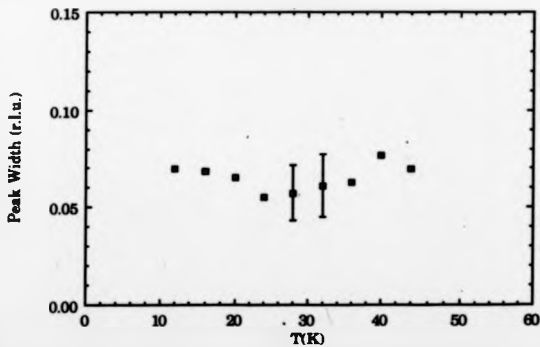
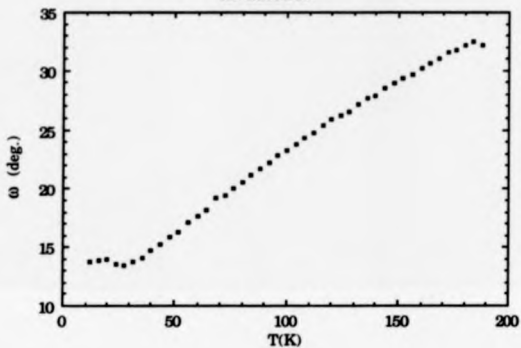


Figure 4.17 Turn Angle vs. Temperature  
for Gd60Y40



## 5

## Experimental Results: Gd-Sc

**Introduction**

The results of neutron diffraction experiments performed at a wavelength of 0.48Å on single crystal Gd-Sc alloys are presented here. A detailed discussion of the results is given in chapter 8, in the light of other supportive experimental techniques (chapters 6 and 7).

**8.1 Gd<sub>64</sub>Sc<sub>36</sub>**

It was decided to start the study of the Gd-Sc alloy series with Gd<sub>64</sub>Sc<sub>36</sub> since it was clear from the available information (Løgvold, 1980) that it exhibited only one magnetic phase (a helical antiferromagnetic phase) below the ordering temperature. The Gd<sub>64</sub>Sc<sub>36</sub> results will be presented first since in this respect, Gd<sub>64</sub>Sc<sub>36</sub> represents one part of the magnetic phase diagram common to both the Gd-Sc and Gd-Y alloys, and its interpretation is straightforward. The sample was mounted with the usual orientation for maximum resolution along  $c^*$ .

For this composition, antiferromagnetic satellite reflections were observed at all temperatures below 140 K. In the diffraction pattern, each nuclear reflection  $hkl$  is accompanied by a single pair of satellites at  $hk\zeta$  where  $\zeta = l/q$  and  $q$  is a displacement in reciprocal lattice units along  $c^*$ . The intensity variation of satellites centred about different reciprocal lattice points indicated

that they arise from a simple helix which propagates along the hexagonal  $c$ -axis, and with turn angle,  $\omega = \pi q$  between moments in adjacent layers.

Figure 5.1 shows the temperature dependence of  $(Sq)^2$  for the 100 and 002 reflections. The absence of any increase in  $(Sq)_{100}^2$  coincident with the appearance of the satellites means there is no associated ferromagnetism and the structure is most likely a simple basal plane helix. The 002 reflection includes contributions from the satellites (see Chapter 3), and therefore  $(Sq)_{002}^2$  is effectively the square of the spontaneous magnetization per ion. The temperature dependence of  $S_{Qd}$ , as calculated from the 100 and 002 reflections (eqns. 2.11 and 2.12), is given in figure 5.2.  $S_{Qd}$  calculated from the 101 reflection and its satellites (eqns. 2.9 and 2.10) is also presented. The resulting magnetization curves are in good agreement, although the saturation magnetization is a little high. (As with the Gd-Y alloys,  $S_{Qd}$  can be expected to have a value between  $7\mu_B$  and  $7.8\mu_B$ .) A theoretical mean-field magnetization curve is also given in figure 5.2, scaled in  $S_{Qd}$  to the observed saturation magnetization as obtained from the 100 and 002 reflections. Comparison shows the measured magnetization is generally high by about  $0.4\mu_B$  over the full curve and even higher near to  $T_N$ .

As the temperature is lowered the turn angle,  $\omega$ , is observed to decrease smoothly from an onset angle of  $33.6^\circ$  per layer (figure 5.3). At 30 K, the gradient  $d\omega/dT$  rapidly falls until the turn angle remains temperature-independent at a value  $\omega = 26.1 \pm 0.1^\circ$  down to the lowest temperature of 12 K. The 'locked-in' value of  $\omega$  is incommensurate with the lattice, the nearest commensurate turn angle being  $25.7^\circ$  where the spiral turns through  $2\pi$  in 14 planes.

Figure 5.4 shows an isometric plot of the scattered intensity observed in Q-scans through the 101 reflection along the  $c^*$  axis as a function of temperature. The behaviour of the turn angle is clear from this type of plot. Also evident is the progressive intensification of the satellites below  $T_N$ ,



Figure 5.1  $(Sq)^2$  vs. Temperature  
for Gd<sub>64</sub>Sc<sub>36</sub>

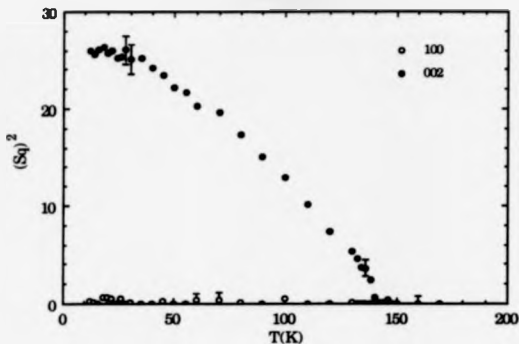


Figure 5.2 Mean Ionic Gd Moment vs. T  
for Gd<sub>64</sub>Sc<sub>36</sub>

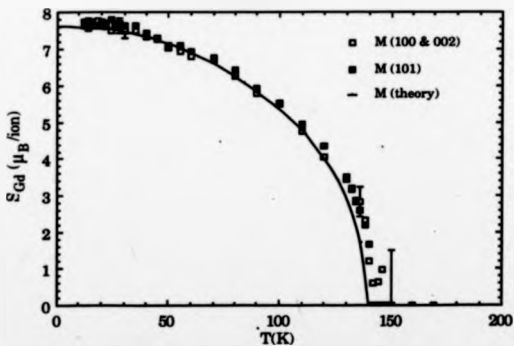
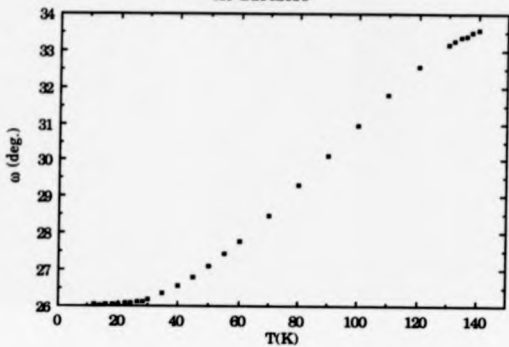


Figure 5.3 Turn Angle vs. Temperature  
for Gd64Sc36



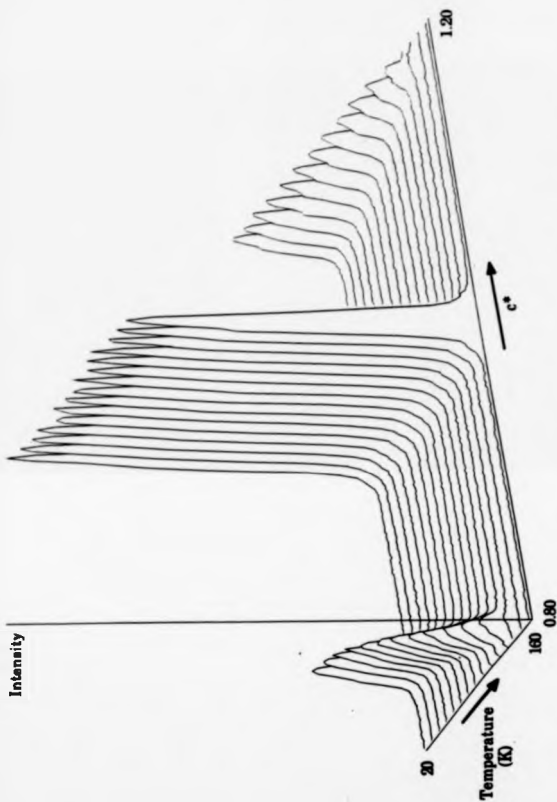


Figure 5.4 Isometric plot for Gd<sub>84</sub>Sc<sub>36</sub> constructed from  $c^*$  scans through the 101 reflection between 20 K and 160 K

consistent with the increase of the spontaneous magnetic moment in the basal plane helix structure. The absence of any magnetic intensity superimposed on the central Bragg peak confirms the absence of ferromagnetism. It is also apparent that the satellite widths remain approximately constant at a value close to that of the nuclear peak. In fact they remain resolution-limited with a width of 0.01 reciprocal lattice units over the full magnetically ordered temperature range, which means that the magnetic structure is long-range ordered with a correlation length of about 100 planes.

The simple basal plane helical structure was verified by refinement against sets of reflections at temperatures both above (50 K) and below (20 K) the 'lock-in transition'.

### 5.3 Gd<sub>69</sub>Sc<sub>31</sub>

Below the initial ordering temperature at 154 K, antiferromagnetic satellites were observed at  $hk\zeta'$  corresponding to an onset turn angle of  $-30^\circ$ , and existed down to 15 K. The temperature dependence of  $(Sq)_{100}^2$  and  $(Sq)_{002}^2$  is shown in figure 5.5. Again the 002 reflection contains contributions from the satellites, whereas the 100 does not. The high temperature phase has a basal plane helical structure similar to Gd<sub>64</sub>Sc<sub>36</sub>. In contrast to Gd<sub>64</sub>Sc<sub>36</sub>, however, a low temperature phase exists below 56 K as evidenced by the increase in  $(Sq)_{100}^2$ . This indicates the onset of a c-axis ferromagnetic moment which is seen to increase at the expense of the basal plane moment. The low temperature phase thus comprises a magnetic structure which embraces both c-axis ferromagnetism and basal plane helimagnetism; this is the conical helix.

In addition to the usual Q-scans made through the satellites and their respective Bragg reflections, Q-scans were also occasionally made across half a zone along  $c^*$  through the 101 and along  $a^*$  through the 002 reflections to

check for higher order harmonics of the modulation along the c-axis and for any in-plane modulation respectively. No peaks of magnetic origin were found in addition to those already observed at  $hk\zeta$ .

The magnetic moment per Gd ion,  $S_{Gd}$ , has been calculated from the 101 reflection and its satellites, and the resulting magnetization curve is shown in figure 5.6. The theoretical curve is also shown, and once more there is close agreement between the two. The shape of the curve is generally good everywhere, with saturation at  $7\mu_B$ . The same curve calculated from the 100 and 002 reflections is not quite so good and locally deviates slightly from the usual Brillouin form, as might be expected from the erratic behaviour of  $(S_{002})^2$  (figure 5.5). This is probably due to poor peak fitting of the 002 reflection, which often suffers distortion owing to the inclusion of the satellites by the resolution function. However, the overall trend of the curve is supported.

The temperature dependence of the turn angle over the fully ordered temperature range (figure 5.7) is akin to the behaviour for  $Gd_{64}Sc_{36}$ , and as the temperature is lowered the turn angle decreases smoothly until it appears to 'lock-in' at a temperature of  $-50$  K. Closer examination reveals that the turn angle wavers slightly below  $50$  K and does not in fact become 'steadfast' until  $30$  K where the turn angle is incommensurate at  $20.6 \pm 0.1^\circ$ . This value of turn angle is midway between the two commensurate values of  $21.2^\circ$  and  $20^\circ$  where the helix undergoes a full turn in 17 and 18 planes respectively. A plot of  $d\omega/dT$  against temperature is shown in figure 5.7b and demonstrates two points: first, the transition from helix to cone structure at  $56$  K (from ultrasound, see section 6.5.2) takes place at the same time that the turn angle is rapidly becoming temperature-independent. This may be coincidental, as  $Gd_{64}Sc_{36}$  shows similar behaviour but does not exhibit the helix/cone transition. Secondly, the turn angle is not properly locked-in, because  $d\omega/dT$  still has a finite albeit small value at  $20$  K.

Figure 5.5  $(S_q)^2$  vs. Temperature  
for Gd<sub>68</sub>Sc<sub>32</sub>

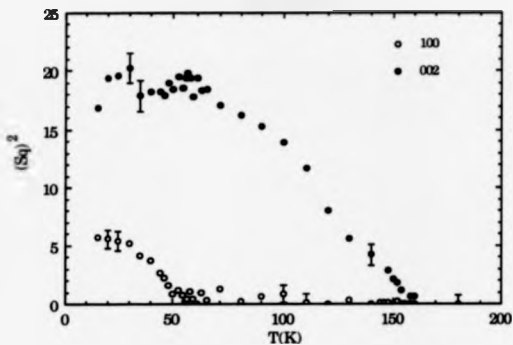


Figure 5.6 Mean Ionic Gd Moment vs. T  
for Gd<sub>68</sub>Sc<sub>32</sub>

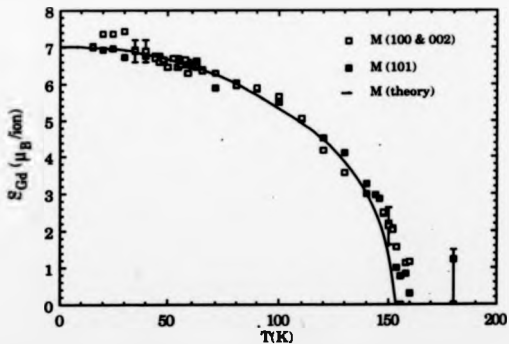


Figure 5.7 Turn Angle vs. Temperature  
for Gd68Sc32

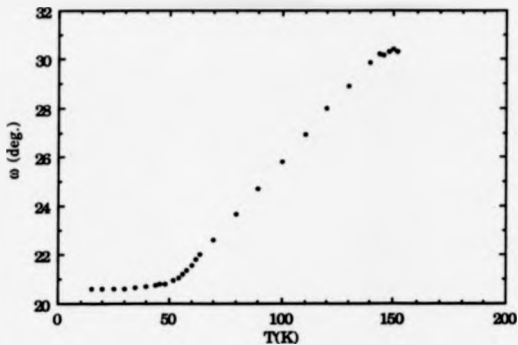


Figure 5.7b  $d\omega/dT$  vs. Temperature for Gd68Sc32

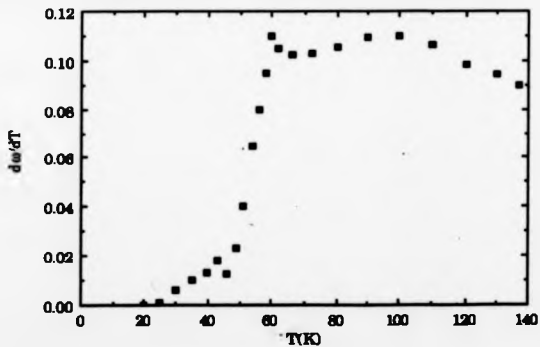
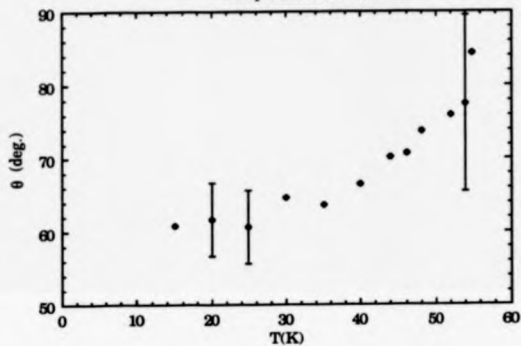


Figure 5.8 Semi-cone Angle vs.  
Temperature for Gd68Sc32





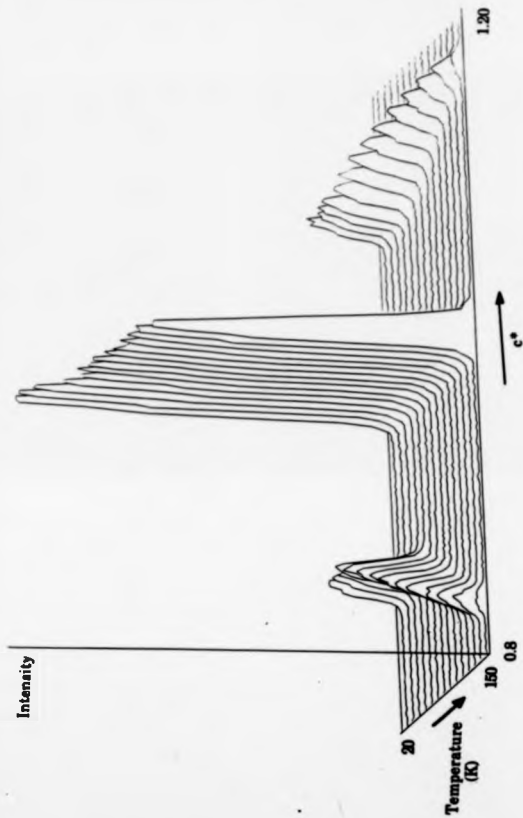


Figure 8.9 Isometric plot for Cd<sub>68</sub>S<sub>32</sub> constructed from  $c^*$  scans through the 101 reflection between 20 K and 150 K.

The low temperature conical structure of  $Gd_{68}Sc_{32}$  with its 'temperature-invariant' turn angle is outwardly similar to the structure of Ho below 20 K. In Ho, however, the turn angle is indeed locked-in at exactly  $30^\circ$ , commensurate with the lattice due to the strong in-plane crystal fields (Koehler, 1972). For  $Gd_{68}Sc_{32}$  the semi-cone angle (the angle between the moment vector and the c-axis) decreases uniformly as the temperature is lowered, reaching  $61^\circ$  at 15 K (figure 5.8). Figure 5.9 shows an isometric plot built up from Q-scans through 101 along  $c^*$  as a function of temperature. The conical phase is apparent from the enhancement of the central peak due to the ferromagnetic contribution. The 'lock-in' effect is also clearly visible. The satellite widths and the ferromagnetic component width always remain resolution-limited.

The different types of helix and cone structures were confirmed by refinement against sets of reflections measured at 105 K and 25 K.

### 5.3 $Gd_{70.5}Sc_{29.5}$

This sample exhibited the same two magnetic phases as  $Gd_{68}Sc_{32}$ . The increased percentage of Gd lifted the initial ordering temperature by 8 K to 162 K, and the transition to conical helix was raised by 35 K to 91 K, antiferromagnetic satellites being observed over the full magnetically ordered temperature range.

Figure 5.10 shows the temperature dependence of  $(S_q)_{100}^2$  and  $(S_q)_{002}^2$ .  $(S_q)_{002}^2$  is seen to be rather better behaved than for  $Gd_{68}Sc_{32}$  and the resulting magnetization curve is presented in figure 5.11 together with a theoretical curve scaled to  $7.4\mu_B$ . By contrast, the magnetization calculated using the 101 reflection is rather high. These results are also shown in figure 5.11. It is a good technique when measuring integrated intensities, to measure symmetry related reflections and average the magnetic intensities over all possible

Figure 5.10  $(S_q)^2$  vs. Temperature  
for Gd70.5Sc29.5

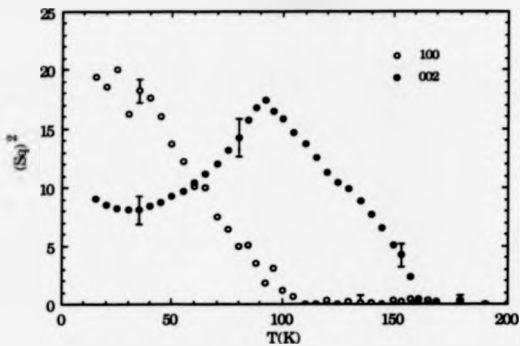


Figure 5.11 Mean Ionic Gd Moment vs. T  
for Gd70.5Sc29.5

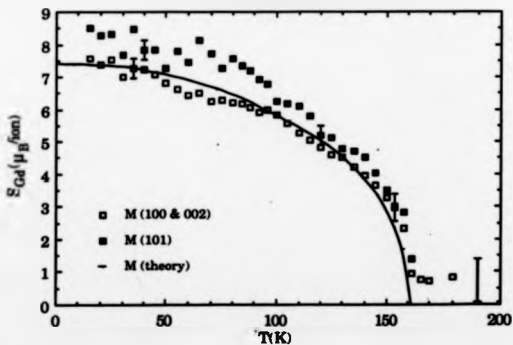


Figure 5.12 Turn Angle vs. Temperature  
for Gd70.5Sc29.5

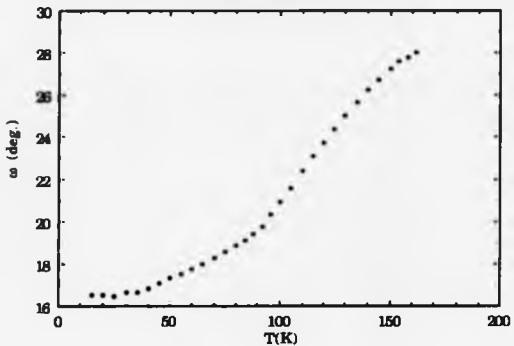
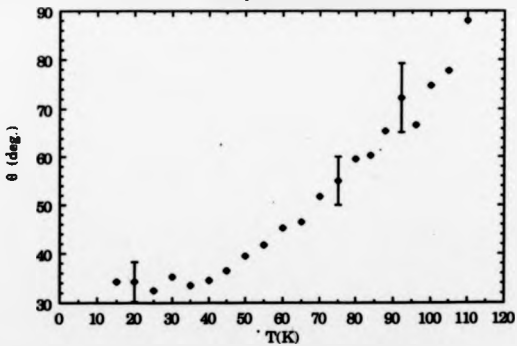


Figure 5.13 Semi-cone Angle vs.  
Temperature for Gd70.5Sc29.5



domain orientations, otherwise a preferred magnetic orientation may result in a higher or lower intensity being measured. This technique was used for  $\text{Gd}_{70.5}\text{Sc}_{29.5}$  and in figure 5.10,  $(S_q)_{100}^2$  represents the average over the 100, -110 and 010 reflections.  $(S_q)_{002}^2$  is averaged over the 002 and 0-0-2 reflections. Since this averaging was not carried out for the 101 reflection, the magnetization calculated from the 100 and 002 reflections should more accurately reflect the true behaviour, since variations from the mean of over 10% were observed.

The interlayer turn angle,  $\omega$ , is plotted as a function of temperature in figure 5.12. The onset turn angle is  $28^\circ$  and falls continuously until the helix/cone transition at 91 K where there is a discontinuity in the slope  $d\omega/dT$ . As the temperature is lowered still further,  $d\omega/dT$  tends to zero until at 30 K,  $\omega$  appears temperature-invariant at  $16.5 \pm 0.1^\circ$  (the nearest commensurate angle being  $16.36^\circ$ ). This is additional evidence that the change in  $d\omega/dT$  in  $\text{Gd}_{68}\text{Sc}_{32}$ , which is not nearly so sharp, is purely coincidental with the helix/cone transition. Such a discontinuity as observed in  $\text{Gd}_{70.5}\text{Sc}_{29.5}$  may, however, be expected due to the extra terms in the RKKY interaction introduced due to symmetry breaking at the transition. It is thus surprising that no discontinuity associated with the same transition is apparent in  $\text{Gd}_{68}\text{Sc}_{32}$ .

The semi-cone angle, calculated from  $(S_q)_{100}^2$  and  $(S_q)_{002}^2$  is plotted as a function of temperature in the conical helix phase in figure 5.13. It falls smoothly from  $90^\circ$  in the helical phase to approximately  $34^\circ$  at 40 K where it remains at much the same value down to 15 K. In both phases the magnetic peak widths remained limited by the resolution of D9.

#### 5.4 $\text{Gd}_{72}\text{Sc}_{28}$

This sample represented the composition richest in Sc to exhibit a simple ferromagnetic phase. This is in contrast with the Gd-Y system where the corresponding composition lies just below 40% Y. Figure 5.14 presents the

behaviour of  $(Sq)_{100}^2$  and  $(Sq)_{002}^2$  as a function of temperature, and once again these represent suitably averaged quantities as explained in the previous section.  $T_N$  is observed to be 167 K. A similar behaviour to the previous sample is exhibited at high temperature, with the rise in  $(Sq)_{002}^2$  and absence of  $(Sq)_{100}^2$  indicating a simple helical structure. At 113 K the rise in  $(Sq)_{100}^2$  indicates the presence of a c-axis ferromagnetic component coexisting with the helical structure as in Gd<sub>70.5</sub>Sc<sub>29.5</sub>. The steep decrease in  $(Sq)_{002}^2$  can again be explained in terms of the decrease in semi-cone angle in the conical phase. However for this composition,  $(Sq)_{002}^2$  returns at low temperature to its value in the paramagnetic phase, indicating that the semi-cone angle has decreased all the way to 0°, leaving a c-axis ferromagnetic structure. Also, the satellites disappear into the background; this is the onset of the c-axis ferromagnetic phase at ~54 K.

The spontaneous magnetic moment is calculated differently in the ferromagnetic phase than in the modulated phases. In the modulated phases,  $(Sq)_{100}^2$  is resolvable from the satellites and this intensity therefore gives the magnetization along the c-axis. The 002 reflection contains the contributions from the satellites which arise from the basal plane magnetization. The total spontaneous moment may thus be derived from the addition of  $(Sq)_{100}^2$  and  $(Sq)_{002}^2$  (eqns. 2.58 and 2.61). In the ferromagnetic structure,  $(Sq)_{002}^2$  will contain the magnetic intensity from basal plane components of ferromagnetism, whereas  $(Sq)_{100}^2$  will contain magnetic contributions from both the basal plane as well as the c-axis, since the scattering plane contains a basal plane direction. The magnetic moment may then be calculated from the summation  $(Sq)_{100}^2 + \frac{1}{2}(Sq)_{002}^2$  (eqns. 2.54 and 2.55).

The resulting magnetization curve (figure 5.15) is similar in shape to that calculated for Gd<sub>70.5</sub>Sc<sub>29.5</sub>. A theoretical curve is also presented for comparison with the results. Once more, the values of the magnetization obtained from the 100 and 002 reflections are in good agreement with the

theory. The magnetization calculated from the 101 reflection in the helical phase is rather high and probably arises due to a poor extinction correction. At several temperatures throughout the ordered temperature range, Q-scans were performed along  $c^*$  through half a zone through the 101 reflection to check for weak additional magnetic Bragg reflections which might arise from higher order  $c$ -axis modulations. No such peaks were found. Nor was anything revealed by performing half-zone scans in an  $a^*$  direction.

The temperature dependence of the semi-cone angle is given in figure 5.16 and of the turn angle in figure 5.17. The onset turn angle is  $26.5^\circ$  and there is the same discontinuity in slope as for  $\text{Gd}_{70.5}\text{Sc}_{29.5}$  at the helix/cone transition. The final turn angle is  $14.6^\circ$  at 54 K, whereupon the semi-cone angle approaches zero (fig. 5.16), and there is a transition to  $c$ -axis ferromagnetism.

Figure 5.18 shows an isometric plot of the scattered intensity during a Q-scan through the 101 reflection along the  $c^*$  axis as a function of temperature. This figure aids visualisation of several features of the magnetic behaviour, namely the development of the satellites, the discontinuity in the turn angle together with the appearance of a ferromagnetic moment in the cone phase, and finally the waning of the satellites as the ferro phase is approached. Once more the magnetic peak widths remain invariant throughout the ordered régime.

A remarkable discovery was made on this sample when the low temperature scans were closely examined. Very weak antiferromagnetic satellites, with a turn angle of about  $12^\circ$ , were observed along  $c^*$  for the 101 reflection at 14 K. Indeed, the elastic constant measurements had suggested the development of a new phase (or at least the modification of the ferromagnetic phase) at these temperatures (see section 6.5.1). The sample was re-examined by neutron diffraction at a later date with the purpose of identifying the magnetic structure corresponding to the satellites. However,

Figure 5.14  $(S_q)^2$  vs. Temperature  
for Gd72Sc28

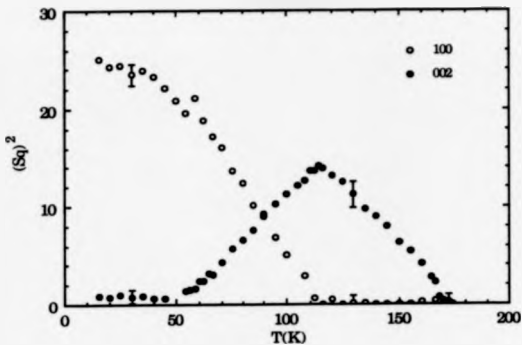


Figure 5.15 Mean Ionic Gd Moment vs. T  
for Gd72Sc28

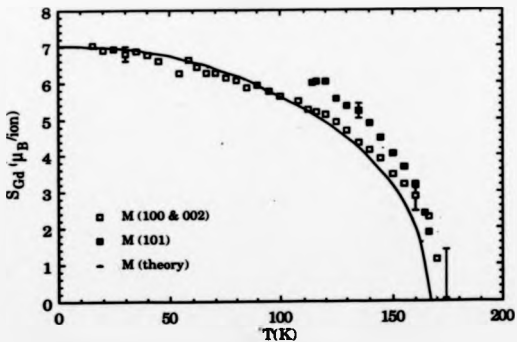




Figure 5.16 Semi-cone Angle vs.  
Temperature for Gd72Sc28

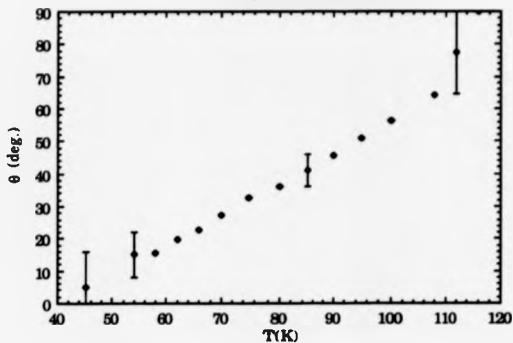
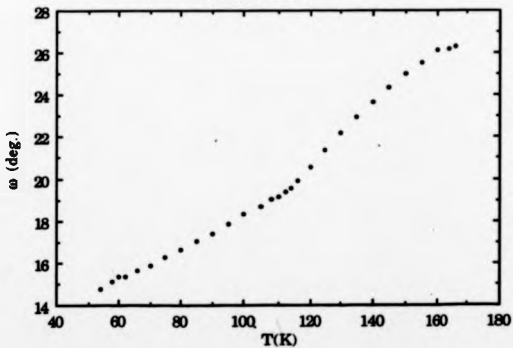


Figure 5.17 Turn Angle vs. Temperature  
for Gd72Sc28



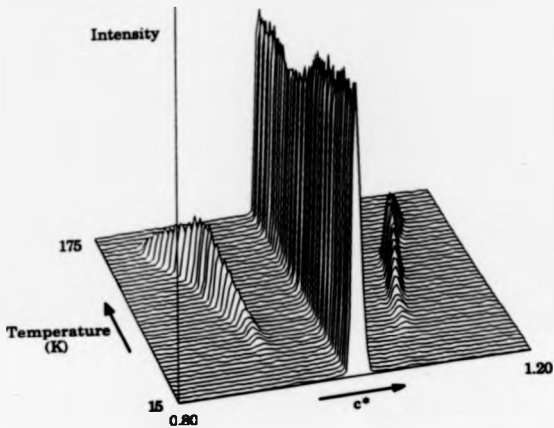


Figure 5.18 Isometric plot for Gd<sub>72</sub>Sc<sub>28</sub> constructed from  $c^*$  scans through the 101 reflection between 15 K and 175 K.

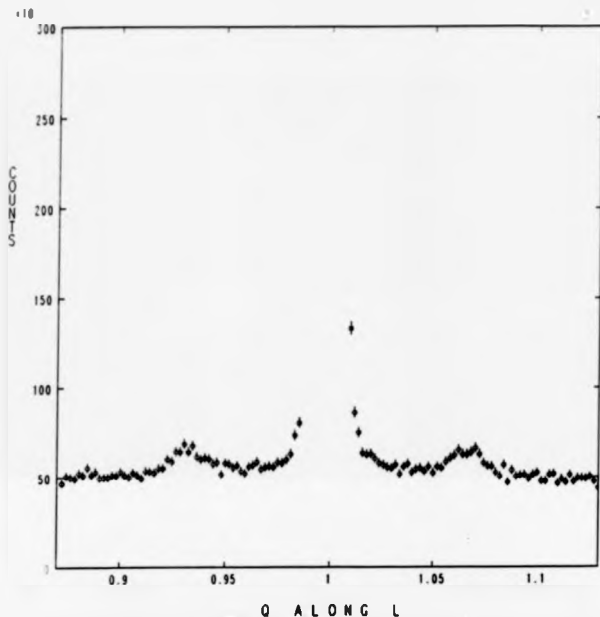


Figure 5.19 Scattering profile along  $c^*$  through the 101 reflection for  $Gd_{73}Sc_{27}$  at 15 K, magnified to show the low-temperature satellites.

even though the satellites were seen again on the 101 reflection (figure 5.19), they were too weak to be observed on any other reflection, except the -210 where they were only just visible. No additional satellites corresponding to further modulations were observed along  $c^*$  for the 101. Since the satellites observed are very weak, the principal magnetic structure at these low temperatures is still a  $c$ -axis ferromagnet. The satellites, being spaced along  $c^*$ , can only correspond to a  $c$ -axis modulation of the moments. This may arise in two ways: there may be a small modulated basal plane component of the moments (conical phase with small, finite, semi-cone angle), or it may arise from domain walls between the two possible types of  $c$ -axis ferromagnetic domains. A  $180^\circ$  Bloch wall between two such domains contains about 15 spins, if the approximate value of the  $q$ -vector is used to determine how the moments rotate about a basal plane direction from one domain to the other. The satellites were only observed below 18 K, and unfortunately the low temperature limit of the cryostat (13.5 K) precluded further studies.

### 5.5 Gd<sub>75</sub>Sc<sub>25</sub>

Elastic constants measured as a function of temperature for this sample revealed initial ordering at 179 K into a magnetic phase existing for only about 7 K below this temperature. Due to the restricted temperature range of the phase and the proximity of the magnetic order/disorder transition, it proved very difficult to determine the magnetic structure even with long count times. The temperature dependence of  $(S_q)_{100}^2$  and  $(S_q)_{002}^2$  is shown in figures 5.20a and 5.20b respectively. In the initial ordered phase between 179 K and 172 K,  $(S_q)_{002}^2$  remains approximately zero, while  $(S_q)_{100}^2$  clearly exhibits a small peak in the same region. No antiferromagnetic satellites were observed. A more detailed study of the region involving much longer count times gave the results shown in figure 5.21. Here, the simple integrated intensities are plotted

to show the true scatter of points. There is a definite enhancement of the 100 intensity below 179 K (fig. 5.21a), whereas the 002 appears to show a truly random scatter of points until about 172 K when it begins to increase (fig. 5.21b). By themselves, the neutron data in this initial phase suggest the existence of a c-axis ferromagnetic structure. Intuitively, however, such a structure is difficult to reconcile in view of the cone phase which follows at 172 K. It was recognised that the results did not refute the possibility of a ferro-I type structure in this phase, but more direct evidence was required. Resistivity measurements on this alloy have provided useful complementary evidence as to the magnetic structure in this region (see chapter 7).

At 172 K, there is a transition to a conical helix structure as evidenced by satellites at  $hk\zeta$  and the presence of magnetic scattering observed on the 100 reflection as well as the 002 reflection. The cone phase exists only down to 140 K whereupon the satellites disappear and there is a transition to c-axis ferromagnetism. Magnetic intensity on the 002 reflection remains absent between 140 K and 40 K, although the scatter of points above zero is rather large (fig. 5.20b). At 40 K there is a sharp increase in  $(Sq)_{002}^2$  which would normally be accompanied by a corresponding fall in  $(Sq)_{100}^2$  in a ferromagnetic phase, indicating a spin-reorientation transition where the moment moves away from the c-axis toward the basal plane. It is puzzling in this case, however, that the drop in  $(Sq)_{100}^2$  is not coincident with the rise in  $(Sq)_{002}^2$ , but takes place some 10 K lower in temperature. As a result, the ionic magnetization as a function of temperature (fig. 5.22) exhibits a distinctive peak at around 30 K. Furthermore, the  $(Sq)_{100}^2$  and  $(Sq)_{002}^2$  curves are reproducible on warming (fig. 5.20) and therefore the peak is also observed again on warming. Considering the well-behaved nature of the rest of the magnetization curve, which saturates at  $\sim 7\mu_B$  per Gd ion, this feature is unusual, and remains unexplained at present.

The behaviour of the turn angle is shown in figure 5.23. Contrary to  $\text{Gd}_{72}\text{Sc}_{28}$ , on approaching the ferromagnetic phase there appears to be a precipitous fall of the turn angle toward zero. It is difficult to ascertain whether the turn angle does in fact go to zero since more points just below 140 K are ideally required. However it can be safely said that if this is the case, the turn angle tends to zero very rapidly because at 140 K,  $\omega=17.6^\circ$  and at 138 K the satellites have gone. Nevertheless, the transition to ferromagnetism here is similar to  $\text{Gd}_{72}\text{Sc}_{28}$  in that it takes place on account of the semi-cone angle tending to zero. The magnetic peak widths remained resolution-limited at all temperatures below the ordering temperature.

The temperature dependence of the canting angle over the full ordered temperature range is shown in figure 5.24. In the cone phase, the angle decreases from about  $45^\circ$  to zero at 140 K, where there is a transition to c-axis ferromagnetism. This transition is more convincingly apparent from figures 5.20a and 5.20b. (There is a substantial scatter of points between 140 K and 40 K in figure 5.24 which arises because in the c-axis magnetic structure, small fluctuations in the 002 intensity tend to be amplified by the arctan function used to evaluate  $\theta$ ; the error in these points is correspondingly large. Points evaluated below the zero line have been placed on the zero line to show where the measurements were taken, and it may thus be noticed that there are in fact a roughly equal number of points above and below the line.) At 40 K, the enhancement of the 002 reflection means the moments have begun to turn away from the c-axis. The anomaly in the magnetization at 30 K does not have a pronounced effect on the canting angle at this temperature. The final canting angle measured was  $73^\circ$  at 15 K.

Figure 5.20a  $(S_q)^2$  vs. T for 100 reflection  
for Gd75Sc25

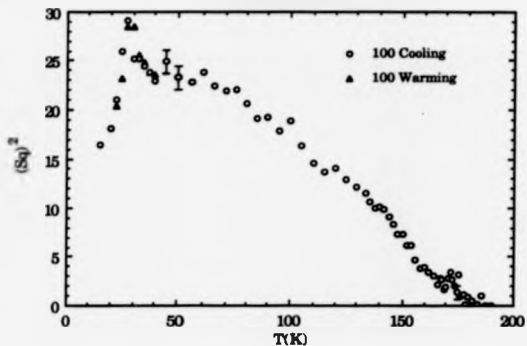


Figure 5.20b  $(S_q)^2$  vs. T for 002 reflection  
for Gd75Sc25

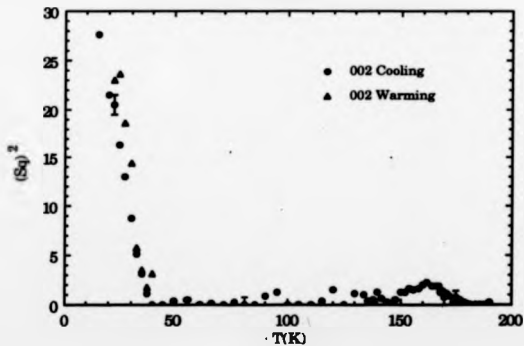


Figure 5.21a Gd75Sc25 : Integrated Intensity vs. T  
for 100 in Initial Ordering Regime

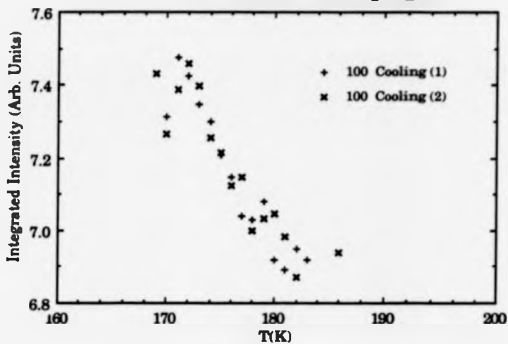


Figure 5.21b Gd75Sc25 : Integrated Intensity vs. T  
for 002 in Initial Ordering Regime

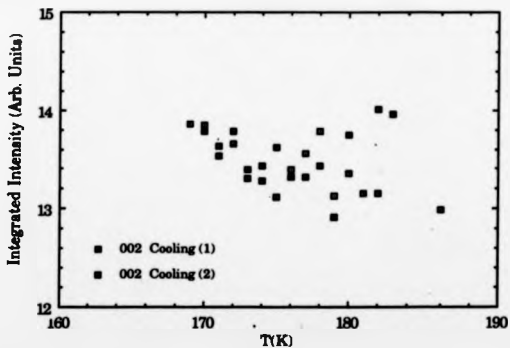




Figure 5.22 Mean Ionic Gd Moment vs. T  
for Gd75Sc25

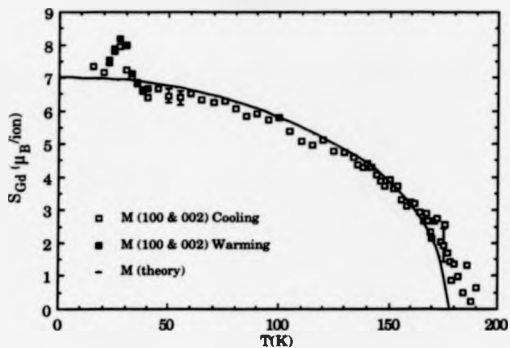


Figure 5.23 Turn Angle vs. Temperature  
for Gd75Sc25

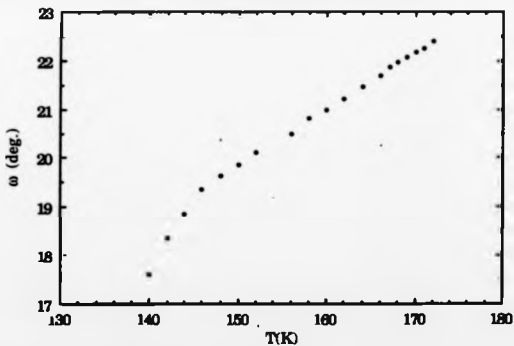
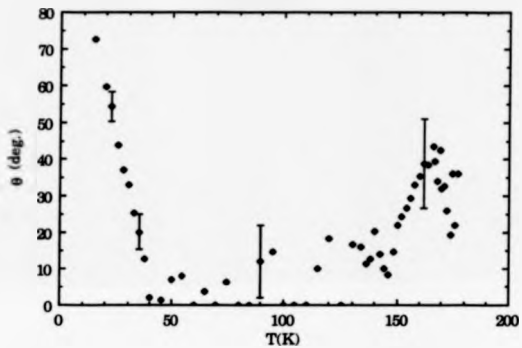


Figure 5.24 Canting Angle vs. Temperature  
for Gd<sub>75</sub>Sc<sub>25</sub>



5.4 Gd<sub>75</sub>Sc<sub>25</sub>

Only ferromagnetic contributions to the nuclear reflections were observed for this sample. Figure 5.25 shows the temperature dependence of  $(S_q)_{000}^2$  and  $(S_q)_{002}^2$  taken on cooling and warming. It is clear from figure 5.25 that a c-axis ordered structure develops at a Curie temperature,  $T_c=187$  K. Elastic constant measurements on this sample revealed the presence of an initial phase possibly of the same nature as that observed by neutrons in the Gd<sub>75</sub>Sc<sub>25</sub> sample just below  $T_c$ . However, in this sample the phase exists only over a range of 2 K at the most below  $T_c$ . As such it was found to be almost impossible to investigate the phase with neutrons for the simple reason that the temperature range was too restrictive to observe any trends in the measurements.

Careful analysis of the scans through the 002 reflection revealed the presence of underlying broad, weak and diffuse magnetic components between  $T_c$  and 120 K, but most noticeable in the vicinity of  $T_c$ . Figure 5.26 shows two scans taken at 186 K and 200 K and also their difference. The 002 scans, fitted with an extra peak to account for the diffusive component, result in a flat response from the resolution-limited peak, which is expected for a c-axis ferromagnet. The significant values of  $(S_q)_{002}^2$  at high temperature in figure 5.25 are therefore solely attributable to the diffusive component and could easily be misinterpreted as being due to a finite canting angle.

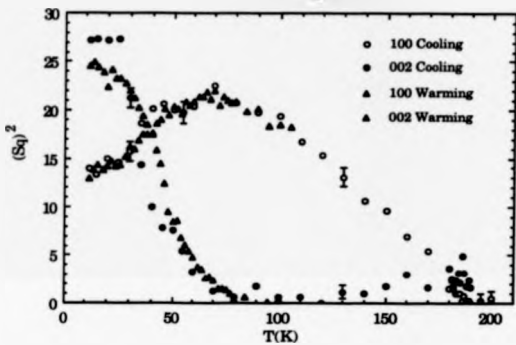
The peak fitted to the difference of the two scans shown in figure 5.26 is a Gaussian peak, and does not represent the true peak profile. In fact the peak is distinctly Lorentzian in profile, which is clear evidence of short-range basal plane order coexisting with c-axis ferromagnetic order; it is incongruous with the diffraction profile from small, long-range ordered clusters (domains) which would present a Gaussian lineshape for the diffusive component (Cowley and Bruce, 1981, Lovesey, 1984). This observation indicates that the

alloy is exhibiting a strong tendency for a ferro-I-like structure near to  $T_c$  which decreases as the temperature is lowered and fully developed long-range order sets in. The diffusive component is hardly noticeable on warming from low temperatures even on approaching  $T_c$ , suggesting that once long-range order sets in, it remains stable.

The temperature dependence of the magnetization per Gd ion is shown in figure 5.27 as calculated from the original experiment. The experimental points appear to have a good Brillouin form, although the saturation moment is a little low at  $\sim 6.8\mu_B$ . Once more, this is most likely due to an imperfect extinction correction. Below  $\sim 85$  K the moments steer away from the c-axis in a manner reminiscent of pure Gd below its spin reorientation transition at  $\sim 220$  K. Contrary to Gd, however, the moments do not revert back towards the c-axis. The temperature dependence of the canting angle is shown in figure 5.29 where the steady increase in  $\theta$  to a final value of  $80^\circ$  may be observed, at which point the moment vectors lie almost in the basal plane.

Occasionally, Q-scans were performed along  $c^*$  through half a zone through the 101 reflection to check for magnetic Bragg reflections which might arise from any c-axis modulations. No additional peaks were found. The ordered structure was confirmed as being ferromagnetic by refinement against extensive sets of reflections at 30 K, 50 K and 170 K. It is therefore concluded that the sample is ferromagnetic below  $T_c=187$  K, with a spin reorientation transition at  $\sim 85$  K.

Figure 5.25  $(S_q)^2$  vs. Temperature  
for Gd<sub>76.7</sub>Sc<sub>23.3</sub>



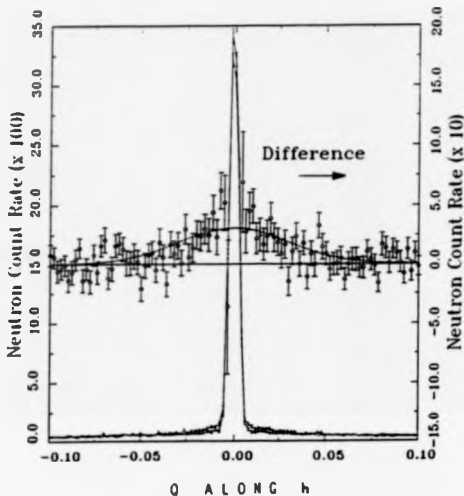


Figure 5.26 Two  $a^*$  scans through the 002 reflection for Gd<sub>76.78</sub>Sc<sub>23.3</sub> at 200 K and 186 K. The difference between the scans is also shown together with a Gaussian fit to the profile. In fact the profile appears Lorentzian rather than Gaussian.

Figure 5.27 Mean Ionic Gd Moment vs. T  
for Gd<sub>76.7</sub>Sc<sub>23.3</sub>

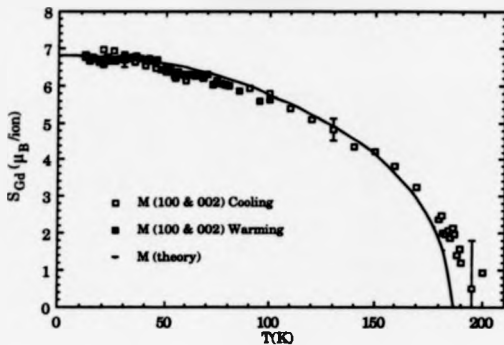
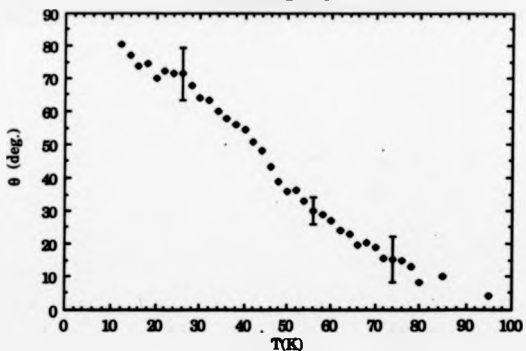


Figure 5.28 Canting Angle vs. Temperature  
for Gd<sub>76.7</sub>Sc<sub>23.3</sub>



## 6

## Ultrasonic Studies of Crystal Elastic Constants of Gd-Sc Alloys

**Introduction**

Measurements of acoustic velocity and attenuation may be used as a probe for investigating magnetic systems, as a consequence of the magneto-elastic interactions which couple the spins to the ionic lattice. In ultrasound experiments, it is the mechanical susceptibility (inappropriately, but more commonly called the elastic constant) that is measured. Furthermore, it has been shown (Fossheim and Fossum, 1984) that the elastic constants are simply related to the order parameter susceptibility, and may therefore display anomalous behaviour at magnetic phase transitions (driven by parameters such as temperature, pressure and applied magnetic field).

Much information related to anisotropy constants, magnetostriction constants, critical behaviour etc. may be derived from such measurements. However, the main purpose of ultrasonic measurements in this study has been to characterize the samples by delineating their various magnetic phases as a function of temperature, and, in conjunction with neutron diffraction experiments, to construct an accurate magnetic phase diagram. From considerations of magnetic symmetry, additional information may also be gleaned about particular phases simply from the type of elastic constant behaviour.



### 6.1 Magnetoelastic Effects in Gd-Y and Gd-Sc Alloys

Acoustic measurements of magnetic systems may only be understood if the nature of the interactions between the ionic and magnetic subsystems are known. Due to their bewildering complexity, these interactions are almost invariably treated from a phenomenological stand-point under the umbrella name 'magnetoelastic effects'. For the purpose of description, it is convenient to divide magnetoelastic coupling into 1) an equilibrium coupling between the lattice and spins and 2) a dynamic coupling between the lattice vibrations (phonons) and magnetic excitations (spin waves) treated as a perturbation on the equilibrium state.

When a crystal becomes magnetically ordered, the equilibrium coupling generally leads to a distortion which is termed magnetostriction. The magnitude of such a distortion is fairly small, while the form of the distortion can be expected to be compatible with the reduction in symmetry accompanying magnetic ordering. As a first stage in developing a formal treatment of magnetostriction, we recall the conventional method of representation of the elastic properties of a crystal by a fourth rank tensor (Musgrave, 1970, Nye, 1964). This arises as follows: suppose that P and Q are two points with coordinates  $x_i$  and  $x_i + \Delta x_i$  respectively in an unstrained crystal. Suppose also that the displacement of these points in the strained state are  $u_i$  and  $u_i + \Delta u_i$ . Then we may write

$$\Delta u_i = \sum_k \frac{\partial u_i}{\partial x_k} \Delta x_k. \quad (6.1)$$

$\frac{\partial u_i}{\partial x_k}$  is a tensor of 2nd rank and is the strain tensor. The strain tensor may be considered as the sum of its symmetric and antisymmetric parts: the antisymmetric part of the strain tensor describes rotations and translations

which do not interest us here. However, the symmetric part,  $\eta_{ik}$ , describes the deformation which is

$$\eta_{ik} = \frac{1}{2} \left( \frac{\partial u_i}{\partial x_k} + \frac{\partial u_k}{\partial x_i} \right). \quad (6.2)$$

Since, by its nature, the stress causing this deformation must also be a tensor of rank 2 ( $\sigma_{ij}$ ), the generalized version of Hooke's Law for a crystal takes the form

$$\sigma_{ij} = \sum_{kl} C_{ijkl} \eta_{kl}. \quad (6.3)$$

The elastic properties of the crystal are therefore described by  $C_{ijkl}$ , a tensor of rank 4 whose elements are the elastic stiffness constants. The elastic energy density is given by

$$U = \frac{1}{2} \sum_{ijkl} C_{ijkl} \eta_{ij} \eta_{kl}. \quad (6.4)$$

The symmetry of the stress and strain tensors implies that there are 6 independent choices for the pairs of suffices  $ij$  and  $kl$ . Hence  $C_{ijkl}$  can have, at most, 36 independent elements owing to relations of the form:

$$C_{ijkl} = C_{ijlk} = C_{jikl} = C_{jilk}. \quad (6.5)$$

In fact, due to the symmetry between the two pairs of suffices  $ij$  and  $kl$ , there can be at most 21 independent tensor elements, and often far fewer because of additional symmetry restrictions gained from the point group symmetry of the crystal.

In order to describe the magnetostrictive effect, we need to express the magnetic free energy density,  $V$ , of the crystal as a function of the strain components. Because the magnetostrictive distortion is usually small, we may expand  $V$  in a Taylor series. Retaining the first two terms, we get

$$V = V^0 + \sum_{ij} V_{ij}^1 \eta_{ij}. \quad (6.6)$$

The physical significance of these two terms is easy to see. The first is the anisotropy at zero strain, while the second term represents the interaction between the magnetic anisotropy and the strain, and is referred to as the 'magnetoelastic energy density'. The coefficients  $V^0$  and  $V_{ij}^1$  will be a function of temperature. Moreover, as a consequence of the magnetic anisotropy, they will depend on the orientation of the magnetization relative to the crystal axes, and as such may be expanded in terms of the direction cosines  $\alpha_i$  of the spontaneous magnetization relative to the axes  $Ox_1x_2x_3$ :

$$V^0 = k_{ij}^{(1)} \alpha_i \alpha_j + k_{ij}^{(2)} k_{kl} \alpha_i \alpha_j \alpha_k \alpha_l, \quad (6.7a)$$

$$V_{ij}^1 = b_{ijkl} \alpha_k \alpha_l. \quad (6.7b)$$

The deformation arising from the spontaneous magnetostriction can now be determined by minimizing the sum of the elastic energy density  $U$  and the magnetic energy density  $V$  with respect to the components of the strain  $\eta_{ij}$ .

i.e. at equilibrium we have

$$\frac{\partial(U+V)}{\partial \eta_{ij}} = 0 \quad (6.8)$$

for all  $\eta_{ij}$ . The condition imposed by (6.8) will produce a new set of equations from which either new equilibrium elastic constants may be found in terms of the anisotropy coefficients,  $k_{ij}^{(1)}$  and  $k_{ij}^{(2)}$ , or new equilibrium anisotropy constants may be found in terms of the elastic coefficients,  $C_{ijkl}$ . It is important to realize that these two interpretations are manifestations of one and the same effect, so that the new state may be described by renormalized anisotropy constants or renormalized elastic constants, depending on which description best fits the particular situation. When making ultrasonic measurements of the elastic constants therefore, the new equilibrium state of the crystal will show up as a change in the elastic constant being measured.

In summary, the magnetic ordering of the system (and also moment reorientation or order-order transitions) leads to magnetostrictive strains

which may break the crystal symmetry. The ordering deformation may then be seen as a renormalization of some or all of the elastic constants of the original symmetry.

At the phase transitions themselves, it is the dynamic magnetoelastic coupling which will dominate the response of the elastic constants being measured. There are two types of coupling depending on the type of transition; for spin-reorientation transitions, the magnetocrystalline anisotropy is responsible for the easy axis change, therefore the sound wave-soft mode coupling is of the linear magnetostrictive type. The soft mode associated with the transition affects only a small region of Q-space and it has been shown (Gorodetsky et al. 1971) that the main effects are due to a resonant interaction between the sound wave and the soft mode (one magnon-one phonon coupling). This is in contrast to the magnetic order-disorder transition at the Curie or Néel point where the coupling arises from the strain modulation of the exchange interaction (volume magnetostrictive coupling). In this case the whole spin-wave spectrum becomes soft giving rise to large fluctuations in the order parameter. The sound wave couples to the spin fluctuations thus exhibiting pronounced attenuation singularities (two magnon-one phonon coupling).

### **6.2 Elastic Constants in the Hexagonal Crystal System**

We have already seen how the strain induced by an applied stress may be written as a generalized form of Hooke's Law using the 4th rank elastic stiffness tensor  $C_{ijkl}$  (6.3). Following Musgrave (1970), we may simplify this expression due to symmetry relations of the stress strain tensors ( $ij=ji$  from the Cauchy relations) and by using an abbreviated notation:-

Tensor	11	22	33	23,32	31,13	12,21	
Matrix	1	2	3	4	5	6	, (6.9)

giving

$$\sigma_i = \sum_{k=1}^6 C_{ik} \eta_k \quad (6.10)$$

For crystals of hexagonal symmetry, there are 5 independent constants,  $C_{11}$ ,  $C_{13}$ ,  $C_{33}$ ,  $C_{44}$  and  $C_{66}$ . The changes in these elastic constants caused by magnetic order can be directly studied by observing the behaviour of ultrasonic elastic waves propagating along high symmetry directions. The measured velocities are then related to the elastic constants by the relations:-

propagation along c-axis

$$\begin{aligned} C_{33} &= \rho V_{\text{long}}^2 \\ C_{44} &= \rho V_{\text{shear}}^2 \quad (\text{any polarization}) \end{aligned}$$

Propagation in the basal plane (a or b axis),

$$\begin{aligned} C_{11} &= \rho V_{\text{long}}^2 \\ C_{44} &= \rho V_{\text{shear}}^2 \quad (\text{polarised along the c-axis}) \\ C_{66} &= \rho V_{\text{shear}}^2 \quad (\text{polarised in the basal plane}). \end{aligned}$$

( $C_{13}$  can be measured by propagating shear waves at  $45^\circ$  to the c-axis).

Finally, it should be noted that measurements of elastic constants by acoustic wave propagation will be adiabatic since the local heat dissipation is slow compared to the wave velocities.

### 6.3 Experimental Technique for Measurement of Ultrasonic Wave Velocities

Over several years now, the Pulse Echo Overlap (PEO) technique (Hallier et al., 1975) has established itself as a convenient method for determining elastic constants. The technique works on the principle of being able to

measure with high relative accuracy the time of flight of an acoustic pulse which has travelled up and down the sample. This is achieved by triggering an oscilloscope at a suitable frequency to allow the apparent overlap of two chosen echoes in the acoustic echo train. The frequency will be that corresponding to the time period between the two chosen echoes. Knowing the path length, the sound velocity may be calculated, and the elastic constant appropriate to the propagation direction in the crystal is then simply proportional to the square of the measured velocity.

A block diagram of the measuring system is shown in figure 6.1. An ultrasonic pulse is driven from a 15MHz quartz transducer (X-cut for longitudinal, Y-cut for shear) bonded to the face of the sample with Araldite epoxy resin. The transducer is excited by a radio frequency pulse from a Matec 950 r.f. pulse generator, and the echo train produced by successive reflections of the acoustic pulse from the ends of the sample is displayed on the oscilloscope screen. In order to overlap two chosen echoes from this trace, the oscilloscope must be triggered externally at a frequency equal to the reciprocal of the time period between these echoes. This is done by selecting the appropriate frequency from a frequency synthesizer. This trigger frequency, reduced by a decade divider also drives the pulse generator, ensuring that the echoes from one pulse have decayed before the next pulse is triggered. A double strobe pulse is also triggered by the reduced frequency such that only the two echoes of interest are displayed on the oscilloscope screen. Any change in the sound velocity will be shown by a relative movement between the overlapped echoes, and adjustments to the synthesizer can bring the echoes back into alignment and the new velocity calculated from the new frequency. Ultrasonic attenuation measurements were also made by using a Matec 9000 comparator to fit log functions to the decaying echo train.

Interfacing the overlap frequency (as read by the frequency synthesizer) and the thermocouple emf (as read by the digital voltmeter) to a

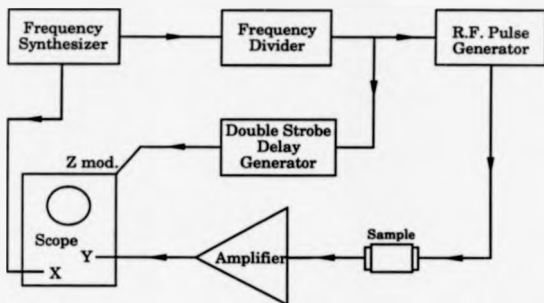


Figure 6.1 Block diagram of pulse-echo overlap system

microcomputer is advantageous (Patterson, 1986). Not only does it make the taking of readings as simple as pressing a button, but more importantly enables them to be done quickly. For in the time it takes to adjust the overlap frequency and note the readings, a phase transition is easily missed. Such a system was constructed for the purposes of this study.

The relative accuracy of the PEO technique is limited by the oscilloscope resolution and the sensitivity of the frequency synthesizer. For this study a Syntest 81-102 frequency synthesizer gave a limiting sensitivity of 1 part in  $10^6$ . The absolute accuracy of the measurements is much poorer by contrast, being limited by several factors. For example the bond type and thickness will lead to uncertainties which are difficult to evaluate. Blackie (1981) has made a study of the limiting factors and has estimated that for a well prepared crystal with faces planed parallel to within 2 microns, the absolute accuracy is about 5%. Further errors are introduced due to the fact that it is very difficult to determine which of the individual oscillations within the wave packets to overlap; it is estimated that an additional 2-3% error must be included for each high frequency peak misalignment. We have partially overcome this problem by using a spike generator to produce a narrow resonant wave packet and a digitizing oscilloscope for accurate time delay measurement.

A conventional Oxford Instruments continuous flow cryostat was used to attain temperatures from 8-300 K with an absolute accuracy of  $\pm 1$  K. The temperature was controlled automatically and enabled variable sweep rates to be selected (normally between 1/2 and 2 K/min). A cross-check of the magnetic transition temperatures with those obtained from the neutron diffraction studies showed the temperature measurements to be correct to within the stated limits of accuracy.



#### 6.4 Temperature dependence of Elastic Constants of Gd-Sc Alloys

The results of the temperature variation of the elastic constants are now presented. Since the samples prepared had faces planed parallel to allow ultrasonic wave propagation in the basal plane and the *c*-axis, the four elastic constants  $C_{33}$ ,  $C_{44}$ ,  $C_{11}$  and  $C_{66}$  could, in principle, be measured. However during cooling, the much larger thermal contraction and magnetostriction along the *c*-axis than in the basal plane meant that great difficulty was experienced in maintaining a good bond to a transducer on a face parallel to the *c*-axis. The Araldite bond proved too brittle for measurement of  $C_{11}$  or  $C_{66}$ , so vacuum grease and silicone grease were tried of which the silicone grease gave the better coupling at lower temperatures. The silicone grease allowed measurements of  $C_{11}$  to be made down to about 130 K, below which the echoes were lost in the background noise.

The results are presented with the elastic constants normalized to their value at room temperature. The absolute values of the elastic constants measured at 295 K are given in table 6.1, from which the graphs may be appropriately scaled. The absolute values at room temperature compare favourably with an extrapolation between the room temperature elastic constants of pure Sc (Wakabayashi et al., 1971) and pure Gd (Elliot, 1972). The elastic constants of Sc are considerably harder than those of Gd, and a decreasing trend in the constants with increasing Gd is evident from the table.

Results from the  $Gd_{73}Sc_{27}$  sample are presented first since it exhibits the three main magnetically ordered phases of the Gd-Sc alloys; ferromagnetic, conical helix and basal plane helix. This forms a basis from which one may understand the principal features of the other samples, whose peculiarities are treated individually.

Table 6.1. Crystal elastic constants of Gd-Sc alloys at 295 K

Sample	Density (Kgm <sup>-3</sup> )	Elastic Constant ( $\times 10^{10}$ Pa)	
Gd <sub>64</sub> Sc <sub>36</sub>	6133	C <sub>33</sub>	7.64
		C <sub>44</sub>	2.16
Gd <sub>69</sub> Sc <sub>31</sub>	6329	C <sub>33</sub>	7.60
		C <sub>44</sub>	2.09
Gd <sub>69</sub> Sc <sub>31</sub>	6378	C <sub>33</sub>	7.60
Gd <sub>70.5</sub> Sc <sub>29.5</sub>	6452	C <sub>33</sub>	7.64
Gd <sub>72</sub> Sc <sub>28</sub>	6526	C <sub>33</sub>	7.52
		C <sub>44</sub>	2.12
		C <sub>11</sub>	6.80
Gd <sub>75</sub> Sc <sub>25</sub>	6673	C <sub>33</sub>	7.48
		C <sub>44</sub>	2.11
Gd <sub>76.78</sub> Sc <sub>23.22</sub>	6757	C <sub>33</sub>	7.44
		C <sub>44</sub>	2.10
		C <sub>11</sub>	6.56

Densities have been calculated from values for Gd and Sc obtained from the Handbook on the Physics and Chemistry of Rare-Earths, (Gschneider K.A. and Eyring L., 1978).

#### 6.4.1 Gd<sub>72</sub>Sc<sub>28</sub>

##### C<sub>33</sub> dependence

The temperature dependence of C<sub>33</sub> is shown in figure 6.2a. The data presented here is for cooling from 300 K to 6 K and also warming back to 300 K. It can be immediately seen that the initial magnetic ordering takes place at 167 K. Also, there are four magnetically ordered phases below this temperature, the transition temperatures being at 113 K, 80 K and 14 K.

Let us examine the behaviour of C<sub>33</sub> at the initial ordering temperature.

At temperatures greater than 167 K, we may consider the system to be magnetically disordered, i.e. paramagnetic, however the convex nature of C<sub>33</sub> indicates magnetoelastic coupling in this régime. This is in fact the volume magnetostrictive coupling mentioned earlier. A departure from the unperturbed C<sub>33</sub> behaviour (linear to a good approximation below the Debye temperature) is observed because the coupling is dependent on the correlation between spins on different sites. The correlation will be non-zero well above the ordering temperature, T<sub>N</sub>, because of magnetic short-range order, and will increase as T<sub>N</sub> is approached. The changes in ultrasonic velocity above a critical temperature, T<sub>c</sub>, can be generally expressed (Laramour, 1969):-

$$\frac{\Delta V}{V} \propto \left( \frac{T - T_c}{T_c} \right)^{-\zeta} \quad (6.11)$$

where the critical exponent ( $\zeta$ ) of the reduced temperature is less than 0.2. As this expression is independent of the spin fluctuation time, one can see that this type of critical coupling will occur whether the material orders ferromagnetically or antiferromagnetically.

In the initial ordered phase, which is the basal plane helical structure, the increase of C<sub>33</sub> towards an unperturbed value is consistent with the fact that the moments lie in the basal plane, since this structure is intrinsically

'hard' for longitudinal waves propagating down the *c*-axis (cf. Dy). However, when the second ordered phase (conical helix) sets in at 113 K, the attenuation of the ultrasound becomes extremely high to the point where the echo train is virtually non-existent. Although there is no data in this region,  $C_{33}$  has undoubtedly softened in this phase, since it is observed to grow at the onset of the low temperature phase. The high attenuation and resulting  $C_{33}$  softening point to a magnetic structure where the moments lie somewhere between the *c*-axis and the basal plane, for now two mechanisms contribute to the high attenuation: first, the magnetoelastic interaction where the canting angle is very sensitive to *c*-axis strain producing strong coupling between the *c*-axis longitudinal wave and the canted structure, and secondly, the dissipation of the elastic wave energy at the domain walls now existent due to the *c*-axis components of the structure.

No hysteresis was observed in the basal plane helix phase on warming from the low temperature ferromagnetic phase, as can be seen from figure 6.2a. At first this seems remarkable when compared to the Gd-Y system where there are large hysteresis effects (Blackie and Palmer, 1982; Braga et al., 1982). The observed hysteresis there has been explained in terms of the two different helical domain types that have been observed to form on warming to, or cooling to, the periodic phase (Patterson, 1986). The domain walls of these two domain types will interact with the ultrasound in different ways and cause hysteresis (Palmer, 1975). In the Gd-Sc system, the situation is different in that the transition from basal plane helix to *c*-axis ferromagnetism takes place via the conical helix phase. The transitions are continuous, being driven purely by the changing out-of-plane anisotropy.

The low-temperature phase of  $Gd_{72}Sc_{28}$  is a *c*-axis ferromagnetic structure, again a 'hard' structure for  $C_{33}$ , which is why there is rapid increase in  $C_{33}$ . It is unclear what type of magnetic structure follows on from this below 14 K from the neutron experiment, but the  $C_{33}$  softening would

indicate a return to a canted structure. We postpone a discussion of the low temperature behaviour till later.

So far we have discussed, without much justification, the  $C_{33}$  elastic constant behaviour in terms of lattice hardening and softening for particular structures. We shall now reduce the magnetic structures to an effective symmetry representation and explain the elastic constant anomalies in terms of symmetry breaking effects.

#### Anomalous $C_{33}$ elastic constant behaviour and magnetic symmetry changes

If the ultrasonic wave is considered to be a homogeneous strain field and assuming that the localized moments can follow this strain field, then the anomalous elastic constant change,  $\Delta C_{ab}$ , can be expressed in an elegant form (Bates et al., 1988):-

$$\Delta C_{ab} = - \sum_{ijkl} B_{aij} T_{ijkl} B_{bkl} \quad (6.12)$$

Here,  $B_{aij}$  and  $B_{bkl}$  are single crystal magnetoelastic coupling tensors whose elements, as with the elastic constant tensors,  $C_{ab}$ , are governed by the crystal symmetry. The tensor  $T_{ijkl}$  is the magnetic tensor, having the same symmetry properties as the elastic constant tensor, but whose elements are governed by the magnetic symmetry alone. As usual, the indices  $i, j, k$  and  $l$ , run through the Cartesian elements  $x, y, z$  used to define the crystal symmetry axes; the indices  $a$  and  $b$  represent the reduced tensor notation. The occurrence of any elastic constant anomalies are, then, implicit within the relationship between the magnetic symmetry and the underlying crystal symmetry, with the magnitude of the effect governed by the magnitude of the tensor elements.

For the hexagonal crystal symmetry, the allowed elements of the magnetoelastic coupling tensor are:  $B_{11} = B_{22}$ ,  $B_{12} = B_{21}$ ,  $B_{13} = B_{31} = B_{23} = B_{32}$ ,  $B_{33}$ ,  $B_{44} = B_{55}$  and  $B_{66} = \frac{1}{2}(B_{11} - B_{12})$ . We may write down an expression for the

change in  $C_{33}$  from (6.12) for a single domain which we call the primary domain:-

$$-\Delta C_{33} = 4(B_{33}T_{33}B_{33} + 2B_{13}(T_{13} + T_{23})B_{33} + B_{13}(T_{11} + T_{22} + 2T_{12})B_{13}) \quad (6.13)$$

Let us now evaluate the coupling for the three main magnetic phases of Gd<sub>72</sub>Sc<sub>28</sub>. In the basal plane helix phase, which is incommensurate, the symmetry is cylindrical. Therefore  $T_{11} = T_{22}$ . However, due to the planar orientation, all magnetic matrix terms involving an index 3 will be zero. Therefore  $T_{33} = T_{13} = T_{23} = 0$ . Hence:-

$$-\Delta C_{33} = 8B_{13}(T_{11} + T_{12})B_{13} \quad (\text{basal plane helix}) \quad (6.14)$$

The other chirality helical domain will generate the same element. On forming the conical helix we establish the full cylindrical symmetry and inherit the additional terms  $T_{33}$ ,  $T_{13}$  and  $T_{23} = T_{13}$ . So,

$$-\Delta C_{33} = 4(B_{33}T_{33}B_{33} + 4B_{13}T_{13}B_{33} + 2B_{13}(T_{11} + T_{12})B_{13}) \quad (\text{conical helix}) \quad (6.15)$$

In a similar manner, for a c-axis ferromagnet we obtain

$$-\Delta C_{33} = 4B_{33}T_{33}B_{33} \quad (\text{c-axis ferromagnet}) \quad (6.16)$$

In anticipation of a canted ferromagnetic phase, which in fact is present in the Gd<sub>76.7</sub>Sc<sub>23.3</sub> sample, the situation is more complex. Each of the six possible domains is monoclinic with respect to the hexagonal basis. However when all the domains are taken together (as an average) we return to full hexagonal symmetry, so the expression is the same as (6.13).

It is thus straightforward to interpret the  $C_{33}$  behaviour in terms of the presence or absence of symmetry elements in the appropriate expression for  $\Delta C_{33}$  in each phase. It is also possible, knowing the magnetic structure, to make predictions about the behaviour of  $C_{33}$ , but far more difficult to try to

deduce a magnetic structure from a measurement of  $C_{33}$ . In general, the lower the symmetry, the more coupling terms are acquired and the softer  $C_{33}$  becomes. In principle, we may perform similar calculations for  $C_{44}$ , or indeed any other elastic constant. However, the  $C_{44}$  or  $C_{11}$  elastic constants measured in the Gd-Sc alloys were found to exhibit very weak anomalies, making a similar analysis very difficult.

#### $C_{44}$ dependence

The temperature dependence of the  $C_{44}$  elastic constant of Gd<sub>72</sub>Sc<sub>28</sub> is shown in figure 6.2b. It can be seen that there is very little response from  $C_{44}$  at the initial ordering temperature and this may be attributed to the volume nature of the critical interaction at the disorder-order transition; it precludes any large anomalous behaviour for shear waves unless the linear magnetoelastic coupling at the transition is large. This is because for volume magnetostrictive coupling, the change in length of the vector connecting the two spin sites is first order in strain for longitudinal waves, whereas it is only second order in strain for a shear wave (Laramour, 1989).

At the helix/cone transition there is a noticeable change in gradient and also at the cone/c-axis ferromagnetic transition. There is no apparent anomaly at the low temperature ferromagnetic transition. The smallness of these effects and their blurred nature mean they are of limited use as an aid to understanding the magnetic behaviour of the alloy.

#### $C_{11}$ dependence

Figure 6.2c presents the temperature dependence of the  $C_{11}$  elastic constant. There is a change in gradient at the Néel temperature, but like  $C_{44}$  it is weak, and the local variation of points gives some indication of the difficulty with which these measurements were made. By about 120 K the echoes become extremely difficult to overlap due to weak signals, and an erratic behaviour of

Figure 6.2a  $C_{33}$  vs. Temperature for Gd72Sc28

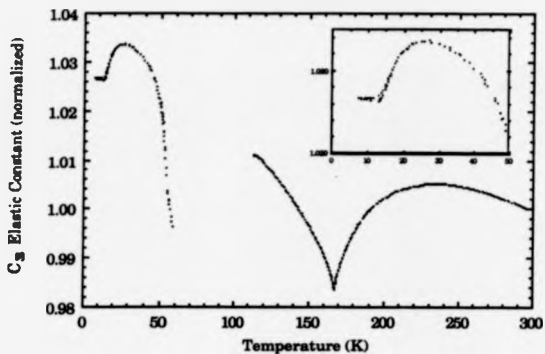


Figure 6.2b  $C_{44}$  vs. Temperature for Gd72Sc28

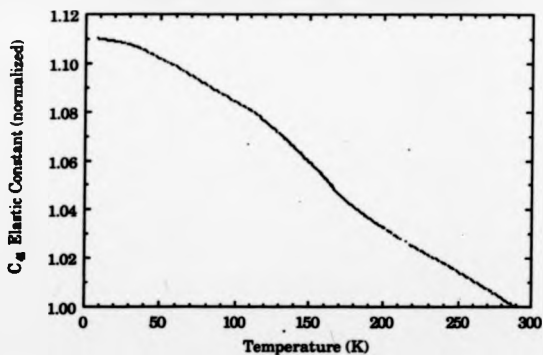
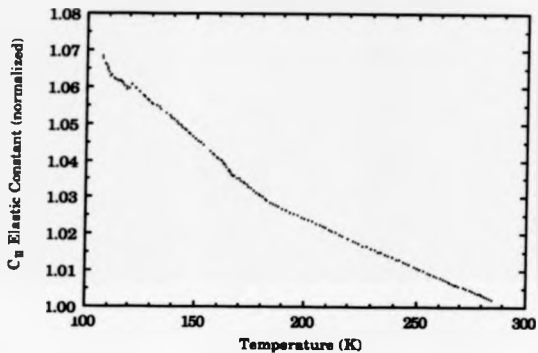




Figure 6.2c  $C_n$  vs. Temperature for Gd72Sc28



points occurs. However the general form of the curve can be seen; there is a very linear response in the paramagnetic regime, and a slight upward change in slope at  $T_N$ .

The low temperature phase in  $Gd_{73}Sc_{27}$  ( $T_N \approx 27$  K)

Below 27 K, the  $C_{33}$  elastic constant begins to drop as if a new magnetic phase is about to be entered. An enlarged view of the low temperature behaviour is provided as an inset to figure 6.2a where it may be seen that  $C_{33}$  flattens out at about 14 K and some hysteresis is apparent between 8 K and 14 K. In the neutron experiment, it was most surprising to observe antiferromagnetic satellites at 14 K and 15 K, but unfortunately the low temperature limit of the diffractometer did not allow us to make further studies at lower temperatures. (See chapter 5 for a fuller discussion.)

**6.4.2  $Gd_{64}Sc_{36}$ ,  $Gd_{65}Sc_{35}$ ,  $Gd_{66}Sc_{34}$  and  $Gd_{70.5}Sc_{29.5}$**

These four samples are all treated together, since they exhibited similar magnetic behaviour. They all ordered initially into the simple basal plane helical phase and this is reflected in their elastic constant behaviour which is shown in figures 6.3, 6.4, 6.5 and 6.6 respectively. For the purpose of clarity, only the cooling curves are presented in these figures, since no hysteretic effects were observed in any ultrasonic measurements on these four samples.  $Gd_{64}Sc_{36}$  is a little different to the other three in that it only has one magnetically ordered phase. The other three order into a conical helix phase at low temperature.

The elastic constant behaviour of these samples is seen to be very similar to that of  $Gd_{73}Sc_{27}$  which has already been discussed. The initial dip in  $C_{33}$  is the usual 2 magnon-1 phonon critical coupling and the sharp recovery is consistent with the basal plane helix structure due to the presence of a single

Figure 6.3a  $C_{33}$  vs. Temperature for Gd64Sc36

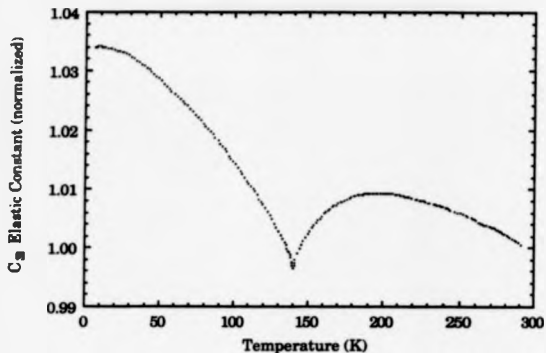


Figure 6.3b  $C_{44}$  vs. Temperature for Gd64Sc36

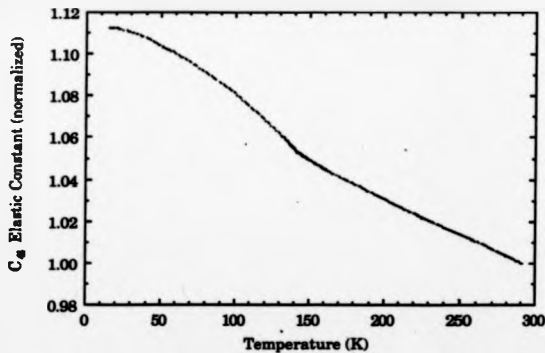


Figure 6.4a  $C_{33}$  vs. Temperature for Gd68Sc32

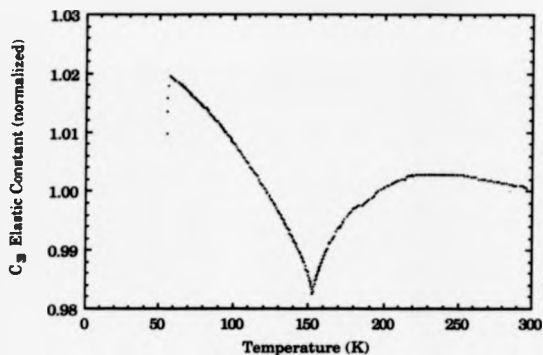


Figure 6.4b  $C_{44}$  vs. Temperature for Gd68Sc32

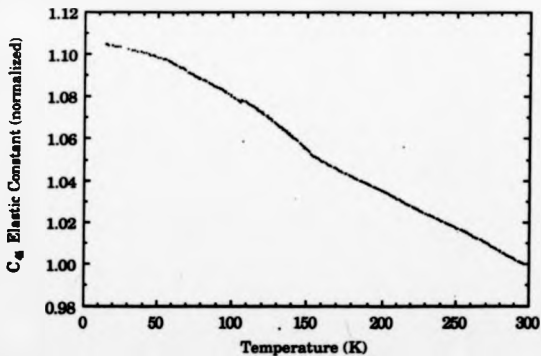


Figure 6.5  $C_M$  vs. Temperature for Gd69Sc31

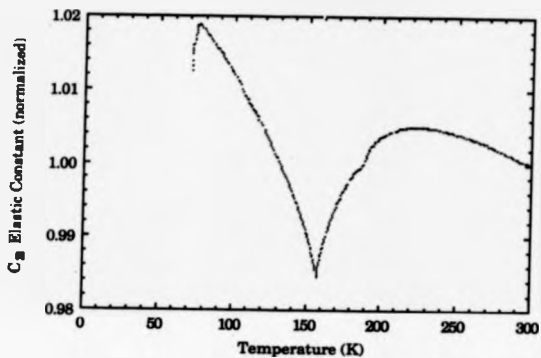
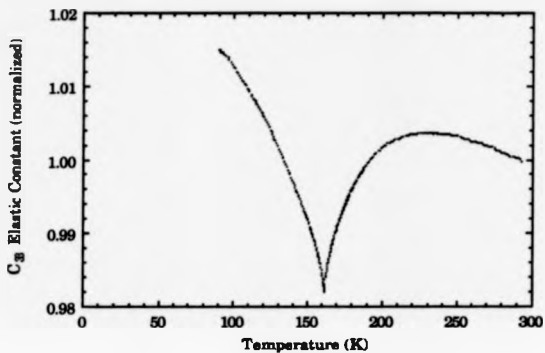


Figure 6.6  $C_{33}$  vs. Temperature for Gd70.5Sc29.5



coupling term in the magnetoelastic interaction (6.14). At the onset of the conical helix phase, there is very high attenuation of the  $C_{33}$  ultrasound accompanied by a large lattice softening effect which may be explained, as for  $Gd_{75}Sc_{25}$ , in terms of additional coupling terms (6.15) and domain wall effects. For the  $Gd_{68}Sc_{32}$  and  $Gd_{69}Sc_{31}$  samples, a small 'kink' may be observed in  $C_{33}$  at about 185 K. Such a feature was not observed on warming in either sample, nor was it observed in  $Gd_{68}Sc_{32}$  in subsequent runs and should therefore be regarded as a spurious effect. A small discontinuity in  $C_{44}$  at 107 K in  $Gd_{68}Sc_{32}$  should likewise be ignored.

By contrast with  $C_{33}$ , the  $C_{44}$  elastic constants of the four samples are little affected by the changes occurring in magnetic structure. At  $T_N$ , there is a departure from the very linear paramagnetic behaviour towards a slight hardening of  $C_{44}$ . Similarly, at the helix/cone transition there is a slight discontinuity in the slope, this time in the opposite sense such that the low temperature value of  $C_{44}$  is very close to its extrapolated value from the paramagnetic régime.

#### 6.4.3 $Gd_{78}Sc_{22}$

Elastic constant measurements of the  $Gd_{78}Sc_{22}$  sample are presented in figure 6.7, where it is soon apparent from  $C_{33}$  (fig. 6.7a) that ferromagnetism is the dominant phase in this sample. The conical helix phase now occurs in a narrow temperature range between 143 K and 172 K. Of perhaps most interest is the initial phase in this sample which exists between 172 K and 178 K. The initial ordering, which takes place at 178 K according to the ultrasound, was missed at first by the neutron diffraction experiment, thereby placing some doubt on the ultrasound measurements. However, the initial ordering temperature, as measured by ultrasound, was in accord with the curve formed by the initial ordering temperatures of the other samples when

plotted against the sample composition (figure 8.1), thus confirming the ultrasound data. On closer examination neutron diffraction enabled the measurement of a small rise in the 100 peak intensity indicating the existence of a *c*-axis or canted ferromagnet (no satellites were observed until 172 K).

The behaviour of the  $C_{33}$  elastic constant is rather unusual in the initial phase in that there is a sharp drop at the ordering temperature followed by a flat region before the alloy orders into a conical helix. Figure 6.7b shows a more careful study of  $C_{33}$  in that region, where it can be seen that on warming, the curve is faithfully reproduced with no hysteresis.

The question now arises as to the magnetic structure between 179 K and 172 K, since on their own, the neutron diffraction results are inconclusive. The apparent absence of any modulation in the structure is consistent with the possibility of a ferro-I phase. Indeed, as we have seen, the softening of  $C_{33}$  is indicative of a canted structure which is consistent with the virtual crystal model of the ferro-I phase where the moments are distributed randomly on the surface of a cone centered on the *c*-axis (Bates, 1986). Furthermore, the initial softening, which is not as severe as in the conical helix phase may also be understood: in the ferro-I phase, the basal plane components of the moments, though effectively paramagnetic still have some magnetic short-range order, so that the coupling terms involving  $T_{13}$  and  $(T_{11} + T_{12})$  in (6.15) are a fraction of what they are when there is long-range order in the basal plane i.e. they only attain their maximum when full long range order has been established in the conical phase. Therefore, we may conclude that although the virtual crystal approximation of the ferro-I phase is not altogether soundly based (Bates, 1987), the  $C_{33}$  ultrasound data does support the existence of ferro-I, when interpretations are based on that model.

$C_{33}$  is well-behaved in the conical and ferromagnetic phases. Between 25 K and 35 K there is a spin reorientation transition where the moments moves away from the *c*-axis with a resulting  $C_{33}$  softening. A small amount of



Figure 6.7a  $C_{33}$  vs. Temperature for Gd75Sc25

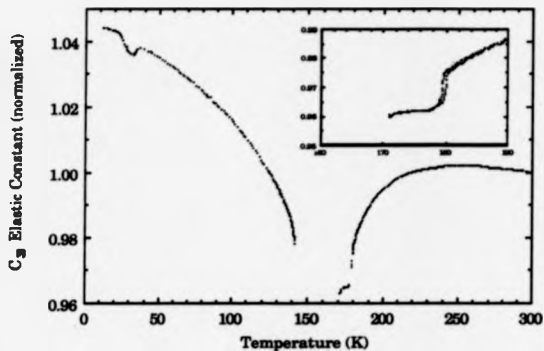
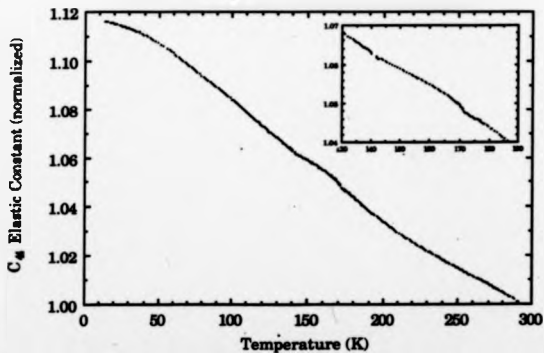


Figure 6.7b  $C_{44}$  vs. Temperature for Gd75Sc25



hysteresis has been observed in this region, which is almost certainly due to domain wall movement as the moments reorient.

The behaviour of  $C_{44}$  is shown in figure 6.7c. It is similar to that in the Gd<sub>73</sub>Sc<sub>25</sub> sample, except that the conical helix phase is a little more pronounced. There is no anomaly shown for the transition at 178 K, however there is a small, abrupt anomaly (fig. 6.7d) at the onset of the conical phase. This may be interpreted as further evidence for a ferro-I phase, since below 178 K there is no effective basal plane magnetization with which the ultrasound can interact, however when the conical phase is entered the ordering of moments in the basal plane allows a coupling term of the type  $T_{44}$ .

#### 6.4.4 Gd<sub>75.7</sub>Sc<sub>23.3</sub>

Figure 6.8 shows the temperature dependence of the  $C_{33}$  and  $C_{44}$  elastic constants for Gd<sub>75.7</sub>Sc<sub>23.3</sub>. From neutron diffraction, we know that this sample only orders ferromagnetically, i.e. no magnetic satellites were observed at any temperatures between 300 K and 12 K. The  $C_{33}$  data (fig. 6.8a) shows the initial ordering to take place at 187 K, and once more we see that there is strange behaviour just below this temperature; at first glance the transition appears to be simply broad, however on closer inspection (see inset) there is clearly a sharp drop in  $C_{33}$  followed by a tiny flat region before it recovers from the 2 magnon critical softening. This is very similar behaviour to the Gd<sub>75</sub>Sc<sub>25</sub> sample, except that there a cone structure ensued, while this sample goes on to behave like a normal ferromagnet. For the same reasons discussed in section 6.4.3, we may attribute such behaviour to the presence of a ferro-I type phase, though it is clear that the phase is far less extensive, existing over a temperature range of only 3-4 K.

Figure 6.8b shows a characteristic  $\lambda$  type anomaly at the initial ordering temperature. In contrast to the ultrasonic velocity (6.11), the critical absorption for ultrasound can be expressed in the form (Luthi, 1970):

$$\alpha = \frac{\omega^2 \chi^{1/2}}{1/\tau_c} \quad (6.17)$$

where  $\omega$  is the ultrasonic frequency,  $\chi$  the spin susceptibility and  $\tau_c$  is the characteristic decay time of the fluctuations. The critical absorption is thus strongly dependent on the type of magnetic order onsetting and the ultrasonic frequency used (see section 6.4.4).

Below about 80 K,  $C_{33}$  begins to soften as the magnetic moments turn away from the c-axis. There is a very high attenuation at this spin-reorientation transition which is clear from figure 6.8b as well as 6.8a. As the ferromagnetic moments near the basal plane,  $C_{33}$  hardens again and tends toward an unperturbed value.

The behaviour of  $C_{44}$ , shown in figure 6.8c, shows very little coupling to the phase transitions. At  $T_c$ , there is merely a weak deviation away from the highly linear paramagnetic regime, with no strong local anomaly. At the spin-reorientation transition, there is a weak coupling of the single ion magnetostrictive type, which results in a dip at approximately 48 K.  $C_{11}$  was measured for this sample and the results are shown in figure 6.9d. A similar characteristic is seen at the initial ordering temperature to the Gd<sub>72</sub>Sc<sub>28</sub> sample. The measurement is rather 'cleaner' than for Gd<sub>72</sub>Sc<sub>28</sub> due to the higher ordering temperature.

Finally, a recent publication (Takashi et al., 1987) on a single crystal of identical composition has reported two magnetic transitions at 178 K and 126 K, with the initial ordering temperature at 187 K. Here, it is simply remarked that neither of the reported transitions have been observed, in

Figure 6.8a  $C_{33}$  vs. Temperature for Gd76.78Sc23.3

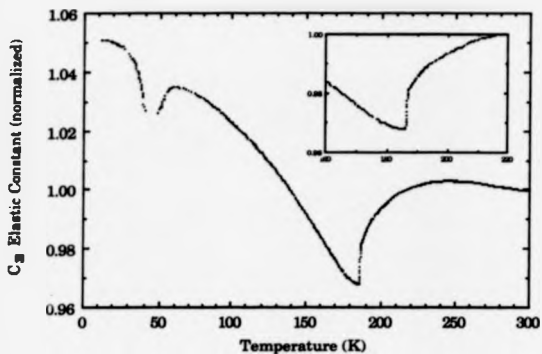


Figure 6.8b  $C_{33}$  Attenuation for Gd76.78Sc23.3

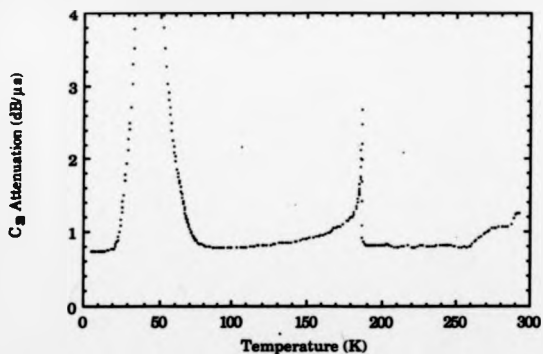


Figure 6.8c  $C_{44}$  vs. Temperature for Gd76.78Sc23.3

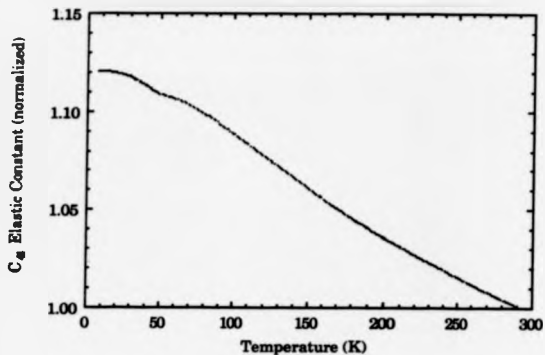
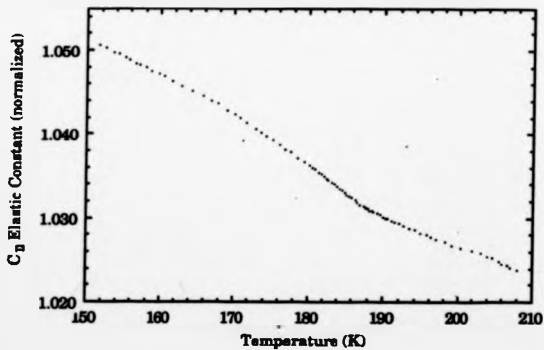


Figure 6.8d  $C_{11}$  vs. Temperature for Gd76.78Sc23.3



measurement of  $C_{33}$  or its associated attenuation,  $\alpha_{33}$  (fig. 6.8b). This is discussed in greater detail in section 8.2.3.

### **8.5 Summary**

In summary, we have seen how ultrasonic measurements of elastic constants can be particularly useful for accurate measurement of magnetic transition temperatures, and that we may understand the different behaviour of the elastic constants in terms of the particular magnetic symmetry being exhibited. Due to the difficulty experienced in measuring  $C_{11}$ ,  $C_{33}$  has proved to be the most informative elastic constant for the Gd-Sc alloys because of its many coupling terms, with  $C_{44}$  remaining relatively little affected by the transitions.

## 7

## Resistivity, Magnetization and Applied Field Studies

**Introduction**

This chapter is divided into three sections. In the first, measurements of resistivity on three of the Gd-Sc alloys ( $Gd_{64}Sc_{36}$ ,  $Gd_{72}Sc_{28}$  and  $Gd_{75}Sc_{25}$ ) are presented. The behaviour of this physical property is interpreted in the light of the neutron diffraction studies and also provides useful additional information on the magnetic phases and phase transitions. The second section is devoted to measurements of magnetization on  $Gd_{72}Sc_{28}$  and  $Gd_{76.7}Sc_{23.3}$ . The final section takes a look at the applied field-temperature (H-T) phase diagram of  $Gd_{64}Sc_{36}$  as investigated by transport property measurements and also the ultrasonic technique of the previous chapter. It should be stressed that this was an initial study of  $Gd_{64}Sc_{36}$  in an applied field, intended to highlight the main characteristics of the system in anticipation of a future neutron diffraction experiment on the alloy. As such, it is rather open-ended, with the emphasis being placed upon simple indications from the results viz. possible magnetic structures, critical fields etc.

The magnetization measurements presented in this chapter were performed at the CNRS, Grenoble, in collaboration with Dr. B. Barbara. The transport property measurements were carried out in Porto, Portugal, by Prof. J.B. Sousa and his group as part of a continuing collaboration on Gd-Y alloys.

### 7.1 Resistivity in $Gd_0.8Sc_{0.2}$ , $Gd_{0.77}Sc_{0.23}$ and $Gd_{0.75}Sc_{0.25}$

The resistivity of the rare-earths is strongly dependent on the magnetic order present, since the exchange coupling between the spin of a conduction electron and the  $4f$  moment of an ion directly affects the electron scattering. In addition, the usual electron-phonon scattering is present ( $\rho_{ph}$ ), as well as the impurity resistivity contribution ( $\rho_0$ ). One then writes

$$\rho(T) = \rho_0 + \rho_{ph}(T) + \rho_m(T),$$

where  $\rho_m(T)$  is the resistivity due to the magnetic contribution.

In the paramagnetic region, sufficiently above the critical temperature, the spin disorder is maximum and independent of temperature. Generally, a linear decrease of  $\rho$  with temperature is observed in this region, due to the corresponding decrease of phonons ( $\rho_{ph} \propto T$  when  $T \gg \Theta$ , the Debye temperature).

As  $T$  approaches the critical temperature, short-range order gradually sets in, increasing pronouncedly in the vicinity of the transition point. This originates interesting critical features in the electrical resistivity ( $\rho$ ), which experimentally can be better displayed through the temperature derivative,  $d\rho/dT$ .

Normally, in a ferromagnet the increase of magnetic order (leading to long-range order characterised by  $q=0$ ) reduces the magnetic scattering and  $\rho(T)$  shows a small decrease as the temperature approaches  $T_c$ . The derivative  $d\rho/dT$  then exhibits a sharp rise through positive values, sometimes accompanied by a peak at the critical temperature. These effects appear as fairly small anomalies in  $\rho$ , because the spin fluctuations occur near  $q=0$ , giving therefore a small change in the electron wavevector  $\mathbf{k} \rightarrow \mathbf{k} + \mathbf{q}$ .

For antiferromagnetic or helical systems, the fluctuations occur near the modulation wavevector characteristic of the magnetic structure,  $q \neq 0$ .



Sizeable effects are now expected in  $\rho$  as  $T$  approaches the Néel temperature, due to the critical spin fluctuations: the onset of the helical (or antiferromagnetic) structure introduces a new special periodicity in the electron hamiltonian leading to new gaps in the electron band structure. The magnitude of these band structure distortions increases as the magnetic order increases. If the magnetic gaps occur near the Fermi level, they may reduce the effective number of free conduction electrons, which favours the increase of  $\rho$  as  $T \rightarrow T_N$ . In most cases this is the dominant effect and then  $d\rho/dT$  exhibits pronounced negative values with a deep minimum at the Néel Temperature.

To interpret the experimental results on basal plane helimagnetic structures, one must also take into account anisotropic effects related to the electron band structure and scattering effects. In fact, for the basal plane resistivity the electrons propagate in planes where the spins are aligned parallel, as in a 2D ferromagnetic structure. One should then observe in phase the characteristic temperature behaviour of a ferromagnet. On the other hand if the conduction electrons propagate along the  $c$ -axis, they are directly influenced by the corresponding magnetic modulation wavevector ( $q$  parallel to the  $c$ -axis), exhibiting the characteristic behaviour of an antiferromagnet.

So far, we have considered only order-disorder transitions. However, interesting order-order phenomena occur in Gd-8c alloys, associated with spin-reorientation transitions below  $T_N$ . In short, the magnetic resistivity is dependent on the canting angle,  $\theta$ , between the spontaneous magnetization and the  $c$ -axis, i.e.  $\rho_{\parallel} = \rho_{\parallel}(T, \theta)$ . Near a spin-reorientation transition,  $\theta$  usually exhibits characteristic anomalies, either with a discontinuous change (first order transition) or through a critical singularity in  $d\theta/dT$  (continuous transition).

The measurements were carried out using the four-contact technique on needle shaped samples of approximately 10mm in length by  $1\text{mm}^2$  cross-section. The samples had been cut from the same boules from which the bulk

samples for neutron scattering and ultrasound were derived. Finally, it should be pointed out that due to the high resolution of the resistivity measurements, the critical features can be sharply displayed through the temperature derivative  $dp/dT$ . This enables the accurate determination of the magnetic critical temperatures and of the associated critical exponents. It is in this form that the results are mainly presented.

### 7.1.1 $Gd_{90}Sc_{10}$

In figure 7.1 is shown  $dp_c/dT$  (where  $p_c$  is the c-axis electrical resistivity). The curve exhibits a sharp minimum at the Néel temperature,  $T_N = 140$  K, where the basal plane helix onsets. Important fluctuation effects extend to temperatures well above  $T_N$ , and close inspection of the data reveals a change in the critical behaviour at temperatures close to  $T_N$ . A weak anomaly, unobserved in both ultrasonic and neutron studies, is apparent at approximately 70 K. A corresponding anomaly can be seen at the same temperature in the corresponding basal plane measurement,  $dp_a/dT$  (figure 7.2). Notice the difference between  $dp_a/dT$  and  $dp_c/dT$  near the paramagnetic/helix transition.

### 7.1.2 $Gd_{72}Sc_{28}$

In the  $Gd_{72}Sc_{28}$  alloy, a sharp minimum is observed in  $dp_c/dT$  at  $T_N = 167$  K (figure 7.3). In the paramagnetic phase close to  $T_N$  an upward curvature develops in  $dp_c/dT$ , similar to earlier observations in Gd-Y alloys (Sousa et al., 1985) where the effect is attributed to the critical enhancement of short-range c-axis order. As  $T$  approaches  $T_N$  a sudden crossover is observed in  $dp_c/dT$ , attributed to short-range basal plane order leading to the onset of the helical

Figure 7.1  $d\rho/dT$  (c-axis) vs. T for Gd64Sc36

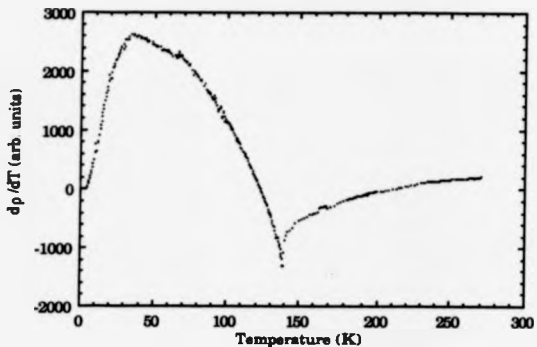


Figure 7.2  $d\rho/dT$  (a-axis) vs. T for Gd64Sc36

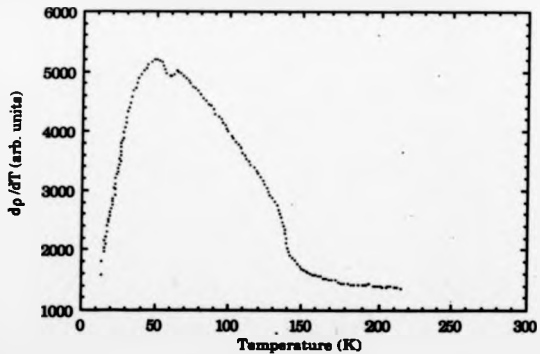


Figure 7.3  $d\rho/dT$  (c-axis) vs. T for Gd72Sc28

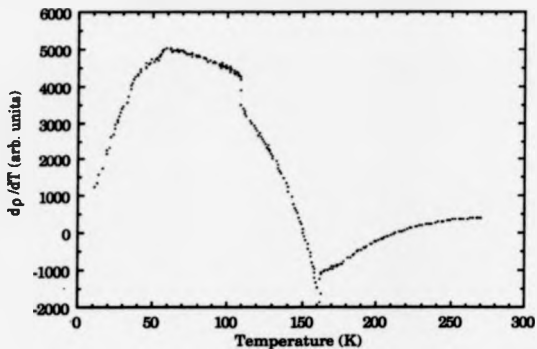
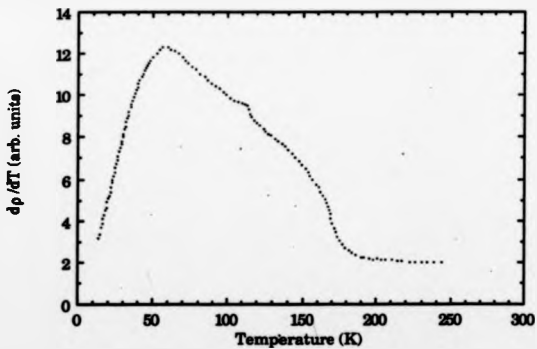


Figure 7.4  $d\rho/dT$  (a-axis) vs. T for Gd72Sc28



structure at  $T_N$ . This crossover occurs so close to  $T_N$  that the transition looks almost first-order.

From the neutron experiment, it is known that the simple basal plane helix phase extends down to 113 K in this sample, below which there is a conical helix phase. At the transition, a small step anomaly is observed in  $dp_c/dT$  (with  $\rho_c$  itself being continuous), indicating a second-order transition. The sudden increase in  $dp_c/dT$  just below 113 K is attributed to the onset of a c-axis ferromagnetic moment, which decreases  $\rho_c$ , producing therefore a higher  $dp_c/dT$  value. The helix finally disappears at about 60 K where a canted ferromagnetic structure develops with a strongly temperature dependent canting angle. This transition is again associated with a small step in  $dp_c/dT$ , but in the opposite sense to that observed at the helix/cone transition. The step can be explained if it is recalled that the helical turn angle,  $\omega$ , gives a positive contribution to  $dp_c/dT$  through  $d\omega/dT$ . As  $d\omega/dT > 0$  just above 60 K and  $d\omega/dT$  vanishes in the low temperature phase, a corresponding negative step in  $dp_c/dT$  should be observed.

Figure 7.4 depicts the  $dp_c/dT$  behaviour for the  $Gd_{72}Sc_{28}$  alloy. The three magnetically ordered phases are clearly delineated.

### 7.1.3 $Gd_{75}Sc_{25}$

For this alloy,  $dp_c/dT$  is shown in figure 7.5. Four magnetically ordered phases are clearly visible, in particular the initially ordered phase which proved to be so elusive in the neutron investigations. The initial steep region in the curve at 178 K corresponds to ordering of a c-axis moment, and the subsequent sharp fall at 170 K is consistent with an ordering in the basal plane to form the conical magnetic structure. Therefore the measurements are very supportive of the existence of a ferro-I type phase, and that this phase is the initial ordered phase in this alloy. Figure 7.6 shows the temperature derivative

Figure 7.5  $d\rho/dT$  (a-axis) vs.  $T$  for Gd75Sc25

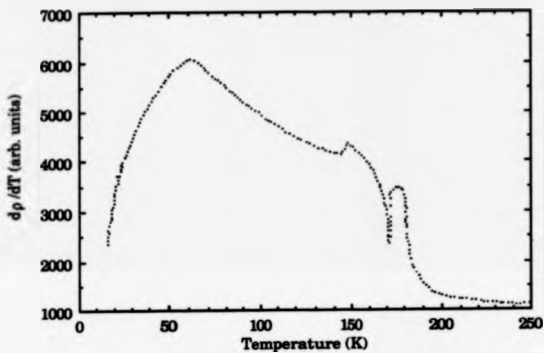


Figure 7.6a  $d\rho/dT$  (c-axis) vs.  $T$  for Gd75Sc25

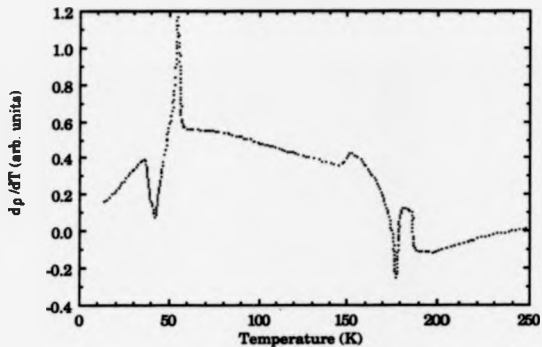


Figure 7.6b  $d\rho/dT$  (c-axis) vs.  $T$  for Gd75Sc25  
in an applied field  $H=0.33$  T

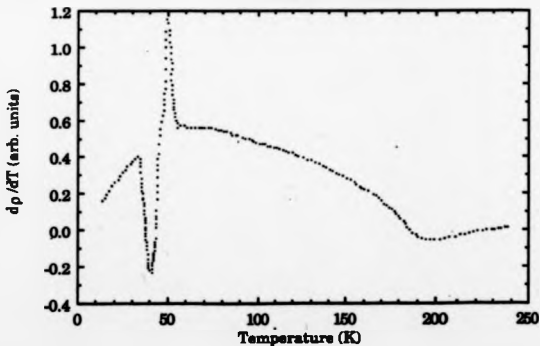
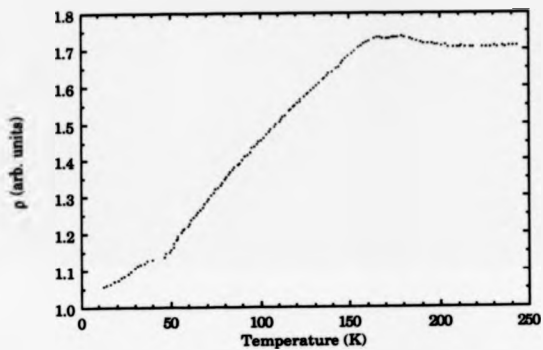


Figure 7.7  $\rho$  (c-axis) vs. T for Gd75Sc25





of the c-axis electrical resistivity in zero applied field and also for an applied field along the c-axis of 0.33 T. For  $H=0$ ,  $d\rho/dT$  delineates five different ordered magnetic phases. As  $T$  decreases, these are ferro-I (178.2–170.1 K), conical helix (170.1–142.7 K), c-axis ferro (142.7–54.9 K), an intermediate canted ferromagnetic phase I (54.9–34.4 K) and canted ferromagnetic phase II ( $T < 34.4$  K). Also,  $\rho_c(T)$  is presented for this alloy in figure 7.7, with the transition temperatures marked (as obtained from  $d\rho/dT$  data).

### 7.2 Magnetization Measurements on $Gd_{73}Sc_{25}$ and $Gd_{78.7}Sc_{21.3}$

Isothermal magnetization measurements were performed primarily in order to check the saturation magnetization in the  $Gd_{73}Sc_{25}$  and  $Gd_{78.7}Sc_{21.3}$  samples, and to check that the spontaneous magnetization in each phase was well behaved upon applying small fields. Measurements parallel to the c-axis and in a basal plane direction were made to monitor the behaviour of the corresponding components of the magnetization. They were carried out on an axial extraction magnetometer in the Laboratoire Louis Néel, CNRS, Grenoble. The applied field was produced by a superconducting Nb-Ti magnet.

#### 7.2.1 $Gd_{73}Sc_{25}$

The b- and c-axis isothermal magnetization curves for  $Gd_{73}Sc_{25}$  are presented in figures 7.8 and 7.9 respectively. The applied field has in all instances been taken close to saturating values. At high fields, the magnetization is seen to be almost equal for basal plane and c-axis measurements at the same temperature. It is usual to extrapolate the linear high field region to zero field to extract the spontaneous magnetization. This has been done for the 10 K c-axis curve to obtain a saturation magnetic moment of  $7.1\mu_B$  (see Appendix B). This represents a minimum saturation

Figure 7.8 b-axis Magnetization for  
Gd72Sc28

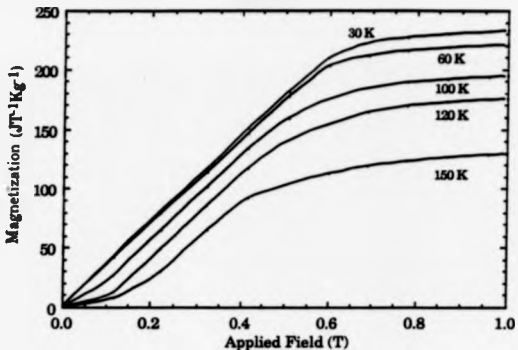
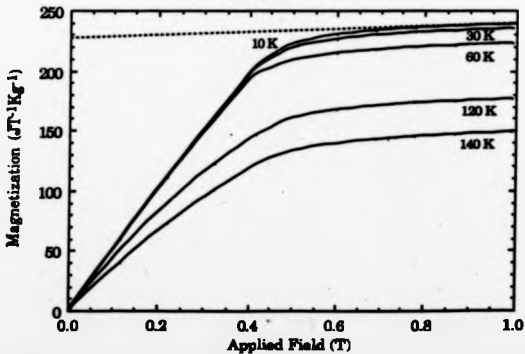


Figure 7.9 c-axis Magnetization for  
Gd72Sc28



magnetic moment, as there is a lack of any obvious linear region at high fields. The value of  $7.1\mu_B$  per Gd ion is not an unreasonable value for a lower limit, and is in keeping with the saturation moment measured by neutrons.

In figure 7.8 the critical behaviour for the collapse of the helix is readily apparent from the 150 K and 120 K curves. It is relatively straightforward to extract the effective critical applied field from the data, but more difficult to evaluate the critical internal field  $H_c$  beyond which the spiral moments collapse about the applied field direction, particularly since the sample shape was far from ideal for magnetic field measurements. (Samples which are of non-ellipsoidal shape will magnetize non-uniformly, leading to a smearing of the transition at  $H_c$ .) The demagnetizing factor, necessary to convert applied field to internal field, can be extracted from the data (in the same way that is generally done for a ferromagnet) by forcing the criticality line between the helical and subsequent phase to be vertical. In simple terms, the slope of the criticality line is the direct reciprocal of the demagnetizing factor. Alternatively, a value for the factor may be made by approximating the sample shape to an ellipsoid with similar axial ratios. Using the sample dimensions listed in table 1.1 together with the graphical method of Osborn (1945), the demagnetizing factor for the sample b-axis was found to be

$$N_b/4\pi = 0.332.$$

Directly from the data (fig. 7.8),

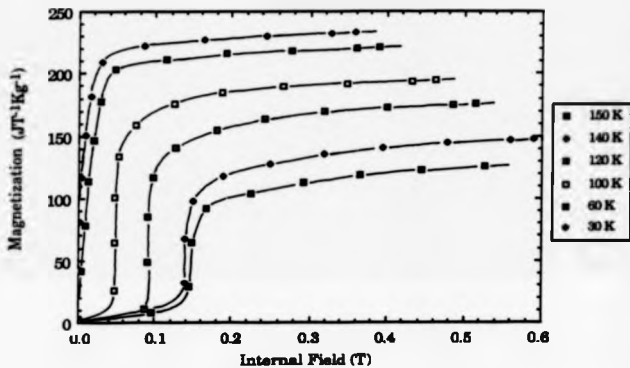
$$N_b/4\pi = 0.24.$$

The internal fields for the sample along the b-axis could then be calculated from the equation:-

$$H_i = (H_a)_i - N_i M_i, \quad (i = a, b, c)$$

where  $N_i$  is the demagnetizing factor,  $H_a$  is the applied field and  $M_i$  is the magnetization in  $JT^{-1}Kg^{-1}$ . The resulting curves, plotted as a function of  $H_i$  using the value  $N_b/4\pi = 0.24$ , are shown in figure 7.10. The verticality of the

Figure 7.10 b-axis Magnetization vs.  
Internal Field for Gd72Sc28



lines at  $H_c$  are a measure of the suitability of the demagnetizing factor; a positive slope indicates too low a factor, a negative slope too high a factor. The demagnetizing factor calculated by Osborn's method was found to be too large, however, the curves obtained for  $N_b/4\pi = 0.24$  are near-perfect.  $H_c$  at 120 K for example is observed to be 0.09T.

Examining figure 7.10, one can see that the highest three temperatures correspond to helical phases, whereas the 30 K line corresponds to a ferromagnetic phase, since it is vertical at zero field. The 60 K line is on the border between a spiral and a ferromagnetic phase, having a near zero value for  $H_c$ . These results are in good agreement with the magnetic phases as determined from neutron diffraction.

Returning to figure 7.9, the magnetization curves show normal ferromagnetic behaviour, and indicate that at 120 K and 140 K the c-axis is a hard direction, whereas below 60 K it is an easy direction. This is also in agreement with the neutron studies, from which we know the magnetic moments lie in the basal plane above 120 K (basal plane helix structure) and lie along the c-axis below 60 K (c-axis ferromagnetic structure). The c-axis demagnetizing factor was measured to be  $N_c/4\pi = 0.33$  from the slope of the low-temperature curves.

### 7.2.1 $Gd_{78.78}Ce_{21.22}$

The b- and c-axis magnetization curves for  $Gd_{78.78}Ce_{21.22}$  at temperatures of 10 K, 60 K, 100 K and 150 K are presented in figures 7.11 and 7.12 respectively. Both of these sets of measurements display normal ferromagnetic behaviour at all temperatures. At high fields, close to saturation, the magnetization is once more observed to be the same for both basal plane and c-axis measurements, reflecting the point to point accuracy of the data. A similar analysis to the one given in the previous section for the extraction of a

Figure 7.11 b-axis Magnetization for  
Gd76.7Sc23.3

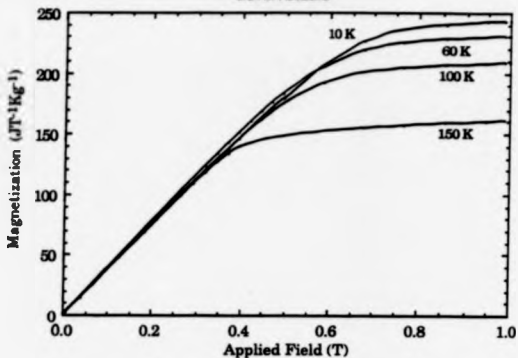
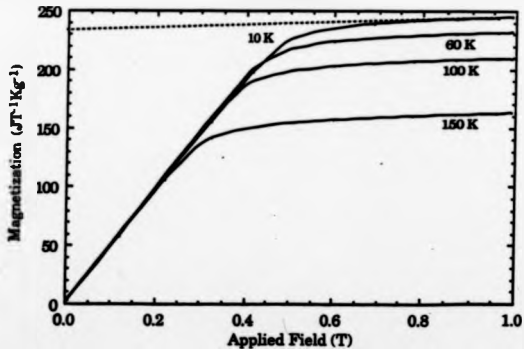


Figure 7.12 c-axis Magnetization for  
Gd76.7Sc23.3



saturation magnetization, again using c-axis magnetization at 10 K led to an identical value for a lower limit to the saturation moment per Gd ion,  $7.1\mu_B$ . The demagnetizing factors for this sample obtained from the magnetization gradient were found to be

$$N_y/4\pi = 0.26,$$

$$N_z/4\pi = 0.32.$$

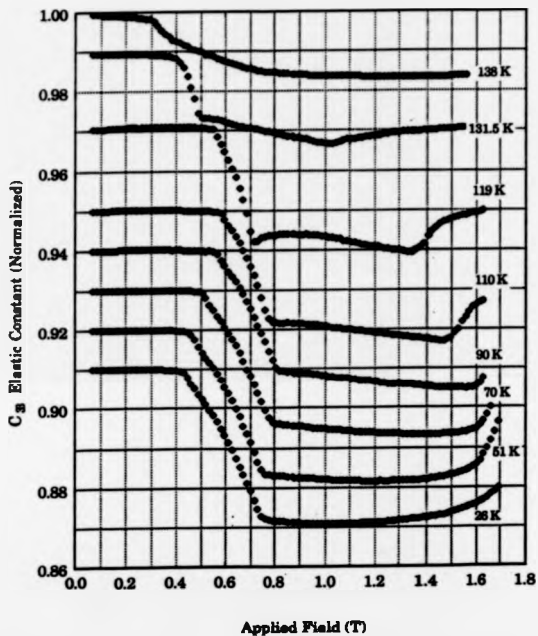
### 7.3 Ultrasonic Study of H-T Phase Diagram of $Gd_{40}Sc_{60}$

The following measurements were carried out with the same technique as explained in chapter 6, with the additional variable of a magnetic field applied in the basal plane of the alloy. The magnetic field was provided by an electromagnet whose field could be varied between 0.007 T (the remanent field) and 1.7 T.

#### 7.3.1 $Gd_{40}Sc_{60}$ : Isothermal Measurements of $C_{33}$ in an Applied Magnetic Field

Figure 7.13 shows isothermal measurements of  $C_{33}$  for a variety of temperatures below  $T_N$  in an applied magnetic field. Each graph has been displaced along the  $C_{33}$  axis for clarity. Each of the graphs show an initial linear region at low fields; this is surprising since it is generally believed (e.g. Cooper, 1972) that in small applied fields, there is a slight distortion of the helix with the moment vectors being tipped slightly in the applied field direction, and one would expect the variation of the magnetoelastic coupling parameters (section 6.4.1) to manifest themselves as a change in the elastic constant. Excepting the 138 K curve, there then reaches a critical field where the elastic constant falls fairly sharply. This region of the curve exists for 0.1 to 0.3T and represents the transition from a distorted helix to a fan type phase.

Figure 7.13  $C_{33}$  Elastic Constant vs. Applied Field for Gd648c36 (graphs are displaced along the vertical axis)





This is a phase where the magnetic moments undergo cyclic oscillations about the field direction, with the  $q$  vector of modulation still along the  $c$ -axis. This transition, which has been investigated by many authors (e.g. Enz, 1961; Nagamiya et al., 1962; Herpin and Maréchal, 1969) is understood to be a first order transition due to a sudden collapse of the spiral structure about the applied field direction. The reason for the gradual transition as observed in these measurements is once more because of demagnetizing effects of the sample shape.

There then follows a nearly flat response in  $C_{33}$ , indicating the completion of the transition to the fan structure. At still higher magnetic fields,  $C_{33}$  starts to harden as the fan structure becomes ferromagnetic via a continuous magnetic transition. This transition unfortunately takes place at fields near the limit of the electromagnet, but is clearly visible at 119 K and 110 K. Once more, demagnetizing effects tend to 'smear' the transition. This is particularly marked at low temperature, where there is merely an upward turn of the curve with no pronounced anomaly.

At 138 K the transition to fan structure is observed at 0.3T, however there appears to be no transition to ferromagnetism at high fields. This may be explained by realizing that the phase boundaries at this temperature are almost parallel to  $H$  in the  $H$ - $T$  phase diagram. Such a situation will lend itself to broad transitions, with the result that the transition to fan structure is not complete before the transition to ferromagnetism commences.

It is not possible to correct these measurements for the demagnetizing factor, since the sample magnetization must be known. Instead, uncorrected critical fields have been extracted to plot out the  $H$ - $T$  phase diagram of  $Gd_{44}Sc_{56}$ . The transition to fan structure has been taken as the first anomaly (the fall in  $C_{33}$ ) being determined by the intersection of extrapolations of the linear regions close to and on either side of the anomaly. The same method was used to determine the transition to ferromagnetism, but was harder to

implement particularly below 110 K. The transition points have been plotted in H-T space to construct the phase diagram in figure 7.14a.

### 7.3.2 $Gd_{50}Bi_{50}$ : Infield Measurements of $C_{33}$

These measurements were made by applying the magnetic field in the basal plane and keeping its magnitude at some chosen value while the temperature was varied. Figures 7.15 to 7.18 show the results for fields of 0.463T, 0.542T, 0.8T and 1.57T. The results may be interpreted in the light of the isothermal results presented in the previous section.

Let us consider firstly figure 7.15. As the temperature is lowered, the convex curvature towards  $T_N$  is the 2-magnon 1-phonon magnetoelastic coupling described in the previous chapter. At 140 K, there is a change of slope and a second downward turn which persists for about 10 K; this is the fan phase. At 130 K, there is a severe hardening of  $C_{33}$  as the distorted helix phase is entered. At lower temperature, the alloy begins to re-enter the fan phase as  $C_{33}$  softens. The completion of that transition may only be determined by carrying out measurements on warming, where a noticeable hysteresis takes place in this region. Within each integral phase, no hysteresis is observed. This measurement is therefore consistent with the isothermal measurements and transition points have been added to the phase diagram (fig. 7.14a) accordingly.

The results at 0.542T (fig. 7.16) show similar features. This time, however, the initial fan phase is a little more extensive, existing for about 15 K below  $T_N$ . Also, the region of hysteresis where the sample consists of fan phase regions and distorted helix regions is considerably broader. At 0.8T (fig. 7.17),  $C_{33}$  behaves quite differently. Just below  $T_N$  there is a very slight change in the slope of the curve and a few degrees below  $T_N$  there is a region of hysteresis. The phase just below  $T_N$  is believed to be the fan phase, but it remains only for

Figure 7.14a H-T Phase Diagram for Gd<sub>64</sub>Sc<sub>36</sub>  
constructed from Elastic Constant  
Measurements

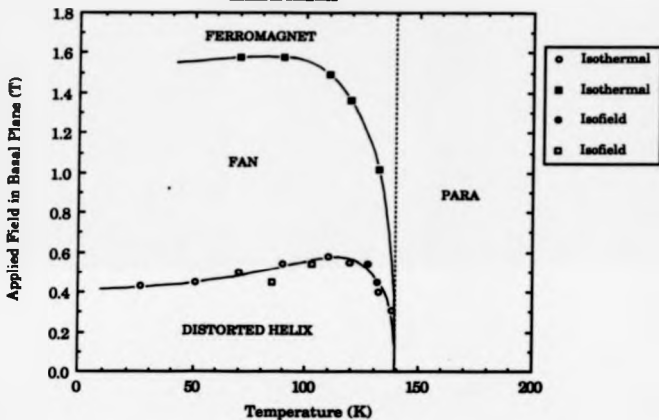


Figure 7.14b H-T Phase Diagram for Gd64Sc36  
constructed from Magnetoresistance  
Measurements

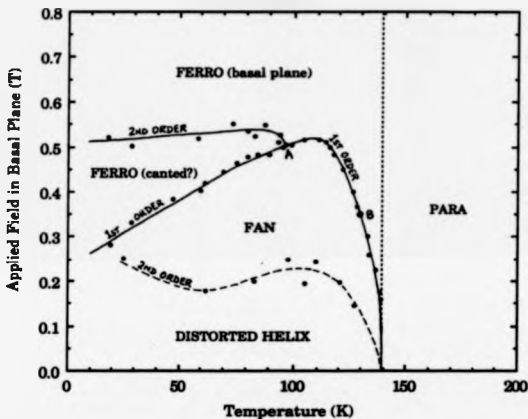


Figure 7.15 C33 vs. Temperature with  
 $H=0.453$  T for Gd64Sc36

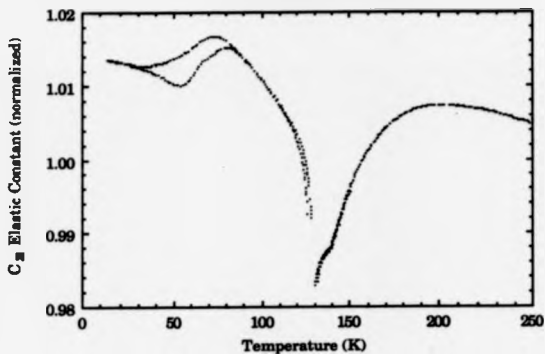


Figure 7.16 C33 vs. Temperature with  
 $H=0.542$  T for Gd64Sc36

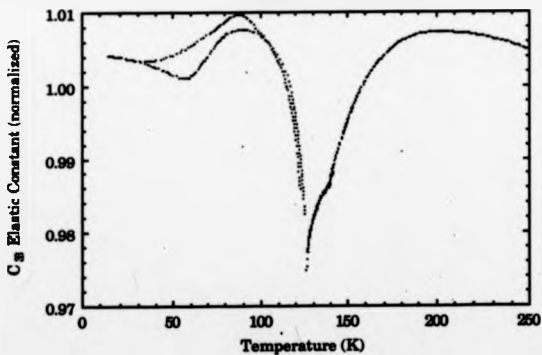


Figure 7.17 C33 vs. Temperature with  
 $H=0.8$  T for Gd64Sc36

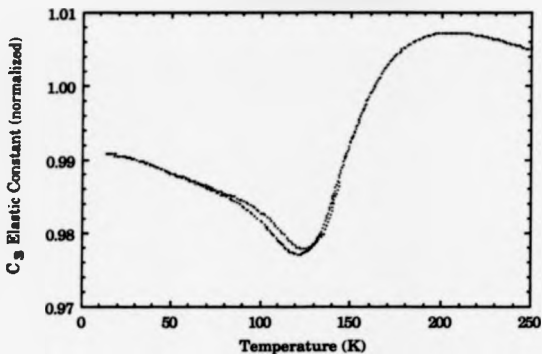
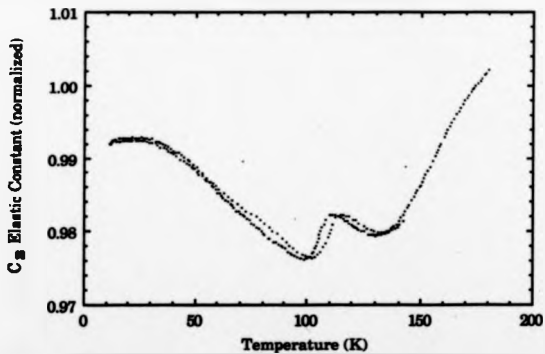


Figure 7.18 C33 vs. Temperature with  
 $H=1.57$  T for Gd64Sc36



a few Kelvins due to the nucleation of some helical phase: although this may not seem consistent with the phase diagram, it should be recalled that the helix/fan transition assumes a 'width', which from the isothermal measurements is seen to exist up to 0.8T. The smallness of the hysteresis is consistent with the fact that the fan phase is always dominant, and at 70 K the sample become completely ordered in the fan structure once more.

At 1.57T (fig. 7.18), some small hysteresis is observable at all temperatures below  $T_N$ . Also, significant variations in  $C_{33}$  are apparent above 100 K. These features are difficult to explain by ultrasonic measurements alone, but may arise, in part, to the fan/ferromagnetic phase boundary which is in proximity at such high fields.

Transition temperatures determined from the isofield measurements of  $C_{33}$  are also plotted in the phase diagram of figure 7.14a.

### 7.3.3 Magnetoresistance Measurements

The H-T phase diagram of  $Gd_{48}Sc_{52}$  has also been determined by magnetoresistance measurements by Prof. J.B. Sousa and his co-workers, and is presented in figure 7.14b for comparison. It should be noted that these studies, performed on a needle shaped sample (b parallel to the long axis), will suffer very little from demagnetizing effects and the applied field is thus very close to the internal field parameter. The critical fields consequently appear at lower values than those in figure 7.14a. The phase diagram is broadly similar to the one measured by elastic constant, but provides more detail, particularly concerning a new phase between the basal plane ferromagnetic and fan phase (possibly canted ferromagnetic) not observed in the elastic constant measurements. This leads to an interesting multicritical point A where ferromagnetic, fan and canted ferromagnetic phases coexist.

Transport property studies are very often definitive regarding the nature of a transition, and the phase boundaries are marked accordingly. The transition from distorted helix to fan structure is reported, in contradiction with general belief, to be continuous. Also, there is a bicritical point B where there is a change from first order to second order behaviour along the fan to ferromagnetic phase transition. This phenomenon seems to be supported by the 138 K and 131.5 K elastic constant measurements presented in figure 7.13

#### 7.4 Summary

In summary, the resistivity measurements on these three alloys have provided useful complementary results to the ultrasound and neutron diffraction studies. They are sensitive to the magnetic phase transitions exhibited by the samples, and have been of invaluable use regarding the initial ordered phase in  $\text{Gd}_{72}\text{Sc}_{28}$ , where they represent the most conclusive evidence that this is a ferro-I phase, hitherto only previously observed in the Gd-Y alloys. The c-axis electrical resistivity has also shown evidence of a transition at 34 K which has not been observed in either the ultrasound or neutron diffraction studies. The significance of this transition is so far unresolved.

The magnetization measurements on  $\text{Gd}_{72}\text{Sc}_{28}$  and  $\text{Gd}_{76.7}\text{Sc}_{23.3}$  have been interpreted in terms of their magnetic phases as determined by neutron diffraction and found to exhibit normal behaviour. Both samples were found to have a saturation magnetization of  $\sim 7.1\mu_B$  per Gd ion. The magnetization measurements have allowed the demagnetizing factors of the samples to be determined parallel to the b and c directions.

A tentative H-T phase diagram has been constructed following isothermal and isofield measurements of the  $C_{33}$  elastic constant in  $\text{Gd}_{64}\text{Sc}_{36}$ . Below the Néel temperature, the measurements have indicated two transitions as the applied field is increased. The first is from a distorted basal plane



helical structure at low fields to a fan phase structure where the moment vectors are modulated about the applied field direction. This transition is normally understood as being a first order transition, although the nature of the transition has not been determined by these measurements. The second transition takes place at higher applied fields, where the moments are finally forced into a ferromagnetic structure with the vectors parallel to the field (basal plane ferromagnet). This is usually a second order transition, but again these studies preclude drawing such conclusions.

The phase diagram measured by magnetoresistance measurements provides much extra detail, especially with regard to the nature of the magnetic phase transitions. An additional phase (probably canted ferromagnetic) is also observed, unseen by the elastic constant measurements. These magnetic structures may only be determined unequivocally by neutron diffraction studies in an applied field.

## 8

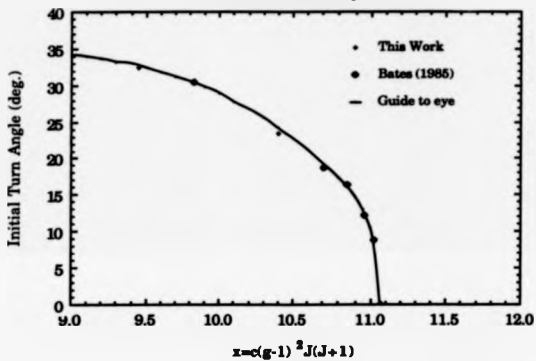
## Discussion and Conclusions

## 8.1 Gd-Y

The magnetic behaviour of two single-crystal samples of composition  $\text{Gd}_{66}\text{Y}_{34}$  and  $\text{Gd}_{60}\text{Y}_{40}$  has been studied in some detail throughout their full magnetically ordered temperature ranges, with particular attention being placed on the helix/ferro-II transition. This transition is observed at 151 K for  $\text{Gd}_{66}\text{Y}_{34}$ , but remains incomplete at the lowest temperatures studied (12 K) for  $\text{Gd}_{60}\text{Y}_{40}$ , where there is evidence for the co-existence of short-range helical and ferromagnetic order in a possibly 'frozen-in' state. The magnetic phases of these samples as determined by neutron diffraction are consistent with the most recent phase diagram (Bates et al., 1986). Both alloys order initially into a simple basal plane helical phase, where the onsetting inter-layer turn angle is in agreement with previous measurements (figure 8.1) and where the turn angle decreases continuously as the temperature is lowered.

$\text{Gd}_{66}\text{Y}_{34}$  exhibits two ordered phases; a basal plane helix which is the high temperature ordered phase ( $T_N = 208$  K) and a canted ferromagnetic phase, ferro-II ( $T_C = 151$  K). For  $\text{Gd}_{66}\text{Y}_{34}$ , the inter-layer turn angle has been observed to fall smoothly to zero in the helical phase (similarly to other Gd-Y alloys exhibiting this phase transition). As previously reported, this is accompanied by an increase in the satellite widths as the transition is approached (Bates, 1985), and may be explained by the fact that the domain

Figure 8.1 Initial Turn Angles vs. De Gennes factor for Gd-Y Alloys



wall thicknesses diverge rapidly as the turn angle approaches zero, thus destroying the long-range helimagnetic order (Drillat, 1983).

The determination of inter-layer turn angles in the low  $q$  helical structures near the ferro-II phase has been of special interest, since observation of the smooth convergence of  $q$  all the way to zero is direct evidence of a continuous phase transition. Such a transition is quite unusual, if not unique, between two magnetically ordered phases. A new approach to fitting peaks to the diffraction profile has allowed turn angles to be measured with values less than would normally be possible due to the limiting resolution. Measured turn angles of much less than  $1^\circ$  per layer together with a continuous approach to a value of zero at the ferro-II phase strongly support earlier conjecture. Further corroborative evidence has recently been supplied by a differential thermal analysis (DTA) study of the helix/ferro-II phase transition in Gd-Y alloys between  $\text{Gd}_{66}\text{Y}_{34}$  and  $\text{Gd}_{70}\text{Y}_{30}$ , carried out by Dr. R.P. Pinto and her colleagues in Porto, Portugal (Pinto et al., 1987). It has been found that the helix/ferro-II transition is second order for  $\text{Y} > 31\%$ ; however, for  $\text{Gd}_{70}\text{Y}_{30}$  (just in the vicinity of the multicritical point adjoining ferro-I, ferro-II, and helical phases), DTA measurements indicate a change to a first-order transition. The latent heat at the first-order transition is fairly small ( $L < 8 \text{ J.Mol}^{-1}$ ), as consistent with the exceedingly weak magnetic anisotropy in Gd-Y alloys. This evidence suggests that the tricritical point A (fig. 4.1) is not strictly speaking a Lifshitz point, even if the basal plane behaviour in the vicinity of the point is considered separately from the  $c$ -axis behaviour (Bates, 1987), since the requirement that  $q \rightarrow 0$  at the point will not be satisfied. The resemblance to a 2D Lifshitz point is nonetheless close.

The neutron measurements have shown that the ferro-II phase does not immediately achieve long-range order below the transition, but does so progressively over some 7 K. This is observed to coincide with the stabilization of the canting angle, which remains approximately constant between  $60^\circ$  and  $70^\circ$

down to 15 K. On warming, long-range ordered ferromagnetism is observed right up to  $T_c$ , indicating that once long-range ferromagnetic order is achieved, it is stable on warming.

Gd<sub>60</sub>Y<sub>40</sub> orders initially into a helical phase at 188 K which persists to low temperatures where the behaviour of the antiferromagnetic satellites has suggested an approach to the ferro-II phase. However the alloy does not achieve long-range order in the ferromagnetic phase, but appears instead to reach a 'frozen-in' state of mixed ferromagnetism and antiferromagnetism.

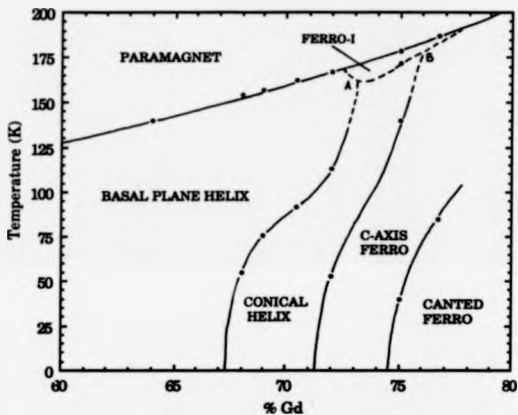
Neutron diffraction experiments on Gd<sub>60</sub>Y<sub>40</sub> have been made to elucidate the nature of the loss of long-range helimagnetic order at low temperatures, where the antiferromagnetic satellites are seen to broaden severely. This striking phenomenon, initially believed to be a manifestation of random field effects, may be accounted for in terms of the characteristics of the helix/ferro-II transition, especially the steepness of the phase line and its proximity at the alloy composition. The Lorentzian squared lineshape of diffraction peaks broadened by random field effects was not found, however the severity of the broadening makes it difficult to reject these effects entirely.

Observations of a similar kind have been found in alloys of Gd<sub>62.4</sub>Y<sub>37.6</sub> and Gd<sub>68.9</sub>Y<sub>31.1</sub> (Bates, 1985). In Gd<sub>62.4</sub>Y<sub>37.6</sub>, long-range ferromagnetic order was never achieved in the observable temperature range (72–50 K), while in Gd<sub>68.9</sub>Y<sub>31.1</sub>, the sample achieved long-range order some 20 K below the proposed ferromagnetic ordering temperature. Gd<sub>66</sub>Y<sub>34</sub> studied in this work has also exhibited this type of behaviour. In addition, the lack of long-range ferromagnetic order just below the phase transition, coupled with the thermal hysteresis arising from domain nucleation, gives rise to the appearance of broad transitions and a slow development of the ferromagnetic phase (Legvold et al., 1980; Blackie, 1981). Such behaviour substantiates the proposition that the low temperature effects in Gd<sub>60</sub>Y<sub>40</sub> are inherent from the characteristics of the helix/ferro-II phase line.

A most interesting feature of the helix/ferro-II transition is the fact that at the transition, two distinct processes take place: on the one hand the  $q$ -vector characterizing the helical structure tends toward zero as the line is approached from the helical side. On the other hand, as the transition line is crossed into the ferromagnetic phase, the magnetic moment develops a component along the  $c$ -axis. There is, in fact, no *a priori* reason why these changes should occur simultaneously along the same line. Indeed, in simple models which are consistent with the hexagonal symmetry assumed for these alloys, this line would split into two lines: one associated with the vanishing  $q$ , and the other with the onset of the rotation of the local moment out of the basal plane. Another interesting feature of the phase diagram is that while in the helimagnetic phase the moments seem to lie in the basal plane, both ferromagnetic phases have non-vanishing  $z$  components of the magnetization,  $S_z$ .

Dr. D. Mukamel has proposed recently (Mukamel, 1981, 1989) that these features of the phase diagram can be accounted for if one assumes that the Gd-Y alloys possess a 3-fold rather than 6-fold symmetry. In particular, the commensurate-incommensurate transition associated with the vanishing of the  $q$ -vector would then be accompanied by a non-zero component of the magnetization in the ferromagnetic phase, as found experimentally. In the helical phase for a system with 3-fold symmetry, the order parameter does not induce a modulated  $z$  component  $S_{z,q}$  with the same wavevector as that of the basal plane magnetization  $S_{xy,q}$ . However, it is concluded that higher harmonics, such as  $S_{z,3q}$  should be induced. These predictions should be checked experimentally in the extensive helical phases of the already well-characterized  $Gd_{95}Y_{34}$  and  $Gd_{95}Y_{22}$  alloys.

Figure 8.2 Partial Magnetic Phase Diagram  
for Gd-Sc Alloys



## 8.2 Gd-Sc

### 8.2.1 Magnetic Properties of the System

The magnetic phase diagram of the Gd-Sc alloys in the temperature-concentration plane for zero applied field is given in figure 8.2. The phase diagram has been constructed from the neutron diffraction and ultrasonic studies of this work alone, since it has been found that there exist discrepancies between this phase diagram and the magnetic transition temperatures of alloys studied in earlier work (e.g. Child and Cable, 1969). Since the only previous neutron study was performed some 20 years ago using powder samples, the purity of the alloys was probably not as high as those used here, and there is therefore reason to believe that the magnetic phase diagram in figure 8.2 is the most correct to date.

The initial ordering transition for all the alloys displays characteristics typical of an order/disorder transition, with ultrasonic velocity measurements sensitive to the effects of short-range order on the volume magnetoelastic coupling well into the paramagnetic phase. This is manifested as a concave dip in the bulk elastic constants. Alloys with up to 72% Gd order initially into a basal plane helical phase characterized by an immediate hardening of the  $C_{33}$  elastic constant, forming the distinctive shape of an inverted cusp as a function of temperature. In the neutron studies, the phase is typified by the appearance of antiferromagnetic satellites spaced from the nuclear peak along the reciprocal  $c$ -axis. These satellites satisfy the necessary angular intensity relationships for the basal plane helix structure.

The transition from basal plane helix to cone structure is marked by the appearance of magnetic diffracted intensity centred at reciprocal lattice points (excluding those of the 001 type). This is accompanied by a change of slope of the interlayer turn angle as a function of temperature. However, the transition is apparently continuous, involving the rotation of the moments out of the basal



plane. The cone phase has a dramatic effect on the  $C_{33}$  elastic constant, which falls very sharply as the phase is entered and the attenuation of the propagating ultrasound is also severe. This may be explained by the additional magnetoelastic coupling terms inherited as a consequence of symmetry breaking at the transition, and also by the damping of the elastic waves by domain wall movement.

As the temperature is lowered through the conical phase, the canting angle decreases steadily. For alloys with between 71 and 76% Gd, there is a further transition to c-axis ferromagnetism, which takes place as the canting angle reaches zero. The two alloys studied which exhibit this transition show differing behaviour with regard to the turn angle: Gd<sub>75</sub>Sc<sub>25</sub> shows a steady decrease of the turn angle as the temperature is lowered until the canting angle reaches zero, where the turn angle remains finite at 14.7°. For Gd<sub>75</sub>Sc<sub>25</sub>, the turn angle makes a downward turn toward zero some 6 K above the transition and is falling rapidly at the last measured point before the transition. This is unusual, because the canting angle and the turn angle are normally dependant on different physical mechanisms, and there seems little reason to assume that they should be strongly coupled. However, since the ferromagnetic transition in these alloys may be understood as being caused by higher order terms in the exchange interaction (see section 8.2.5), there may be some coupling. It has been observed, nevertheless, that there may exist changes in the properties of the helix/cone phase line regarding  $q$ .

The c-axis ferromagnetic phase, exhibited by samples with Gd concentration above 71 K, is characterized by the absence of antiferromagnetic satellites and the absence of magnetic diffracted intensity on the 002 reciprocal lattice point. There is also a severe hardening of the  $C_{33}$  elastic constant as the phase is entered. On further cooling, samples with above ~74% Gd also exhibit a spin-reorientation transition, where the moments rotate towards the basal

plane and indeed almost reach the basal plane at low temperatures in  $\text{Gd}_{75}\text{Sc}_{25}$  and  $\text{Gd}_{78.7}\text{Sc}_{21.3}$ .

The measured magnetization curves for the Gd-Sc alloys generally follow the mean-field theoretical curves given in the figures for comparison, with the observed saturation Gd moment varying from  $6.9\mu_B$  to  $7.6\mu_B$ . Moreover, the magnetization curves are generally observed to be slightly high (above the theoretical curve) in the temperature range between  $-0.8T_c$  and  $T_c$  and sometimes fall a little below the theoretical curve below  $-0.8T_c$ . These observations are upheld by earlier measurements on the magnetization of Gd (Elliot et al., 1953, Nigh et al., 1963).

In contrast to the Gd-Y alloy system, it is important to note that with the exception of the region around ferro-I, all the phases exhibited by the alloys studied establish long-range magnetic order, with the diffracted magnetic intensity appearing as peaks with a width determined by the instrumental resolution. This must reflect the high state of equilibrium of the system in its various magnetic phases, with well-defined magnetic phase boundaries which display no apparent hysteresis in either neutron diffraction or ultrasonic measurements.

### 8.2.3 Ferro-I in Gd-Sc

$\text{Gd}_{75}\text{Sc}_{25}$  orders initially at 179 K into a phase which exhibits characteristics of ferro-I, previously only observed in the Gd-Y alloys. The  $C_{33}$  elastic constant remains low for about 7 K after the initial concave drop on approach to the transition. This behaviour was also seen for ferro-I in Gd-Y (Bates, 1985). Resistivity measurements have given supportive evidence of initial ordering of the moments along the c-axis followed by ordering in the basal plane at the transition to the cone structure. The most conclusive evidence for ferro-I from the neutron studies has been the absence of

antiferromagnetic satellites until 7 K below the ordering transition, although the results also strongly suggest ordering along the c-axis at 179 K and subsequent ordering in the basal plane at 172 K. Unfortunately, the limited extent of the phase and the inadequacy of the counting statistics have prevented the obtaining of precise magnetization curves, from which the two-tier nature characteristic of this phase should be seen.

Evidence of ferro-I has also been seen for  $\text{Gd}_{76.7}\text{Sc}_{23.3}$  albeit to a lesser degree than for  $\text{Gd}_{75}\text{Sc}_{25}$ . The  $C_{33}$  elastic constant shows a flattening over about 2 K below the initial ordering temperature before ordering as a c-axis ferromagnet. This feature is not observed for samples which order as helimagnets, and is not expected for samples which order directly into a c-axis ferromagnetic phase (c.f. pure Gd). There is no resistivity data available at present to back up this observation, and neutron diffraction is of little use over such a small temperature range. However, diffuse scattering has been observed around the 002 reflection over a wide temperature range below  $T_c$  corresponding to short-range order in the basal plane. This is particularly apparent just below  $T_c$ . The diffuse scattering is not observed on warming the sample from low temperatures suggesting, as in some Gd-Y alloys, that once long-range order has been established, it is stable. From the limited data available, it therefore seems reasonable to conclude that in the region of the magnetic phase diagram of Gd-Sc corresponding to ferro-I in Gd-Y, the system is exhibiting characteristics of ferro-I-like properties, but with a weaker tendency to stabilize ferro-I, and exemplified by the limited extent of the phase in comparison with the Gd-Y system. This is a surprising conclusion to draw given that the ferro-I phase is believed to result from a short-range exchange interaction, and that the substitution of Sc for Y was expected to stabilize the phase. Clearly a simple model based on competing interactions is not sufficient in accounting for ferro-I, and the details of the band structure distortion on alloying are important.

Unfortunately, the limited extent of the ferro-I region so far observed has meant that problems concerning the nature of this phase still remain. It is not known whether ferro-I is a long-range ordered structure (i.e. random cone), whether it arises from statistically random nearest neighbour interactions, or whether it arises from compositional fluctuations (cluster model).

### 8.2.3 Gd<sub>76.7</sub>Sc<sub>23.3</sub>

Of particular interest regarding Gd<sub>76.7</sub>Sc<sub>23.3</sub> is the recent publication by Ito et al. (1987) concerning the magnetic structure of this alloy. Their sample was cut from the same boule and the properties measured were magnetization, low field susceptibility, electrical resistivity, ultrasonic attenuation and specific heat. The low field ac susceptibility curves for the c-axis exhibited a sharp peak at the highest ordering temperature ( $T_c=187$  K) and a drop between  $T_c$  and  $T_2$  ( $=126$  K), which suggested the existence of an antiphase domain-ferrimagnetic structure. In this structure, several atomic layers have the c-axis components of the moments pointing upward, followed by a nearly equal (but not equal) number of atomic layers having c-axis components pointing downward, with an essentially random basal plane component. The difference in numbers of the atomic layers having the c-axis upward and downward components supposedly increased at  $T_1$  ( $=178$  K), and then below  $T_2$  the structure transformed to a canted ferromagnetic structure with the c-axis moment ordered and random moment components in the basal plane. A similar conclusion was reached from the results of electrical resistivity, elastic property and specific heat measurements.

First of all, the initial ordering temperature of 187 K is supported by the neutron and ultrasonic measurements. However, the transitions reported at  $T_1$  and  $T_2$  have not been observed in this work. The transition reported at  $T_1$  is best seen from the measurements presented for the c-axis electrical resistivity,

and as such may arise from microscopic effects which will not be seen using the macroscopic probes of elastic constant and neutron diffraction.  $T_2$  is a distinct transition apparent from all reported measurements and therefore it is surprising that no anomaly has been observed in the measurement of  $C_{33}$ , if too small an effect to be observed by neutrons.

The antiphase-domain ferrimagnetic structure proposed for  $Gd_{76.7}Sc_{23.3}$  may be interpreted in two ways; the first interpretation is that the domains of up and down pointing c-axis moments occur periodically along the c-axis, though not necessarily being the same size. (This is probably the intended interpretation, since the conclusions are interpreted in the light of Kaino and Kasuya (1981)—see section 8.2.5.) Secondly, the up and down domains may be of varying sizes along the c-axis, with a tendency to form larger domains of one type and with a typical c-axis size which is of the order of several atomic layers.

The results of neutron diffraction cannot assimilate either possibility, since in the first interpretation, the periodic nature of the domains would give rise to antiferromagnetic diffraction peaks, which have not been found despite careful searches across a full Brillouin zone. In the second case, because the domains are uncorrelated, the scattering from each block would be incoherent, and consequently the intensities from each diffracting block would be summed at the reciprocal lattice points. However, the small size of the domains could then be expected to result in a considerable broadening of the ferromagnetic peaks, which has not been observed. (The diffuse scattering seen around the 002 reciprocal lattice point—section 5.6—cannot arise from such a structure.)

Although the magnetic structures of the sample proposed by Ito et al. may be in error, their reported transitions at  $T_1$  and especially  $T_2$  present a problem. The limited resolution of the diffraction experiments means that the transitions could arise from changes in the domain structures of relatively large (i.e. >200 layer) domains. Anything occurring on a smaller scale should

have been observed. The absence of an anomaly in the  $C_{33}$  elastic constant (this work), measured several times, is also puzzling considering that an anomaly has been seen by Ito in the  $C_{33}$  ultrasonic attenuation. The conflict between measurements remains unreconciled for the present.

### 8.2.4 Magnetic Critical Points

Although the phase diagram in the region of the ferro-I phase is not well mapped out, there exists the possibility of two multicritical points (labelled A and B) where the helix/cone and the cone/c-axis ferromagnetic phase boundaries merge with either the ferro-I phase boundary or the paramagnetic phase boundary. It has been proposed (Hornreich, 1980) that the Gd-Sc system could well exhibit a Lifshitz point (a multicritical point where paramagnetic, ferromagnetic and helimagnetic phases coexist with  $q \rightarrow 0$  at  $q=0$ ). Such a point has only previously been observed in MnP (Becerra et al., 1980). The possibility of points A or B being a Lifshitz point is, however, complicated by the presence of the ferro-I phase and therefore seems remote.

### 8.2.5 Gd-Sc Magnetic Phase Diagram - General Overview

Remarkably enough, the single phase transition from helix to canted ferromagnet in the Gd-Y system is split into three separate transitions in the Gd-Sc system, perhaps reflecting the stronger perturbation of Gd by Sc, which exposes the 'degeneracy' of the underlying symmetry of the Gd-Y system. Indeed, the magnetic phase diagram of Gd-Sc may be considered simplified with respect to these three transitions, which replaces a complex helix/ferromagnetic transition which is beset by hysteresis, and which appears very broad due to failure to achieve long-range order in its proximity.

Kaino and Kasuya (1980) have modelled the magnetic properties of heavy rare-earth systems; using a simple band model, they have investigated the role of the non-linear c-f (conduction-f-band) exchange interaction on the magnetic properties of the rare-earth metals. Furthermore, their results are seen to account for the stronger propensity of the Gd-Sc system to develop c-axis order. They find that without the crystal field, the non-linear effect stabilizes the cone structure for small  $k_a$ , the characteristic wave number of the flat Fermi surface (i.e. small parallel sheets of Fermi surface), and thus contributes an effective anisotropy energy along the axis of the helix. The effect of temperature has been included in the model in the form of the magnitude of the ionic moment and the effective lifetime of the conduction electrons,  $\Gamma$ . In lowering the temperature, the model demonstrates that the non-linear effect causes the ferromagnetic transition, while an increase of  $\Gamma$  also stabilizes the ferromagnetic phase against the cone and the helical phases. The inclusion of a crystal field complicates the magnetic phase diagram: in the case of easy plane anisotropy, the fan appeared instead of the cone. For the case of easy axis anisotropy, the helix was squared by the higher harmonics and became the antiphase domain structure in the infinitesimal c-f exchange.

Although the model is too simple to make a detailed numerical comparison with various experimental results in rare-earth metals, qualitative and semi-quantitative comparisons are possible. The model has shown, for example, that an increase in the effective lifetime,  $\Gamma$ , tends to destroy the cone phase and stabilizes the ferromagnetic phase at the expense of the helical phase. This accounts for the absence of antiferromagnetism in Gd, where  $\Gamma$  increases as the temperature is increased from  $T=0$ . Dilution of Gd with Y improves the Fermi surface nesting condition and gives rise to the appearance of a helix/ferromagnetic transition which is predicted to disappear at ~40% Y, in line with experiment (this work).

Placing Gd-Sc on the  $T=0$  phase diagram of Kaino and Kasuya (1980) has not been attempted because of the large uncertainties in  $\Gamma$  and  $k_a$ , which are important. However, the predicted stabilization of the cone phase between ferromagnetic and helical phases for low  $\Gamma$  and  $k_a$  means that the behaviour of Gd-Sc may be at least qualitatively understood in terms of their model.

### 8.3 Future Work

The helimagnetic breakup exhibited by  $\text{Gd}_{60}\text{Y}_{40}$  at low temperature is worth examining in greater detail by studying another sample near to the helix/ferro-II phase boundary at low temperature, perhaps slightly richer in Gd, e.g.  $\text{Gd}_{51}\text{Y}_{49}$ . This would involve carrying out detailed peak-fitting analysis at low temperature, as carried out for  $\text{Gd}_{60}\text{Y}_{40}$ , in order to ascertain the rôle of possible random field effects. Also, the use of Soller collimating slits together with the now operational multidetector on D9 should improve the resolution enough in  $2\theta$  to establish the nature of the breakup in directions other than the  $c$ -axis.

We have recently been allocated time on D9 to investigate the predictions of Dr. Mukamel, who has proposed that features of the phase diagram of Gd-Y may be understood by assuming that the alloys possess a 3-fold symmetry rather than 6-fold (see section 8.1). According to the predictions, modulations of a  $c$ -axis component with wavevector  $3q$  should be induced. Since earlier experiments in the helical phases of Gd-Y did not envisage such a modulation,  $Q$ -scans were never performed far enough out in along  $c^*$  from the reciprocal lattice points to observe resulting peaks, should they exist. The well-characterized alloys  $\text{Gd}_{66}\text{Sc}_{34}$  and  $\text{Gd}_{68}\text{Sc}_{32}$  with their extensive helical phases will be used to test the theory.

The Gd-Sc alloys also present interesting work for the future. Intriguing work lies ahead in the region of the phase diagram between 72% and 75% Gd,



where experimental data is lacking. Indeed, the true extent of the ferro-I region and the positions of the phase boundaries are not known. Also, two multicritical points exist, but their positions are not accurately known. These points may reveal intriguing critical properties in their own right. In this region, however, neutron diffraction will be of limited use, and it is believed only a survey using a variety of experimental techniques will prove informative with regard to characterization of the transitions. A neutron study of the behaviour of the turn angle along the cone/ferromagnetic phase line may also be rewarding, particularly as the multicritical point is approached.

It would also be fascinating to find out the magnetic structure of the low temperature phase which follows on from c-axis ferromagnetism in  $\text{Gd}_{72}\text{Sc}_{28}$  at  $-15\text{ K}$ . There is no provision for working below this temperature at present on D9, but it might be possible in future to mount an ILL orange cryostat on D9 for this purpose.

The D3b instrument at the ILL, which sits on the hot neutron source, has recently proved its suitability for studying magnetic field driven transitions in the Gd alloys. A neutron test experiment on  $\text{Gd}_{64}\text{Sc}_{36}$ , which had been initially investigated in a magnetic field using ultrasound (this work), emphasized the importance of complementary neutron diffraction studies for the determination of the magnetic phase diagram. As an example, it is generally believed (but has never been directly observed) that when a field is applied in the basal plane to a basal plane helix, the helix becomes distorted as the field is increased and then collapses via a first-order transition into a fan phase where the moments oscillate in a periodic fashion about the field direction. This should give rise to many higher-order magnetic satellites. No higher-order satellites were observed in the experiment. In summary, it is believed that induced ferromagnetic domains form out of the chirality domain walls, though this is a tentative explanation which should be backed up with

further experiments. What is certainly clear is that use of D3b opens up a new dimension in the study of the Gd alloys.

The same problems remain concerning interpretation of the ferro-I phase, and the same problems remain in trying to solve them: a study of paramagnetic scattering in ferro-I would be very informative, as would inelastic experiments, but the severe absorption of Gd destroys any possibility of such experiments even at short wavelengths. Isotopically enriched  $^{160}\text{Gd}$ , a low absorbing isotope of Gd would make these experiments possible, but it is very expensive.

Lately, however, there has been a new thrust at the ferro-I problem. At the Paris magnetism conference, ICM88, Ito et al. (1988) reported measurements of the magnetization, electrical resistivity, thermal expansion, specific heat and magnetic anisotropy of a  $\text{Gd}_{75}\text{Y}_{17.5}\text{Sc}_{7.5}$  single crystal alloy where they have observed a ferro-I phase that exists over a temperature range of approximately 30 K from an initial ordering  $T_{c1} = 216$  K to a full moment developed at  $T_{c2} = 188$  K. It would therefore appear that the addition of Sc combined with Y does indeed favour the random nature of ferro-I.

The specific heat measurements of Ito show divergence at both ordering temperatures, so from a mean field point of view, ferro-I must be treated as decoupled from the subsequent magnetic phase. Thus, on changing from ferro-I to the canted ferromagnetic phase below  $T_{c2}$ , there is a cross-over between two decoupled competing types of order. This very idea of cross-over leads to magnetization curves with a two-tier nature as observed for Gd-Y (Bates et al, 1987).

Neutron experiments have been planned to examine ferro-I and the two transitions  $T_{c1}$  and  $T_{c2}$  in this new alloy. The temperature dependence of the magnetization obtained from neutron data of the alloy should allow the study of the loss of ordered moment and indicate whether present understanding may

be enhanced by pursuing the additional replacement of Y with Sc to monitor the increase in disorder.

## Appendix A

### Evaluation of the Extinction Corrections to the Ferromagnetic Reflections

Zachariasen's (1967) correction for secondary extinction is

$$Y_s = (1 + 2x)^{-1/2},$$

where

$$2x = \frac{2T\lambda^3}{V^2 \sin 2\theta} g^* F^2.$$

$g^*$  is the extinction parameter and  $F^2$  is the true structure factor for the reflection ( $F_N^2 + F_M^2$  or  $F_N^2$  or  $F_M^2$  depending on whether we consider a ferromagnetic, nuclear or antiferromagnetic reflection).  $T$  is the mean path length through the sample,  $V$  is the crystal volume and  $\lambda$  and  $\theta$  have their usual meanings.

In Becker and Coppens (1974) extension of the theory,

$$Y_s = (1 + 2x + \text{lesser terms in } x^2)^{-1/2}.$$

Although the lesser terms are important when calculating the absolute values of  $Y_s$ , we can ignore them in calculating the variation of  $Y_s$  for small changes in  $F^2$ , and express  $Y_s$  as

$$Y_s = (1 + k|F|^2)^{-1/2}, \quad (\text{A.1})$$

so that

$$\frac{dY_s}{dF^2} = -\frac{1}{2} Y_s^3 k$$

where  $k$  is a constant for a particular reflection and independent of  $F$ . Thus the extinction correction for a reflection with both nuclear and magnetic contributions can be expressed in terms of the correction for the nuclear reflection alone:-

$$\begin{aligned}
 Y_{M \cdot N} &= Y_N + \frac{dY_N}{dF_M^2} F_M^2 \\
 &= Y_N - \frac{1}{2} Y_N^2 k F_M^2.
 \end{aligned}
 \quad (A.2)$$

From (A.1) we get

$$k = \frac{1/Y_N^2 - 1}{F_N^2}.$$

From (A.2),

$$Y_{M \cdot N} = Y_N \left( 1 - \frac{(1 - Y_N^2)}{2 F_N^2} F_M^2 \right). \quad (A.3)$$

In calculating the magnetization, the formula used is

$$\begin{aligned}
 \frac{F_M^2}{F_N^2} &= \frac{I_{M \cdot N} (1/Y_{M \cdot N}) - I_N (1/Y_N)}{I_N (1/Y_N)} \\
 &= \frac{I_{M \cdot N} \left( \frac{Y_N}{Y_{M \cdot N}} \right) - I_N}{I_N}.
 \end{aligned}$$

From (A.3), we get

$$\frac{F_M^2}{F_N^2} = \frac{I_{M \cdot N} \left\{ 1 - \frac{(1 - Y_N^2)}{2} \frac{F_M^2}{F_N^2} \right\} - I_N}{I_N}. \quad (A.4)$$

Since  $F_M^2 / F_N^2 = (I_{M \cdot N} - I_N) / I_N$ , (A.4) can be solved iteratively. The  $Y_N$  values used were those obtained from the refinements.

To show the effect, the correction factor may be expanded in terms of  $\delta_N$  where  $Y_N = 1 - \delta_N$ :

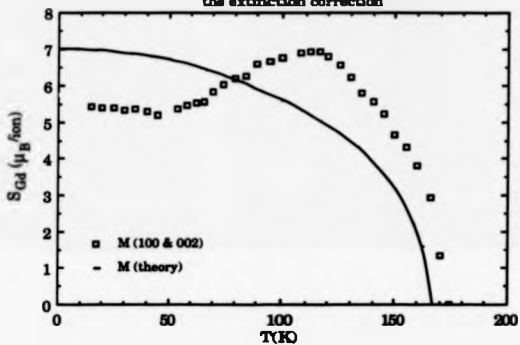
$$1 - Y_N^2 = 1 - (1 - \delta_N)^2 = 2\delta_N,$$

where we ignore the terms in  $\delta_N^2$ .

$$\therefore \frac{F_M^2}{F_N^2} = \frac{I_{M+N} \left(1 - \delta_N \frac{F_M^2}{F_N^2}\right)^{-1} - I_N}{I_N} \quad (\text{A.4})$$

Thus the effect is almost exactly opposite to the effect on antiferromagnetic reflections (see figure A1).

Figure A1 Mean ionic Gd moment vs. T for  
Gd72Sc28 as calculated without  
the extinction correction



## Appendix B

### Calculation of the Gd Ionic Moment from Low-Temperature Isothermal Magnetization Curves

As an example, the calculation is performed for the  $\text{Gd}_{78.7}\text{Sc}_{23.3}$  sample with the observed magnetization obtained from extrapolation of the 10 K c-axis curve (figure 7.12).

$$1 \text{ Mole } \text{Gd}_{78.7}\text{Sc}_{23.3} = 131.1\text{g}$$

$$\text{Sample Mass, } M = 0.6213\text{g}$$

$$\therefore \text{No. Moles} = 4.739 \times 10^{-3}$$

$$\text{No. Formula Units} = \text{No. Moles} \times N_A = 2.854 \times 10^{21}$$

$$\therefore \text{No. Gd Atoms} = 2.189 \times 10^{21}$$

$$\begin{aligned} \text{Observed Magnetization} &= 232 \text{ JT}^{-1}\text{Kg}^{-1} \\ &= 0.1441 \text{ JT}^{-1} \end{aligned}$$

$$\begin{aligned} \therefore \text{Gd Ionic Moment} &= \frac{0.1441}{2.189 \times 10^{21}} \text{ JT}^{-1} \\ &= 7.10 \mu_B \end{aligned}$$



## References

- Allibon J.R., Filbel A., Lehmann M.S., Mason S.A. and Simms P., *J.Appl.Cryst.* **14** 326 (1981)
- Archer J.M. and Lehmann M.S., *J.Appl.Cryst.* **19** 456 (1986)
- Bacon G.E., *Neutron Diffraction* (3rd ed.), Clarendon press, Oxford (1975)
- Baruchel J., Palmer S.B., and Schlenker M., *J. de Physique* **43** 1279 (1981)
- Bates S., Ph.D. Thesis, University of Hull (1985)
- Bates S., Palmer S.B., Sousa J.B., McIntyre G.J., Fort D., Lagvold S., Beaudry B.J. and Koehler W.C., *Phys.Rev.Lett.* **55** 2968 (1985)
- Bates S., McIntyre G.J., Palmer S.B., Sousa J.B., *J.Phys.F* **17** 1973 (1987)
- Bates S., Patterson C., McIntyre G.J., Palmer S.B., Mayer A., Cowley R.A. and Malville R., *J.Phys.C* **21** 4125 (1988)
- Beaudry B.J. and Daane A.H., *Transactions of the Metallurgical Society of AIME* **237** 865 (1963)
- Beaudry B.J. and Daane A.H., *J. Less-Common Metals* **6** 322 (1964)
- Becker P.J. and Coppens P., *Acta Cryst.* **A30** 129 (1974)
- Blackie G.N., Ph.D. Thesis, University of Hull (1981)
- Blackie G.N. and Palmer S.B., *J Phys.C* **15** L483 (1982)
- Blume M., Freeman A.J. and Watson R.E., *J.Chem.Phys.* **37** 1245 (1962)
- Bozorth R.M. and Gambino R.J., *Phys.Rev.* **147** 487 (1966)
- Bozorth R.M., *J.Appl.Phys.* **38** 1366 (1965)
- Braga M.E., Pinto R.P., Sousa J.B., Blackie G.N., Hemslay D.J. and Palmer S.B., *J. Magn. Magn. Mat.* **29** 203 (1982)
- Breit G. and Wigner E., *Phys.Rev.* **49** 519 (1936)
- Bruce A.D. and Cowley R.A., *Structural Phase Transitions*, Taylor and Francis (1981)
- Cable J.W. and Koehler W.C., *J.Appl.Phys.* **53** 1904 (1982)
- Chen C.H., Gibson J.M. and Flemming D.M., *Phys.Rev.* **B26** 185 (1982)
- Child H.R. and Koehler W.C., *Phys.Rev.* **174** 562 (1968)
- Child H.R. and Cable J.W., *J.Appl.Phys.* **40** 1003 (1969)
- Cooper B.R., *Solid State Physics* **21** 393 (1975)
- Cooper B.R. in *Magnetic Properties of Rare Earth Materials*, Editor R.J.Elliot, Plenum Press, London, 1972)
- Coppens P., Leiserowitz L. and Rabinovich D., *Acta Cryst.* **18** 1035 (1965)
- Cowley R.A., Birgeneau B.J., Shirane G. and Yoshizawa H., *Multicritical Phenomena*, R.Fynn and A.Skjeltorp Ed's (Nato ASI B106) Plenum Press (1984)

- Dimmock J.O. and Freeman A.J., *Phys.Rev.Letters* **13** 750 (1964)
- Drillat A., Ph.D. thesis, University of Grenoble.
- Elliot J.F., Legvold S. and Spedding F.H., *Phys.Rev.* **91** 28 (1953)
- Elliot R.J., *Phys.Rev.* **134** 348 (1961)
- Enz U., *J.Appl.Phys.* **S32(J)** 22 (1961)
- Fort D., Personal Communication (1986)
- Fosheim K. and Fossum J.O., *Multicritical Phenomena*, R. Pynn, A. Skjeltorp ed.'s (NATO ASI B) Plenum Press, 1984
- Freeman A.J. in *Magnetic Properties of Rare Earth Materials*, Editor R.J.Elliot, Plenum Press, London (1972)
- Freeman A.J. and Desclaux J.P., *Int.J.Magnetism* **3** 311 (1972)
- Gorodetsky G., Luthi B. and Moran T.J., *Intern. J.Magnetism* **1** 295 (1971)
- Gotase J.A., Rhyne J.J., Wegner L.E. and Mydosh J.A., *ICM Proceedings* (1985)
- Gschneider K.A. and Eyring L.R. (Ed.s), *Handbook on the Physics and Chemistry of Rare Earths* (Vol. 1), North Holland (1978)
- Hellier A.G., Palmer S.B. and Whitehead D.G., *J.Phys.* **E8** 352 (1975)
- Herman F. and Skillman S. in *Atomic Structure Calculations*. Prentice-Hall, Inc., New Jersey (1963)
- Herpin F.A. and Meriel P., *J.Physique* **23** 737 (1969)
- Hornreich R.M., *J.Magn.Magn.Mater.* **15-18** 387 (1980)
- Ito T., Oka M., Legvold S. and Beaudry B.J., *Phys.Rev.B* **29** 6276 (1984)
- Ito T., Takeuchi J., Mizuno K., Ito K., Oka M. and Beaudry B.J., *Jpn.J. Appl.Phys.* **26** L1868 (1987)
- Izyumov Y.A. and Ozerov R.P., *Magnetic Neutron Diffraction*, Plenum Press, New York (1970)
- Kaino K. and Kasuya J., *J.Phys.F* **11** 883 (1981)
- Kasuya T., *Progr.Theoret.Phys.(Japan)* **16** 45 (1956)
- Keeton S.C. and Loucks T.L., *Phys.Rev.* **168** 872 (1968)
- Koehler W.C., *J.Appl.Phys.* **36** 1078 (1965)
- Koehler W.C., in *Magnetic Properties of Rare-earth Metals*, ed.R.J.Elliot, Plenum Press (1972)
- Kuks W.F., *Materials Science Forum* **27-28** 25 (1988)
- Laramour C.E. and Kadanoff L.P., *Phys. Rev.* **187** 619 (1969)
- Legvold S., Harmon B.N., Beaudry B.J., Burgardt P., Younkun D.R. and White H.W., *Phys.Rev.B* **16** 4986 (1977)
- Legvold S., *Phys.Rev.B* **19** 448 (1979)

- Legvold S., in *Ferromagnetic Materials*, Ed. E.P. Wohlfarth, North Holland (1980)
- Legvold S., Burgardt P. and Beaudry B.J., *Phys. Rev. B* **23** 2573 (1980)
- Legvold S., Burgardt P. and Beaudry B.J., *J. Magn. Magn. Mat.* **15-16** 413 (1980)
- Lindgård P.A., *Phys. Rev. B* **16** 2168 (1977)
- Lomer W.M., *Proc. Phys. Soc. (London)* **80** 489 (1962)
- Lovesey S.W., *Theory of Neutron Scattering from Condensed Matter*, Clarendon Press, Oxford (1984)
- Luthi B., Moran T.J. and Pollina R.J., *J. Phys. Chem. Solids* **31** 1741 (1970)
- Mackintosh A.R., *Physics Today* **23** (June 1977)
- McIntyre G.J. and Stanfield R.F.D., *Acta Cryst.* **A44** 257 (1988)
- Majkrak C.J., Cable J.W., Kwo J., McWhan D.B., Yafet Y., Waszcak J.V. and Vettier C., *BNL Report 38016* (1986)
- Marshall W. and Lovesey S.W., *Theory of Thermal Neutron Scattering*, Oxford (1971)
- Michelson S., *Phys. Rev.* **B16** 585 (1985)
- Moon R.M. and Koshler W.C., *Phys. Rev.* **27** 407 (1971)
- Mukamel D., *Phys. Rev. Lett.* **46** 845 (1981)
- Mukamel D. and Barbara B., to be published (1989)
- Musgrave M.J.P., *Crystal Acoustics*, Holden-Day, San Francisco (1970)
- Nagamiya T., Nagata K. and Kitano Y., *Prog. Theor. Phys.* **27** 1253 (1962)
- Nigh H.E., Legvold S. and Spedding F.H., *Phys. Rev.* **132** 1092 (1963)
- Nigh H.E., Legvold S., Spedding F.H. and Beaudry B.J., *J. Chem. Phys.* **41** 3799 (1964)
- Nye J.F., *Physical Properties of Crystals*, O.U.P., (1964)
- Osborn J.A., *Phys. Rev.* **67** 351 (1945)
- Palmer S.B., *J. Phys. F* **5** 2370 (1975)
- Patterson C.P., Ph.D. Thesis, University of Hull (1986)
- Pinto R.P., Braga M.E., Amado M.M. and Sousa J.B., Personal communication (1987)
- Rhys J.J. and McGuire T.R., *IEEE Transaction on Magnetics* **MAG-8** 105 (1972)
- Rosland L.W., Cock G.J., Muller F.A., Moleman A.C., McEwan K.A., Jordan R.G. and Jones D.W., *J. Phys. F: Met. Phys.* **5** L233 (1975)
- Ruderman M.A. and Kittel C., *Phys. Rev.* **96** 99 (1954)
- Salamon M.B. and Simons D.S., *Phys. Rev. B* **7** 229 (1973)
- Schoenborn B.P., *Acta Cryst.* **A39** 315 (1983)

- Smidt F.A. and Daane A.H., *J.Phys.Chem.Solids* **24** 361 (1963)
- Souza J.B., Moreira J.M., Braga M.E., Palmer S.B., Bates S. and Beaudry B.J., *J.Phys.F: Met.Phys.* **15** 1171 (1985)
- Squires G.L., *Introduction to the Theory of Thermal Neutron Scattering*, Cambridge University Press (1978)
- Stassis C., Deckman H.W., Harmon B.N., Desclaux J.P. and Freeman A.J., *Phys.Rev.B* **18** 369 (1977)
- Takashi I., Takeuchi J., Mizuno K., Ito K., Oka M., Beaudry B.J., *Jap. J. App. Phys.* **26** L1868 (1987)
- Thoburn W.C., Legvold S. and Spedding F.H., *Phys. Rev.* **110** 1296 (1958)
- Tibbals J.E., Feteris S.M. and Barnes Z., *Aust.J.Phys.* **34** 689 (1981)
- Turov E.A. and Sharov V.G., *Sov. Phys. Usp.* **26** 543 (1983)
- Wakabayashi N., Sinha S.K. and Spedding F.H., *Phys. Rev.* **B4** 2398 (1971)
- White H.W., Beaudry B.J., Burgardt P. and Harmon B.N., *AIP Conf. Proc.* **29** 329 (1975)
- Wollan E.O., *Phys. Rev.* **100** 369 (1967)
- Wollan E.O., *J.Appl.Phys.* **38** 1371 (1967)
- Yoshimori A., *J.Phys. Soc.(Japan)* **14** 807 (1959)
- Yosida K., *Phys. Rev.* **106** 893 (1957)
- Yosida K. and Watabe A., *Progr.Theoret.Phys.(Kyoto)* **28** 361 (1962)
- Young R.C., *J.Phys.F* **13** L239 (1983)
- Zachariasen W.H., *Acta Cryst.* **23** 558 (1967)

Publications arising from this work and through collaborative work

- The magnetic structures of Gd-Sc alloys**  
 Melville R.J., Bates S., McIntyre G.J., Souza J.B. and Palmer S.B.,  
*Europhys. Lett.* **6** 725 (1988)
- Magnetic phases of Gd-Sc alloys in the multicritical regime**  
 Melville R.J., Palmer S.B., McIntyre G.J. and Souza J.B.,  
*J. Appl. Phys.* **64** 5889 (1988)
- The magnetic Structure of holmium: II**  
 Bates S., Patterson C., McIntyre G.J., Palmer S.B., Mayer A.,  
 Cowley R.A. and Melville R., *J.Phys.C* **21** 4125 (1988)

Physical properties of Gd-Sc single crystal random alloys

Melville R.J., Palmer S.B., Sousa J.B., Moreira J.M., Carvalho C.  
and Pinto R.P., *J. de Physique C3* 341 (1988)

Magnetic structures of  $Gd_{1-x}Sc_x$  single crystal alloys

Melville R.J., Bates S., McIntyre G.J., Sousa J.B. and Palmer S.B.  
*Physica B* 154-157 788 (1988)

THE BRITISH LIBRARY DOCUMENT SUPPLY CENTRE

TITLE

Magnetic Properties of Gd-Y and Gd-Sc Alloys

AUTHOR

Richard John Melville

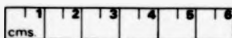
INSTITUTION  
and DATE

UNIVERSITY OF WARWICK

1989

Attention is drawn to the fact that the copyright of this thesis rests with its author.

This copy of the thesis has been supplied on condition that anyone who consults it is understood to recognise that its copyright rests with its author and that no information derived from it may be published without the author's prior written consent.



THE BRITISH LIBRARY  
DOCUMENT SUPPLY CENTRE  
Boston Spa, Wetherby  
West Yorkshire  
United Kingdom

20

REDUCTION X

CAMEL

3

D90925